PREPARATION OF NANOSTRUCTURED INTERFACE BY POLYMER GRAFTING ON VARIOUS SOLID SUBSTRATES FOR BIOSENSOR APPLICATIONS

A Thesis Submitted to
the Graduate School of
İzmir Institute of Technology
in Partial Fulfillment of the Requirements for the Degree of

DOCTOR OF PHILOSOPHY

in Chemistry

by
Sezer ÖZENLER

December 2021
İZMİR

ACKNOWLEDGMENTS

Firstly, I would like to thank my esteemed advisor Assoc. Prof. Dr. Ümit Hakan YILDIZ, who is always support me with his excellent guidance, knowledge, caring, and experience during the creation, planning, and performing of the thesis study. I am also thankful to Assoc. Prof. Dr. Ahu ARSLAN YILDIZ and Biomimetics group to support me in sharing the laboratory equipment and environment.

I am very grateful to Dr. Ufuk Saim GÜNAY and the ITU group for supplying polyester. Besides, I would like to thank Müge YÜCEL, Öykü YILDIRIMKARAMAN, Tuğçe KÜÇÜKTARTAR, Dilce ÖZKENDİR İNANÇ, Soner KARABACAK, and all members of the BioSens&BioApps group. I am thankful to Material Research (IZTECHMAM), Dr. Ayşegül ERDOĞAN-Ege University Central Research Testing and Analysis Laboratory Research and Application Center (EGE-MATAL), Nanosurf Company, and Fatih AKGÜL-Terralab Turkiye.

This study is supported by the IZTECH-Scientific Research Project (2019-İYTE-291) and The Scientific and Technological Research Council of Turkey, TUBİTAK Project: 117F243. Besides, I would like to acknowledge the support of the Scientific and Technological Research Council of Turkey 2214-A International Doctoral Research Fellowship Programme for Ph.D and Council of Higher Education (CoHE) in the field of Sensor Technologies within the scope of 100/2000 Programme by CoHE.

ABSTRACT

PREPARATION OF NANOSTRUCTURED INTERFACE BY POLYMER GRAFTING ON VARIOUS SOLID SUBSTRATES FOR BIOSENSOR APPLICATIONS

This thesis presents the utilization, various applications, and characterization of the soft material-based coating formed on the gold surface with varying thickness and chemical properties resulting from the isocyanate-gold interaction. Theoretical calculations regarding the interaction of isocyanate with the gold surface revealed the character of the bond formed and the orientation of the functional groups on the surface. Results by X-ray photoelectron spectroscopy showed the tendency to shift to the high energy at N 1s and C 1s binding energies in the gold-interacting isocyanate group. In the next steps, the isocyanate-activated gold substrate was subjected to sequential incubation of 1,4-butanediol/hexamethylene diisocyanate, and thin-film formation was achieved by surface assisted (SurfAst) urethane polymerization. It was revealed with three different applications that a nano-porous polyurethane (PU) structure was formed on the gold substrate and could be postmodified by using SurfAst polymerization method. In the first application, modification with polyethylene glycol (PEG) was provided to obtain antifouling properties. The PEG-terminated PU structure on the gold surface was shown to reduce protein adhesion by approximately ten-fold. In the second application, SurfAst was applied on the 11-mercaptodecanoic acid incubated surface and grafting onto the poly (N-allyl-N-methyl-N-(3-((4-methylthiophen-3-yl)oxy)propyl) prop-2-en-1-aminium surface was characterized. As a result of PT grafting, PT nanowires with an average height of 100 nm, a width of 250 nm, and a length of 7 μm were obtained on the gold surface. In the last application, a soft nanogel was obtained by a reactive layer-layer (rLBL) coating method using the aza-Michael addition reaction of branched polyethyleneimine and polyester on the isocyanate functional surface. The mechanical and electrical permeability and coating properties of the nanogel layer were assessed. In conclusion, the high potential of isocyanate in surface activation has been demonstrated theoretically and experimentally. Effective modification of gold surfaces by polymer grafting with the SurfAst method and rLBL coating techniques has been achieved.

ÖZET

BİYOSENSÖR UYGULAMALARI İÇİN FARKLI ALTTAŞLAR ÜZERİNE POLİMER AŞILAMA İLE NANOYAPILI ARA YÜZEYLERİN HAZIRLANMASI

Bu tezde, izosiyanat-altın etkileşimi sonucu altın yüzeyde değişen kalınlık ve kimyasal özelliklerde oluşan yumuşak madde temelli kaplamanın eldesi, çeşitli uygulamaları ve karakterizasyonu sunulmuştur. İzosiyanatın, altın yüzeyle etkileşimi ile ilgili teorik hesaplamalar oluşan bağın karakterini ve fonksiyonel grupların yüzeyde yönelimlerini ortaya çıkarmıştır. X-ışını fotoelektron spektroskopisi ile elde edilen deneysel veriler altın ile etkileşen izosiyanat grubundaki N 1s ve C 1s bağlanma enerjilerinde yüksek enerjiye kayma eğilimini göstermiştir. İzosiyanat ile aktifleştirilmiş altın alttaş sonraki adımlarda 1,4-bütandiol/hekzametilen diizosiyanat sıralı inkübasyonuna uğratılarak, yüzey destekli (SurfAst) üretan polimerizasyonu ile ince film oluşumu sağlanmıştır. SurfAst polimerizasyon metodu ile altın alttaş üzerinde nano gözenekli poliüretan (PU) yapı oluştuğu ve sonradan modifiye edilebilir olduğu, üç farklı uygulama ile ortaya çıkarılmıştır. Birinci uygulamada kirlenme önleyici özellikler elde etmek için polietilen glikol (PEG) ile modifikasyon sağlanmış ve altın yüzeydeki PEG-sonlu PU yapısının protein yapışmasını yaklaşık 10 kat azalttığı gösterilmiştir. İkinci uygulamada SurfAst, 11-merkaptoundekanoik asit inkübe edilmiş yüzeyde çalışılarak poli (N-allil-N-metil-N-(3-((4-metiltiofen-3-il)oksi)propil) prop-2-en-1-aminyum bromür'ün (PT) yüzeye aşılaması karakterize edilmiştir. PT aşılaması sonucunda altın yüzey üzerine ortalama 100 nm yükseklik, 250 nm genişlik ve 7μm uzunlukta PT nanoteller elde edilmiştir. Son uygulamada ise, izosiyanat fonksiyonel yüzeyi üzerinde dallanmış polietilenimin ve polyesterin aza-Michael katılma reaksiyonu kullanılarak reaktif katman-katman kaplama yöntemi ile yumuşak bir nanojel elde edilmiştir. Nanojel katmanın, mekanik ve elektriksel geçirgenlik ve kaplama özellikleri çalışılmıştır. Sonuç olarak, yüzey aktifleştirmede izosiyanatın yüksek potansiyeli teorik ve uygulamalı olarak gösterilmiş ve altın, yüzeylerin SurfAst metodu ile polimer aşılaması ve reaktif katman-katman kaplama teknikleri ile etkin modifikasyonu sağlanmıştır.

.

Dedicated to my family…

TABLE OF CONTENTS

LIST OF FIGURES

Figure **Page**

Figure **Page**

Figure **Page**

Figure **Page**

Figure **Page**

Figure **Page**

Figure **Page**

LIST OF TABLES

Table **Page**

LIST OF ABBREVIATIONS

AFM	Atomic Force Microscopy
CPEs	Conjugated polyelectrolytes
EFM	Electrostatic force microscopy
OFET	Organic field-effect transistors
rLBL	Reactive layer-by-layer assembly
SAM	Self-assembly monolayer
SEM	Scanning Electron Microscope/Microscopy
SI-ATRP	Surface-initiated atom transfer radical polymerization
SIP	Surface-initiated polymerization
SurfAst	Surface-assisted urethane polymerization
TOF-SIMS	Time-of-flight secondary ion mass spectrometry
VASP	Vienna Ab Initio Simulation Package
XPS	X-ray photoelectron spectroscopy

CHAPTER 1

INTRODUCTION

1.1. Motivation

Biosensors and implantable bioelectronic systems have become an important area of research due to increasing interactions between living beings and electronic systems. Determining, conserving, and maintaining the delicate balance at the interface between bio and electronic components is important to the success of the biosensor field. Therefore, the interface is combined with metals or semiconductors, which are electronic components of bioelectronic systems, to produce a soft and stimulus-sensitive interface. Although silane and thiol-based molecules are widely used as interface modification agents, they exhibit limited stability and robustness under ambient or physiological conditions. In silane-based agents, cross-links and uncontrolled oligomerization can form irregular structures on oxide surfaces, while nano-scale chemical coating with thiol-based surface functionalization cannot be controlled with sufficient precision on gold surfaces. The permanence of achievement can be provided with the continuity of well-defined alternative interface studies. Consequently, the stimulus-sensitive interface has become an always up-to-date research field that needs to be constantly explored. Therefore, various isocyanate sources have been investigated to produce reactive self-assembly-like behavior on gold surfaces since isocyanate is a very important functional group that reacts with groups containing active hydrogens such as hydroxyl, amine, and urea. Thus, it is planned to make both surface modifications and to provide reactive isocyanate groups that enable the formation of polymeric structures with the further reaction on the surface. Because, although conventional modification methods are useful methodologies for surface modification of metals, metal oxides, and semiconductors, they demand laborious and tedious polymerization steps which can be regarded as disadvantageous for effective fabrications. In this context, the straightforward and novel "grafting from" methodology named surface-assisted (SurfAst) urethane polymerization has fabricated a highly efficient, well-defined post-functionalizable polyurethane interface using isocyanate modified gold surfaces. In addition, poly(N-allyl-N-methyl-N-(3-((4-methylthiophen-3-

yl)oxy)propyl)prop-2-en-1-aminium bromide as cationic polythiophene "grafting to" methodology to the gold surface has been investigated using the Surfast methodology. Moreover, nanometer-thick gels production has been probed by the "reactive layer-by-layer assembly" methodology on the isocyanate modified gold surface. In this thesis, we foresee that an isocyanate functionalized gold surface could provide all basic surface modification methodologies like *grafting to*, *grafting from*, and *reactive layer-by-layer assembly* that do not require inert conditions, degassing, or high-cost catalysts that limit the feasibility of biosensor applications.

1.2. The Structure and Scope of the Thesis

The *Chapter 1* of the thesis presents the motivation and introduction. In *Chapter 2*, an investigation of a high-efficiency, stable isocyanate-gold interaction has been presented. The surface-assisted (SurfAst) urethane polymerization technique (*grafting from*), which is based on the isocyanate-gold interaction, has been studied in detail in *Chapter 3*. In *Chapter 4*, the structural and electronic properties of *grafting to* cationic polythiophene on a gold surface by using the SurfAst polymerization method are investigated. *Chapter 5* presents the reactive *layer-by-layer assembly* method with the aza-Michael addition reaction forming nanometer-thick gels by using an isocyanate-gold interaction. *Chapters 6* and *7* introduce a brief overview of micro-patterning of the hydrogel by laser ablation for cell guidance study and the general concluding remarks and future prospects, respectively.

1.3. Surface Modification Techniques

Surface modification alters surface features such as roughness, hydrophilicity, charge, energy, and reactivity by changing the properties of the interface that interacts with the environment.[1, 2] Molecular self-assembly (SAM) is the modification technique that can be functionalized or modified for the interface; thus, the well-ordered structures are obtained on the surface.[3] Well-ordered SAMs are provided by secondary interactions like electrostatic interactions, intermolecular hydrogen bonds, π-π interactions, hydrophobic interactions, and hydrophilic interactions.[4] Silane and thiol-based agents are most commonly used to create monomolecular films in interface modification. The

properties of an interface are determined by the terminal group of SAM while the anchoring group tends to interact with the surface (Figure 1.1).[5]

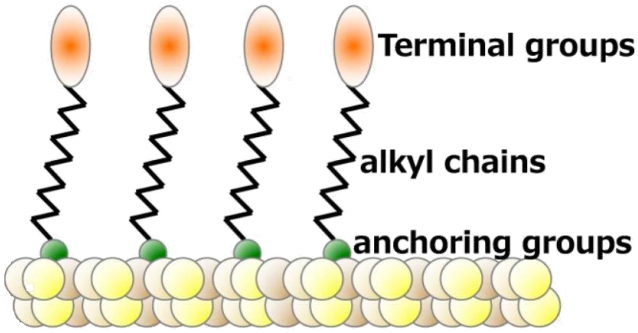

Figure 1.1. Scheme of self-assembled monolayers.[5]

In the gold-alkanethiol interaction, the alkyl chains form a closely packed structure due to the high affinity of the thiol group to the gold surface, as well as gold nanoparticles that change the properties of the gold interface.[6, 7] The alkyl chain length of thiol molecules is an important parameter to achieve crystal structure, and dense monolayers can be achieved when the number of methylene chains is higher than ten (tilted 20-30^{o} from the surface).[8] On the other hand, the main advantage of using silane is the rapid formation of a covalent bond between the substrate and the terminal group. The best substrates for silane modification are Si-OH groups like quartz glass, although metal oxide surfaces are also used. This covalent bond stabilizes the monomolecular film and allows easy chemical modification without disrupting the unity of the monomolecular film.

1.4. Interface Engineering with Polymer Brushes

Polymer brushes, first used by de Gennes to define the molecular structure of densely linked polymer chains, are useful for controlling the properties of materials.[9, 10] Polymer brushes are a powerful study area in surface and interface engineering because they adapt the chemical and physical properties of the interfaces as one end of the polymer chain is tethered to a solid interface. Polymer brushes could be found in various polymer chain conformations depending on their surface bonded density and molecular weight. As seen in Figure 1.2, these three basic conformations are the “pancake” or “mushroom” state for low polymer density and the “brush” state for high polymer density on the solid

surface.[11] Two conformations are presented: i) the mushroom structure, where the chains are in a relaxed conformation with the sparse grafting regime (D > 2RG) and ii) the brush structure, where excluded volume interactions lead to stretched chain conformations with a dense grafting regime (D < 2RG) (D: Distance between chains RG: Radius of gyration).

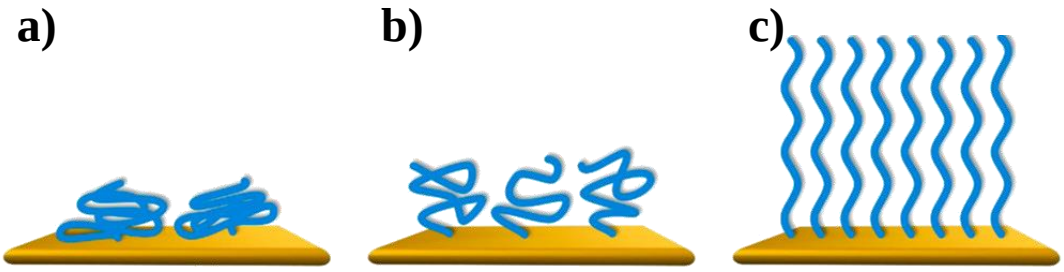

Figure 1.2. Scheme of three basic conformations: a) pancake, b) mushroom, and c) brush-type state.[11]

Pancake, mushroom, and brush states can be fabricated on the solid surface by the *grafting from* and *grafting to* methods described in the following section. Furthermore, the *layer-by-layer assembly* (LBL) method, which provides a robust polymer coating on the solid surface and is a good alternative to the graft methods, has been examined within the scope of the thesis and is explained in the following section.

1.4.1. *Grafting from* and *Grafting to* Methodologies

As seen in Figure 1.3, the fabrication of polymeric brushes on the surface can be conducted in two basic ways: i) *grafting to*, or covalently bonding a synthesized polymer to the surface and ii) *grafting from*, or creating polymer propagation on the solid surface by adding monomers (bottom up approaches).[12]

Grafting to methodology takes place when a covalent bond is formed as a result of the reaction between the chemical group of the solid surface and the pre-modified terminal group of the polymer. However, since the methodology is based only on the reaction between chemical group of the solid surface and the polymer, it is difficult to remove polymers that are not grafted onto the surface after fabrication. In addition, although it is a straightforward and rapid method to obtain a polymer brush, it is difficult to graft the surface with high yield polymer grafting due to steric hindrance which makes it hard to tether chain ends. On the other hand, the *grafting from* methodology is

promising for fabricating with a purer, high yield polymer grafting. The method has two basic steps: i) surface modification by using an initiator and ii) polymer chain growth gradually occurs on the surface. The method, which uses small molecules compared to polymer, results in a high-density polymer brush on solid surfaces and is promising and versatile for grafting polymers to biomolecules such as enzymes, proteins, or peptides.[11-13]

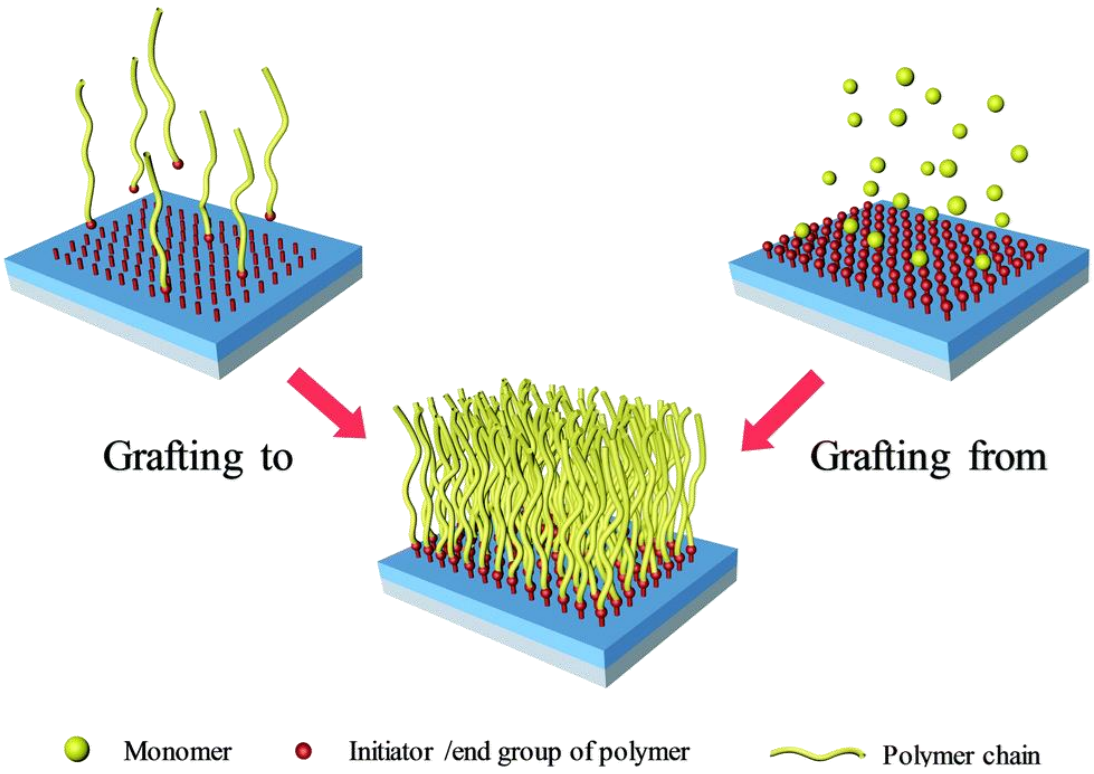

Figure 1.3. *Grafting to* and *grafting from* strategies for fabricating polymer brush.[12]

Growing a polymer from the surface with a *grafting from* methodology is also called surface-initiated polymerization (SIP). To understand the application of the *grafting from* polymerization method, the surface-initiated atom transfer radical polymerization (SI-ATRP) could be probed. Recently, SI-ATRP has become the most commonly used controlled radical polymerization technique for modifying solid surfaces with polymer brushes. Using the same mechanism as ATRP, SI-ATRP involves basic (initiation, propagation, activation/deactivation, and termination) steps. Figure 1.4 demonstrates that alkyl halide dormant/initiators species (P_n–X) react with activators to reversibly create propagating radicals (P_n•) and deactivators and complexes of Cu^{II} halides.[14, 15]

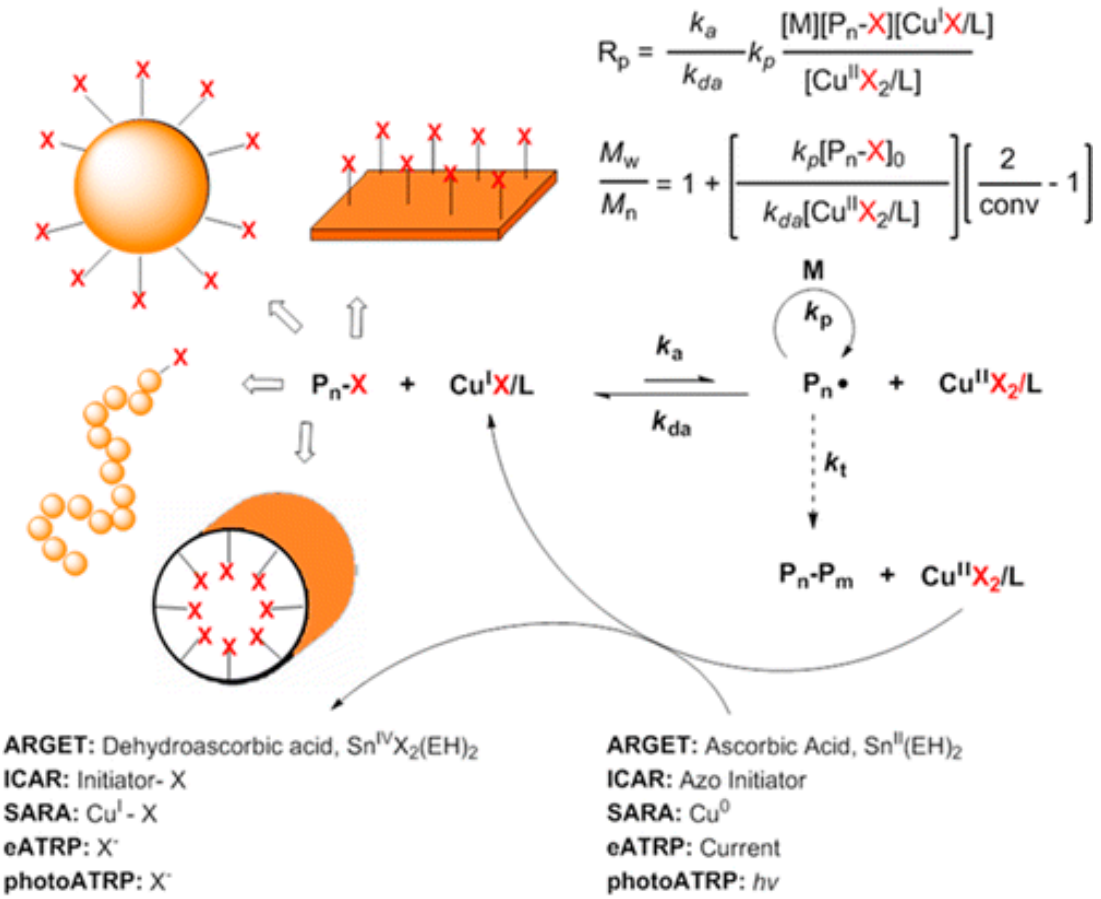

Figure 1.4. Illustration for ATRP and low-ppm Cu-ATRP.[9]

The dependence of dispersity (M_w/M_n) and polymerization rate (R_p) on kinetic parameters and reagent concentrations are shown in Figure 1.4 (top right). Polymerization rate (R_p) relies on the ratio of the rate constants of activation (k_a) and deactivation (k_{da}), propagation rate constant (k_p), and the concentrations of related reagents. Also, catalysts with a higher value of k_{da} create faster deactivation and have reduced dispersity (M_w/M_n). Experimentally, the SI-ATRP used to obtain the polymer brush on the solid surface is performed in the following two basic steps: (i) modification of the initiator on the target surface and (ii) performance of ATRP under airtight conditions to form a polymer brush. In the second stage, the deoxygenation (airtight conditions) process must be done using a complex apparatus. Additionally, a large amount of copper (Cu) catalyst (0.1−1 mol % vs monomer) may be deposited on the resulting polymer brush; therefore, a long washing step is often required for complete removal. On the other hand, ARGET (activators regenerated by electron transfer) ATRP uses excessive amounts of reducing agents (e.g., ascorbic acid) and oxidized Cu^{II} catalysts (Figure 1.4, bottom part). The reducing agent acts as a chemical reservoir that continuously regenerates active Cu^{I} species from inactive

Cu^{II} species. Unlike the SI-ATRP method, a simple washing step is sufficient for removal because the Cu catalyst is used in low concentrations.[16-20]

As a general assessment, the *grafting from* method has key advantages when compared to the *grafting to* method in areas such as organic electronics or device manufacturing. In the *grafting from* method, the density and thickness of the polymeric brushes are precisely controlled by first activating the solid surface before tuning the reaction conditions by adding small monomers to enable polymer growth stepwise fashion. Moreover, the *grafting from* method allows the production of sharply patterned polymeric brushes with specific patterning using lithographic methods. In this thesis, both *grafting from* (*Chapter 3*) and *grafting to* (*Chapter 4*) methods were used by using isocyanate modified gold surface, and the methods were compared with the experimental investigations.

1.4.2. Layer-by-Layer Assembly

As an alternative method to *grafting from* and *grafting to* strategies, multilayer thin-film coatings are crucial techniques for surface modifications. *Layer-by-layer assembly* (LbL) is used to create films that provide nanoscale control on film thickness and its composition on the solid surface for various applications. LbL, which is basically a bottom-up strategy, is a useful method in fields such as biotechnology, electronics, catalysis, and energy by giving films the mechanical, electrical, optical, and thermal properties with various functional groups or unique polymer selections. Additionally, the LbL method allows reproducible and robust surfaces with desired strategies for surface methodologies that are simple, cost-effective, and flexible to be used for this wide range of applications. The LbL method, which can be performed on any substrate type (planar, cylindrical, porous, etc.), consists of the sequential adsorption of components (polymer, peptide, dye, etc.) on the surface that mainly drive force electrostatic or non-electrostatic interactions and reactive LbL (rLbL), as shown in Figure 1.5.[21-23]

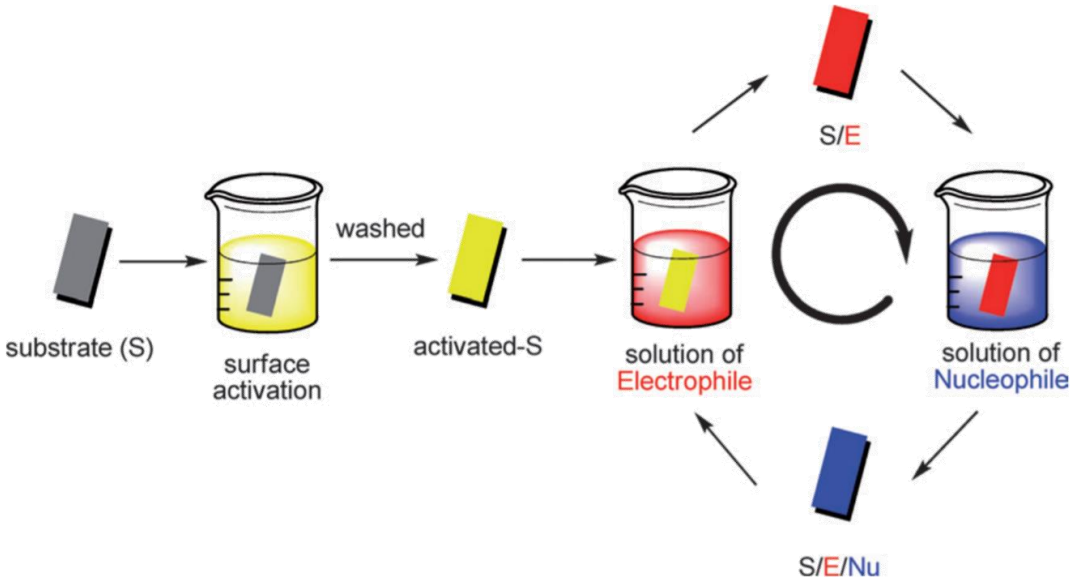

Figure 1.5. Illustration of reactive LbL assembly nucleophile (Nu) and electrophile (E).[24]

Electrostatic interactions based LbL is an assembly mechanism performed by sequentially immersing a pair of oppositely charged polyelectrolytes on a charged substrate. Multilayer films that are formed using aqueous polyelectrolyte solutions are particularly suitable for biomedical applications. In addition to electrostatics LbL, hydrogen bond donors and hydrogen bond acceptors are also driving forces for the incorporation of many neutral materials into multilayer films. However, electrostatic or hydrogen bond LbL assembly has the disadvantage of being able to break under conditions where ionic or hydrogen bonds are unstable, such as in strongly acidic, highly ionic, or strongly basic solutions. To overcome this disadvantage, reactive LbL (rLbL) is another alternative driving force that notably improves the stability and strength of the multilayer structure. Furthermore, the "click" chemistry of multiple reactive groups utilized in the rLbL assembly allows pre- and post-functionality by incorporating several other functional groups into the films (Figure 1.5). The rLBL method has four main advantages over other non-covalent methods: i) the covalent bond provides high stability and endures severe conditions, ii) in situ covalent bonding does not require post-crosslinking, iii) various types of reactions can be carried out in aqueous or organic (or mixtures) solutions, and iiii) the latest deposited layer does not disassemble the previous layer. In this thesis, the rLBL method was used with the aza-Michael addition reaction of the −NH2 groups of BPEI and the alkyne group of PE (*Chapter 5*).[24]

1.5. Characterization Methods

1.5.1. X-ray Photoelectron Spectroscopy

The characterization of the chemical composition of the surface, which can be completely different from the bulk material composition, is critical to determining and evaluating the properties of the interface. X-ray photoelectron spectroscopy (XPS) is a powerful technique that is used to provide binding energies to characterize the chemistry and composition of interfaces with a high precision and sensitivity. XPS analysis is based on the photoelectric effect, in which the X-ray is a probe source. On the X-ray source, aluminum or magnesium is used generally band on the rim of the anode material. The energies (hυ) of the resulting Al Kα or Mg Kβ photons are 1486.7 eV and 1253.6 eV, respectively. These photons have limited penetrating power (the order of 1-10 micrometers) and interact with atoms in the surface region causing the emission of electrons. The emitted electrons have kinetic energy given by: KE = hυ - BE - Φs (where BE: binding energy, KE: measured kinetic energy of photoelectron, hυ: is the energy of X-ray photons and Φs: the work-function.) To resolve the kinetic energy distributions of electrons ejected from the sample are measured with an electron energy analyzer. Since the XPS tecnique is very sensitive to surface contamination, the samples are examined in ultra-high vacuum (UHV) conditions in order to provide surface stability and to prevent the scattering of the ejected electron by hitting the gas molecules (Figure 1.6).[25]

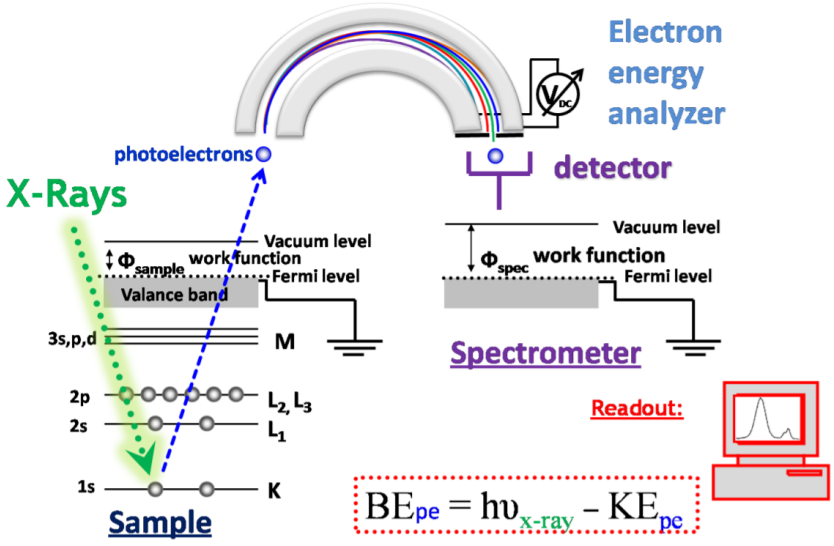

Figure 1.6. Principles and components of XPS.[25]

1.5.2. Atomic Force Microscopy

Atomic Force Microscopy (AFM) is a sub-technique of scanning probe microscopes that profile the surface at the nanometer scale. AFM is a unique characterization method that allows characterizing the topography, mechanical and electrical properties of the surface. Figure 1.7 shows the parts of AFM that include piezoelectric tube scanner, tip, photodetector, laser source, position sensor, etc., and the substrate is located on the top of the piezoelectric tube scanner. AFM has two basic operating modes: static and dynamic. In static mode, the probe tip makes constant physical contact with the surface, and surface profiles are recorded directly as the vertical deflection of the tip. In dynamic mode, the probe tip is oscillated at a high frequency or close to resonance. The changes in oscillation amplitude and resonance frequency are measured depending on the interaction forces when the probe tip comes close to the sample surface.[26]

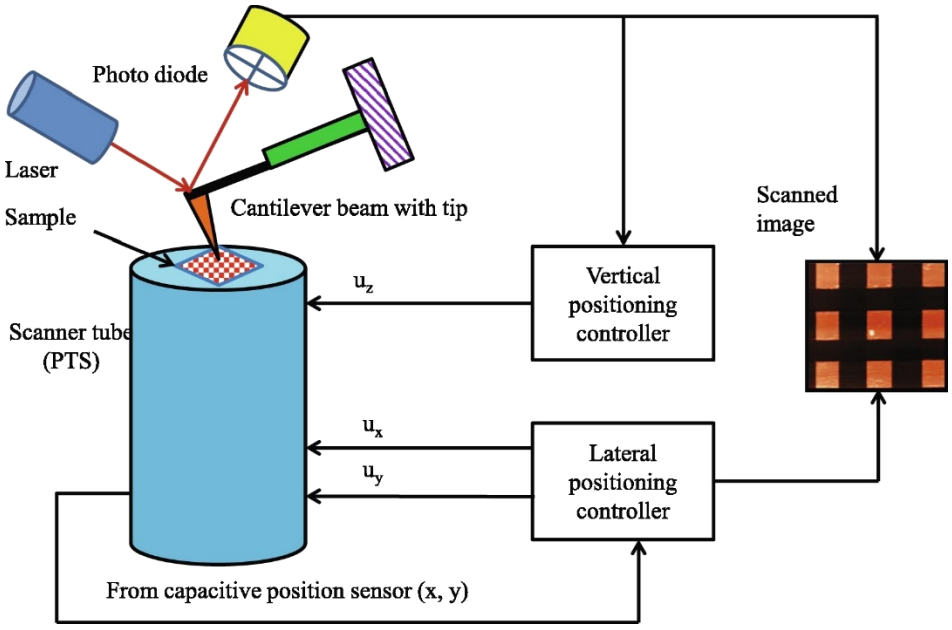

Figure 1.7. Principles and components of AFM.[26]

In addition, electrostatic force microscopy (EFM) is a special type of dynamic mode in which the electrostatic force is dominated between tip and sample. The biased tip and sample are measured as long-range interaction with an adjustable tip lift that only electrostatic interactions can predominate. Contour mode is the most effective mode of EFM that takes place with two sequential scans. The first scan includes a typical dynamic

mode (Figure 1.8-black line). The Z-axis data added from the first scan is used to EFM measurement the surface from a certain height in the second scan (Figure 1.8-red line).[27]

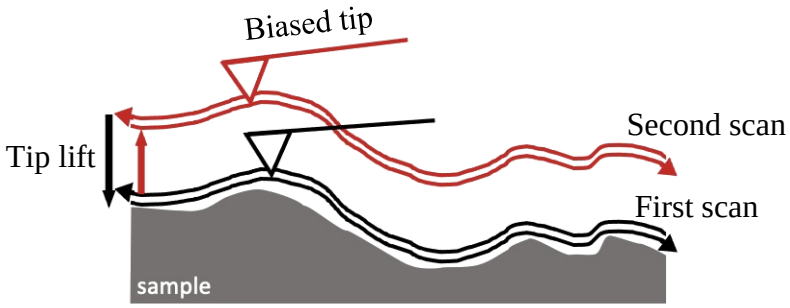

Figure 1.8. Principles of contour mode EFM.

1.5.3. Cyclic Voltammetry

Electrochemistry is an important tool for relating the flow of electrons to chemical changes. Cyclic voltammetry (CV) is an electrochemical technique used to examine the oxidation and reduction behavior of molecular species. The potential is applied by sweeping between the set limits at a constant scan rate in cyclic voltammetry. The traces in Figure 1.9 are cyclic voltammogram that the x-axis represents the applied potential (E), and the y-axis is the resulting current (i) passed.

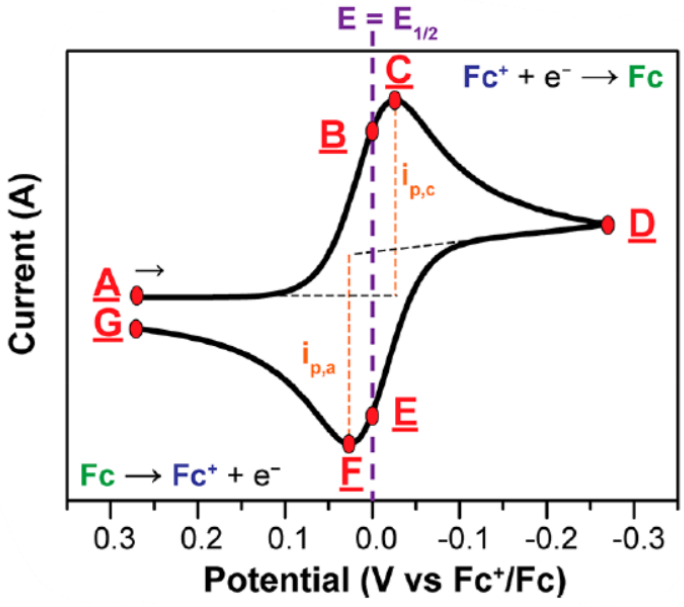

Figure 1.9. Cyclic voltammogram of Fc+ solution to Fc (scan rate: 100 mV/s).[28]

As the potential is scanned from point A to point D, Fc+ is steadily consumed on the electrode, and it is reduced to Fc. The peak cathodic current ($i_{p,c}$) is observed at point C. The scan direction is reversed at D, the potential is scanned in the anodic direction and the Fc is oxidized back to Fc^+. The concentrations of Fc and Fc+ are equal at points B and E. Observed peaks at C and F provide an easy way to determine the $E^{0'}$ for a reversible electron transfer.[28]

1.5.4. VeeMAX III Variable Angle Specular Reflectance Accessory

The VeeMAX III accessory enables to be analyzed in the specular reflectance sampling mode over a range of incident angles from 30° to 80° designed for use in FTIR spectrometers. The VeeMAX III employs a unique optical design for FTIR analysis on the surfaces. Maximum throughput of the VeeMAX III will occur at a set angle of incidence of about 45° to 50°. For a p-polarizer, when the polarizer is set to 0° the grid lines run parallel to the width of the polarizer mount and the transmitted IR radiation will be perpendicular to this. When the polarizer is set to 90° the grid lines run parallel to the length of the polarizer mount and the transmitted IR radiation will be perpendicular to this (Figure 1.10). In addition, VeeMax is often utilized to determine self-assembly behavior in the literature.[29, 30] In this thesis, the effect on PU orientation and self-assembly properties was investigated by using VeeMAX III with p-polarizer by performing SurfAst urethane polymerization with isophorone diisocyanate (IPDI)/1,4-Phenylene diisocyanate (PDI)/hexamethylene diisocyanate (HDI) and 1,4-Butanediol (1,4-BDO).

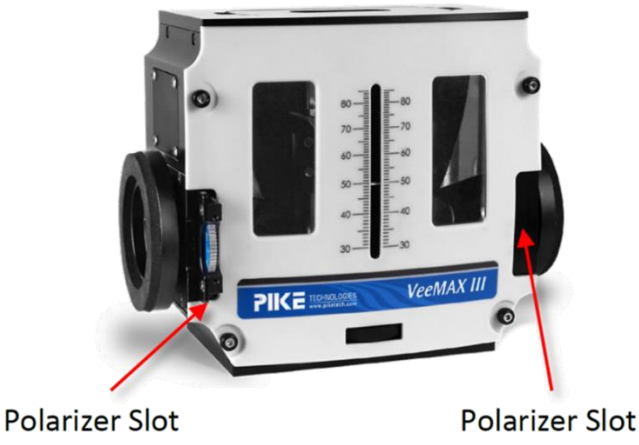

Figure 1.10. VeeMAX™ III Variable Angle Specular Reflectance Accessory.

CHAPTER 2

ISOCYANATE GOLD SURFACE INTERACTION

SAM of silane and thiol are widely employed for surface and modifications however SAMs exhibit limited stability and robustness under ambient or physiological conditions and that limits their practical application. For instance, in silane-based agents, the cross-links formed within the monomolecular layer increase the stability; however, the cross-links could be formed within irregular structures and uncontrolled oligomerization, as seen in Figure 2.1.[31]

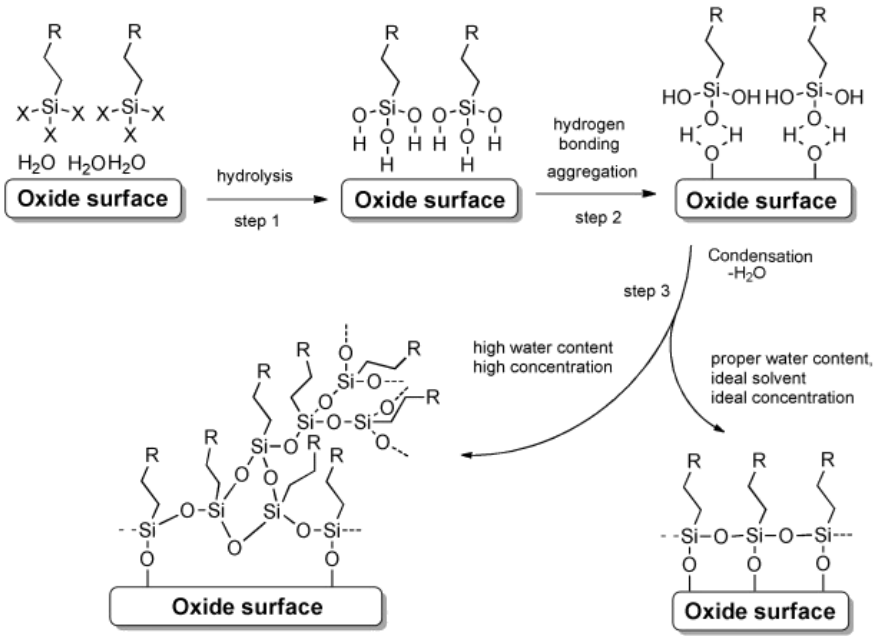

Figure 2.1. Single-layer formation mechanism by silanes on OH terminated surfaces disordered inhomogeneous multilayers (left) and laterally cross-linked (right).[31]

In the gold-thiol interaction, aromatic structure-based thiol molecules show well-ordered packaging due to π-π interactions; however, they have less stable than long-chain alkanethiols.[32] In addition, the chemical coating may not be controllable with sufficient precision at the nanoscale with thiol-based surface functionalization, and pinhole defects may occur on the surface.[33, 34] Some SAMs such as $–CH_3$ and –COOH terminate have poor chemical stability that degraded easily the course of investigations.[35] Moreover, a

hydrophobic SAM surface has a high surface energy that causes the deposit of contaminants in the analyte recognition sites, and these impurities could change the actual measuring area of the sensor surface.[36] Although silane and thiol agents (SAMs) are a conventional surface functionalization methods, the need for novel surface functional agents continues due to their drawbacks. Therefore, linear aliphatic and aromatic isocyanates have been investigated to fabricate reactive self-assembly-like behavior on gold surfaces in this chapter. Thus, it is planned to make surface modifications and create reactive functional groups that allow the formation of polymeric structures with the further reaction on the surface.

Isocyanate is an important functional group that reacts with active hydrogen-containing groups such as hydroxyl, water, amine, and urea.[37] The high activity of the isocyanate group can be explained by the following resonance structure (Figure 2.2).

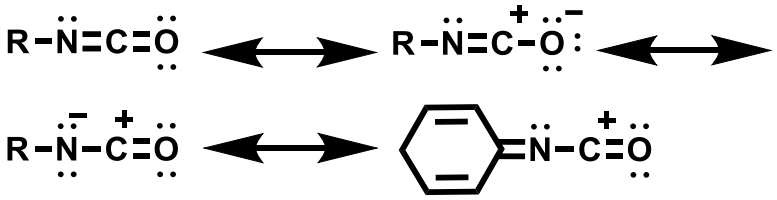

Figure 2.2. Resonance structure of the isocyanate group.

The carbon atom has a low electron density, while the oxygen atom has a higher electron density. The carbon atom is positively charged, the oxygen atom is negatively charged, and the nitrogen atom is moderately negatively charged. The reaction of active hydrogen (HXR; X: O, N etc; R: alkyl / aryl) with isocyanate is the addition of hydrogen to the C=N double bond (Figure 2.3).[37]

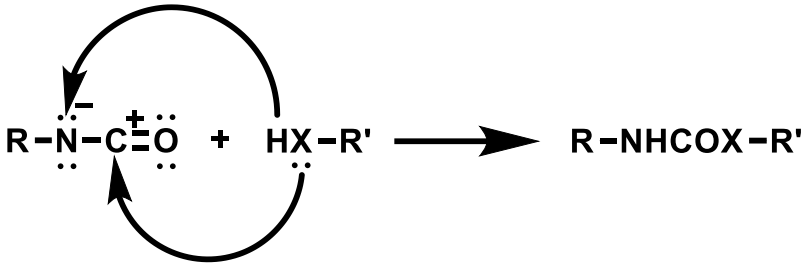

Figure 2.3. Reaction of active hydrogen with isocyanate.

In the literature, Tardio et al. examined the interactions of methylene diphenyl diisocyanate (MDI) and polymeric MDI (p-MDI) molecules with a 316L stainless steel

surface by incubating them in acetone.[38] XPS and a time-of-flight secondary ion mass spectrometry (TOF-SIMS) analysis revealed that a urethane-like bond was formed between diisocyanate and metal surface as a result of the reaction of isocyanate groups and hydroxyl groups on the metal surface.

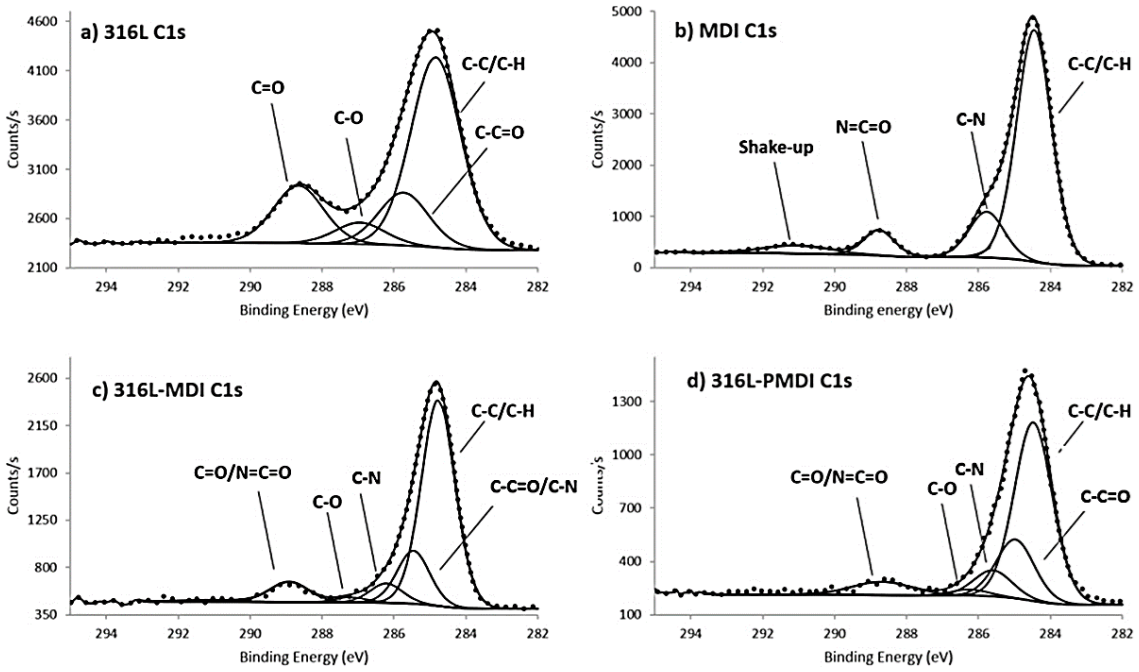

Figure 2.4. XPS spectra of C 1s a) oxidized 316L stainless steel, b) bulk-MDI, c) MDI-316L stainless steel interface, and d) PMDI-316L stainless steel interface.[38]

Figures 2.4a and b show C 1s XPS spectra of oxidized 316L stainless steel and bulk-MDI, respectively. Oxidized 316L stainless steel shows four well-defined peaks, while bulk-MDI shows three characteristic peaks. The main difference in the C 1s XPS spectra of Figures 2.4a and b is that the binding energy of the isocyanate group of bulk-MDI is 288.8eV and the binding energy of the nitrogen atom attached to the carbon atom of the aromatic ring is 285.6 eV. Figures 2.4c and d shows the XPS spectra of C 1s MDI-316L and PMDI-316L of the stainless steel interface, respectively. A similar peak profile is seen in Figures 2.4c and d, showing a combination of bulk-MDI and 316L stainless steel C 1s that indicate the existence of carbon contamination from 316L stainless steel at the interface.

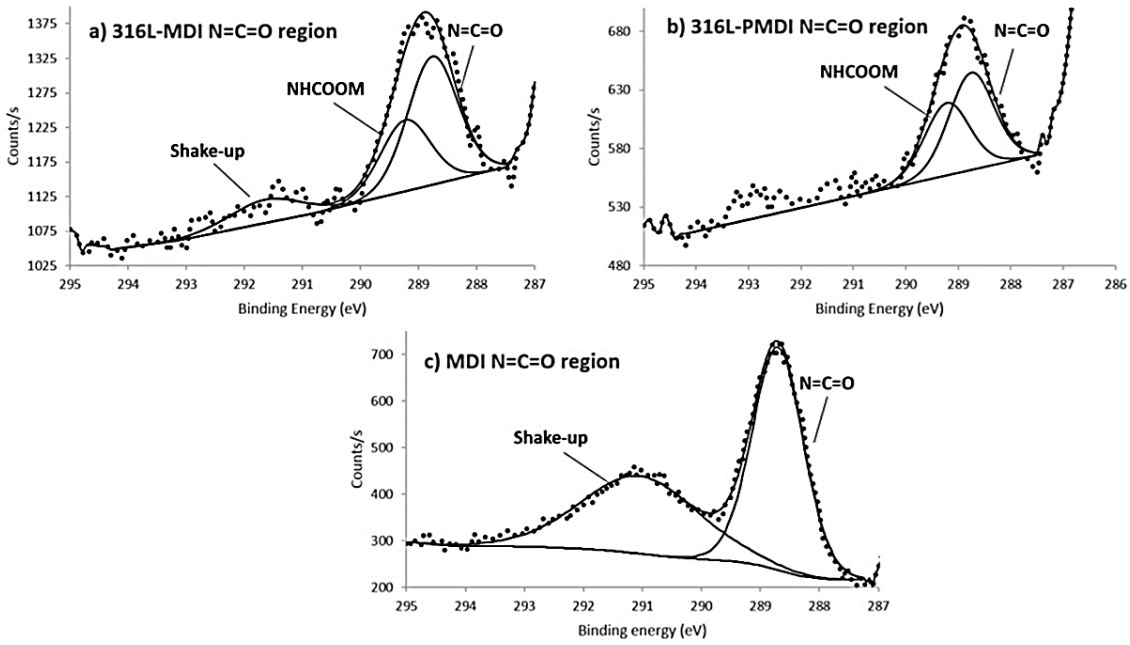

Figure 2.5. High-resolution XPS spectra of C 1s a) MDI-316L stainless steel interface, b) PMDI-316L stainless steel interface, and c) bulk-MDI.[38]

A high-resolution C 1s XPS spectra MDI-316L, PMDI-316L stainless steel interface, and bulk-MDI of the high binding energy region of the isocyanate functional group are shown in Figure 2.5. The peak of the isocyanate in the high binding energy region of bulk-MDI is symmetrical which indicates a single functional species. MDI-316L and PMDI-316L have asymmetrical and identical peaks in the high binding energy region of the stainless steel interface. Therefore, it can be considered that the peak of the binding energy belongs to two species, and it can be concluded that there are two different types of isocyanate-originating groups. These two types can be attributed to two groups as N=C=O/R-C=O and HNCOOM (M = metal). Since two binding energy peaks originate from isocyanate, a similar binding energy profile should be in the N 1s spectrum. High-resolution N 1s XPS spectra MDI-316L, PMDI-316L stainless steel interface, and bulk-MDI are shown in Figure 2.6. The N 1s peak of the isocyanate of bulk-MDI is symmetrical which is similar to the XPS spectra of C 1s bulk-MDI. However, PDI-316L and PMDI-316L are asymmetrical as the XPS spectra of C 1s can be attributed to HNCOOM (M = metal), N=C=O, and N=M, respectively. Thus, two different types of isocyanate-originating groups in the C 1s spectrum were also identified in the N 1s spectrum. In addition, they also suggested that hydrogen bond formation between nitrogen and metal hydroxide group and the cyclocation reaction between the isocyanate-metal oxide group could occur due to isocyanate reactivity.

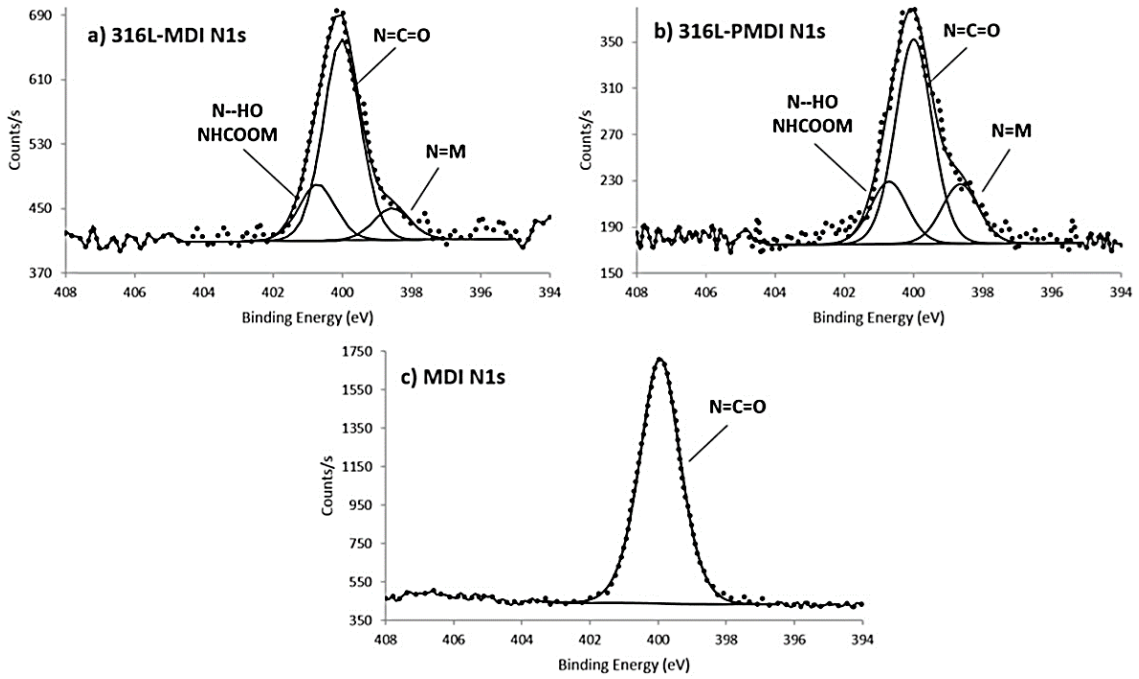

Figure 2.6. High-resolution XPS spectra of N 1s a) MDI-316L stainless steel interface, b) PMDI-316L stainless steel interface, and c) bulk-MDI.[38]

Shimizu et al.[39] coated the activated aluminum surface samples using a spin coating method with different concentrations of PMDI layers in the presence of a catalyst. They investigated the interactions between PMDI and the Al surface and the reaction between the PMDI and atmospheric humidity by XPS and TOF-SIMS. The covalent bond formed between PMDI and the Al layer has been observed. Nies et al.[40] investigated the interaction of MDI and propylene ether triol (PPET) with Au, Al, and Cu surfaces in a tetrahydrofuran (THF) solvent for three minutes. As a result, MDI monomers exhibited strong adhesion behavior because of the stronger interactions on the Cu and Al surface; however, MDI monomers were adsorbed weakly on the Au surface. These results confirm that experimental planning like incubation time, temperature, organic and metal-based catalysts, isocyanate type, and surface activation method are crucial parameters in isocyanate/surface interaction. In this chapter, an isocyanate gold surface interaction has been investigated to uncover self-assembly-like behavior with the most yielded and stable structure on the gold interface. In this context, PDI was used for rigidity aromatic structure whereas p-MDI was used for rigidity aromatic structure, which has more than two functionalities. HDI was used for a linear aliphatic that provides a more flexible structure than PDI and p-MDI. A combination of the applied experimental methods

(temperature, metal-based catalyst and high incubation time in acetone) has been performed, and the high-efficiency stable isocyanate-gold interaction has been shown for the first time in the literature.

2.1. Materials and Methods

1,4-Phenylene diisocyanate (PDI), polymeric methylene diphenyl diisocyanate (p-MDI), hexamethylene diisocyanate (HDI), 1,4-diazabicyclo[2.2.2]octane (DABCO), and dibutyltin dilaurate (DBTDL) (95%) were purchased from Sigma Aldrich and used without any further purification. Ammonium hydroxide (30%, Merck) and hydrogen peroxide (30%, Sigma Aldrich) were used in RCA cleaning. Acetone (99.5%, Sigma Aldrich) was used as a solvent.

Adsorption between the Au (111) surface and HDI was studied by utilizing the DFT method performed in Vienna Ab Initio Simulation Package (VASP) and projector augmented wave pseudopotentials.[41-44] By using the generalized gradient approximation function advanced by Perdew−Burke−Ernzerhof, the exchange−correlation energy of the system was estimated.[45] The weak dispersion forces were adjusted by including Grimme's DFT-D2 method, which allows more precise correlation energies to be defined.[46] The cut-off energy for the plane-wave basis set was restricted to 500 eV. The 2×2×1 k-point mesh has been determined to be effective to integrate the Brillouin zone of the system. Partial occupancies were specified with respect to Gaussian smearing method that smeared the Fermi level with a width of 0.05 eV. On the Au (111) surface, a rectangular cell was formed that cut the unit cell of the bulk Au crystal from the (111) lattice plane. The formed unit cell was broadening into a 5 × 3 × 1 supercell. The vacuum range was increased to 30 Å along the z-direction to avoid neighboring interactions in adsorption calculations. The HDI molecule was placed 2.5 Å above the topmost layer of the relaxed Au (111) surface. Binding energies were computed using the equation $E_{binding} = E_{HDI} + E_{surface} - E_{HDI + Au (111)}$, after the structural optimization of the HDI - Au (111) system. EHDI and Esurface represent the total energies of the bare Au (111) surface and HDI molecule, while $E_{HDI + Au (111)}$ represents the total energy of the HDI + Au (111) system.

RCA cleaning was applied by the following procedure: distilled water, ammonium hydroxide, and hydrogen peroxide (5: 1: 1 by volume) that were held at 80°C until the bubbles stopped and the gold surfaces were washed with distilled water. As seen

in Figure 2.7, an isocyanate source (160 mM) was dissolved in 2 ml acetone. DBTDL catalyst (90×10^{-3} mM) was added to the acetone solution. The gold surface was incubated at 40°C for 30 minutes. At the end of the incubation, the gold surface was sonicated with acetone to remove the unbounded isocyanate source, and right after, the XPS point analysis was performed.

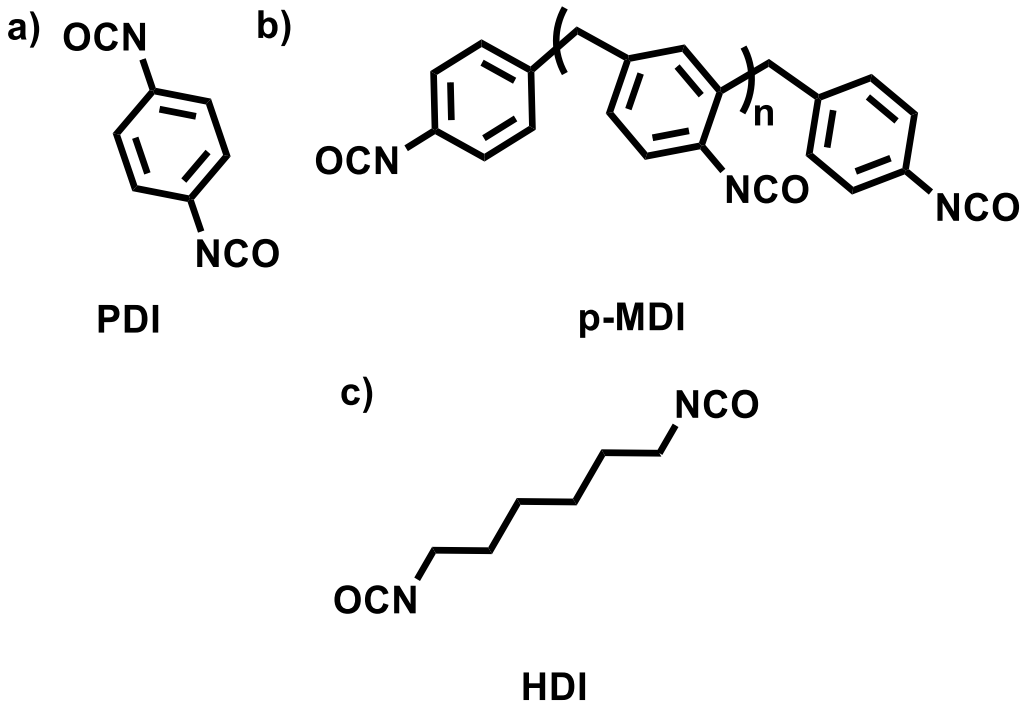

Figure 2.7. Structure of isocyanate sources a) 1,4-Phenylene diisocyanate (PDI), b) polymeric methylene diphenyl diisocyanate (p-MDI), and c) hexamethylene diisocyanate (HDI).

The second part of the chapter includes an investigation of the reaction conditions and the effect of the catalyst type. (See: 2.2.4. Hexamethylene Diisocyanate Gold Interaction in the Presence of DABCO and DBTDL). The gold surface was prepared by the following procedure for the XPS point analysis: HDI and DBTDL/DABCO with various concentrations were dissolved in the 5 mL acetone solution. The gold surfaces were incubated in acetone under various conditions. After incubation, the gold was sonicated with acetone thoroughly three times. X-ray Photoelectron Spectroscopy (XPS) analyses were performed at a pass energy of 30 eV. An Al Kα monochromatic (1486.68 eV) beam was used with a spot size of 300 μm (10 numbers of scans).

2.2. Results and Discussions

2.2.1. 1,4-Phenylene Diisocyanate Gold Surface Interaction

Figure 2.8 shows the XPS spectra obtained after the incubation of the gold surface with PDI. As shown in Figure 2.8a, the C 1s spectrum has deconvoluted into four peaks. The peaks at 284.72 eV (FWHM: 1.42) and 284.37 eV (FWHM: 1) correspond to C−C aliphatic and C=C aromatic carbons, respectively. Carbon bound to nitrogen (C−N) was assigned to 285.71 (FWHM: 1.44). The broad peak located at 288.88 eV (FWHM: 1.66) could be assigned to the combination of the N=C=O group and the gold bonded N=C=O group (NHCOOM). In Figure 2.8b, the N 1s spectrum has deconvoluted to two peaks which at 399.54 eV (FWHM: 1.34) and 400.06 eV (FWHM: 1.31), corresponding to the N=C=O groups and NHCOOM, respectively. As explained earlier, 400.7 eV were found to be NHCOOM, and 400.0 eV could be assigned N=C=O.[38, 47]

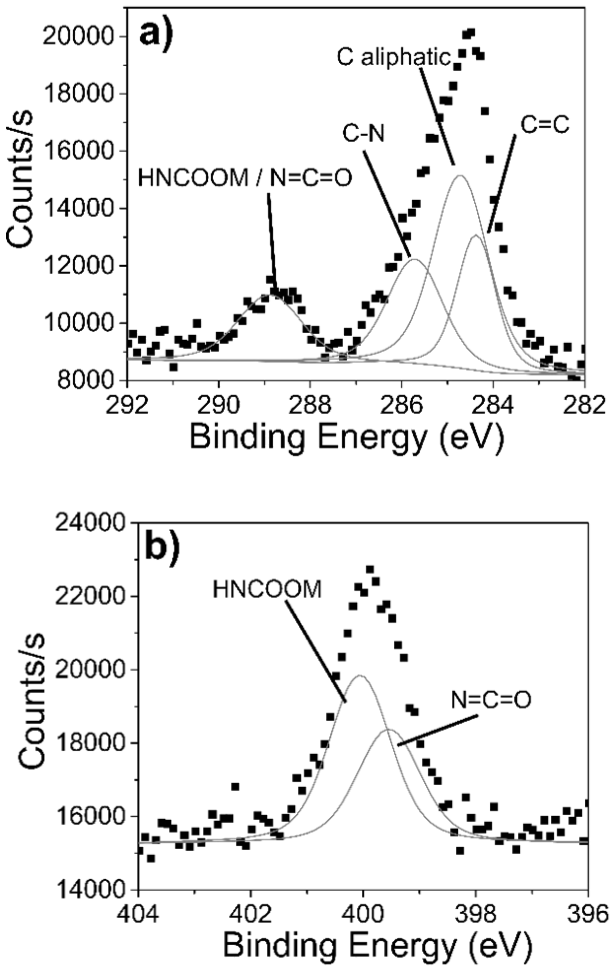

Figure 2.8. XPS spectra of a) C 1s and b) N 1s after PDI incubation.

2.2.2. Polymeric Methylene Diphenyl Diisocyanate Gold Surface Interaction

An XPS point analysis of the p-MDI incubated gold surface is shown in Figure 2.9. In Figure 2.9a, the XPS spectra of the C 1s has deconvoluted into five peaks. The peaks at 284.22 eV (FWHM: 0.85) and 284.75 eV (FWHM: 0.92) correspond to C=C aromatic and C−C aliphatic carbons, respectively. The binding energies of C-N and C-O are assigned to 285.66 eV (FWHM: 0.97) and 286.51 eV (FWHM: 1.13). The broad binding energy peak at 288.82 eV (FWHM: 1.97) could correspond to a combination of the N=C=O group and the gold bonded N=C=O group (NHCOOM). In Figure 2.9b, the N 1s spectra has deconvoluted to two peaks that are at 399.96 eV (FWHM: 1.03) and a broad peak at 400.45 eV (FWHM: 2.42), corresponding to the N=C=O functional group and NHCOOM, respectively. Also, according to Tardio et al., 400.7 eV and 400.0 eV were attributed to NHCOOM and N=C=O, respectively.[38, 47]

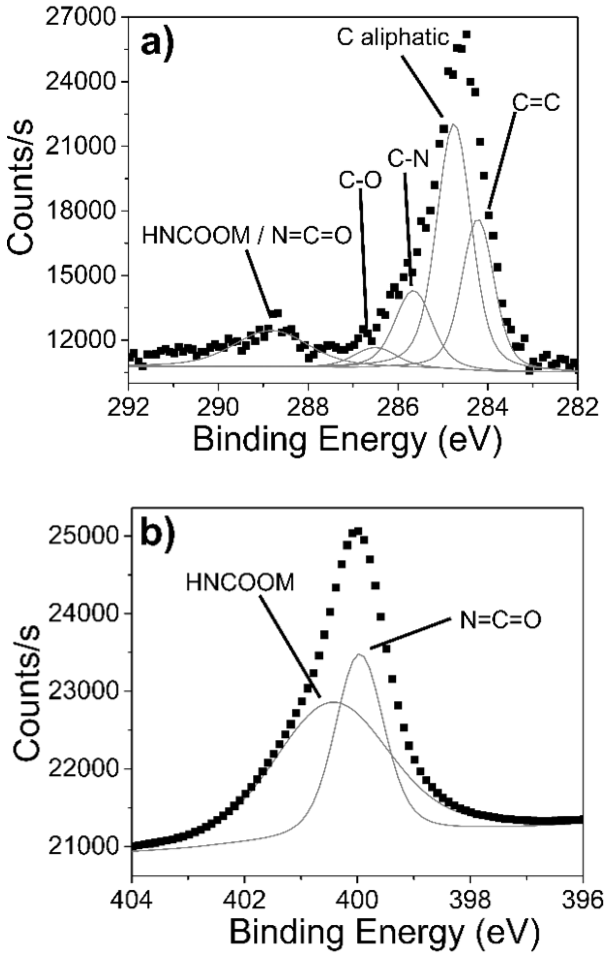

Figure 2.9. XPS spectra of a) C 1s and b) N 1s after p-MDI incubation.

2.2.3. Hexamethylene Diisocyanate Gold Surface Interaction

Figure 2.10 shows the XPS spectra obtained after the incubation of the gold surface with HDI. In Figure 2.10a, the C 1s spectrum is split into five peaks. C−C aliphatic carbons peak are present at 284.99 eV (FWHM: 1.2). There are two adjacent binding energy peaks of the C-N bond 285.99 eV (FWHM: 1.46) and C−O 287.56 eV (FWHM: 0.5). The narrow binding energy peak at 288.72 eV (FWHM: 0.72) and the broad peak at 289.03 eV (FWHM: 1.57) could correspond to the N=C=O groups and gold bonded N=C=O group (NHCOOM), respectively. In Figure 2.10b, the N 1s spectra split into two peaks. The peak at 399.64 eV (FWHM: 1.35) corresponds to the N=C=O functional groups, and a broad peak at 400.43 eV (FWHM: 1.78) is assigned to NHCOOM.[38, 47]

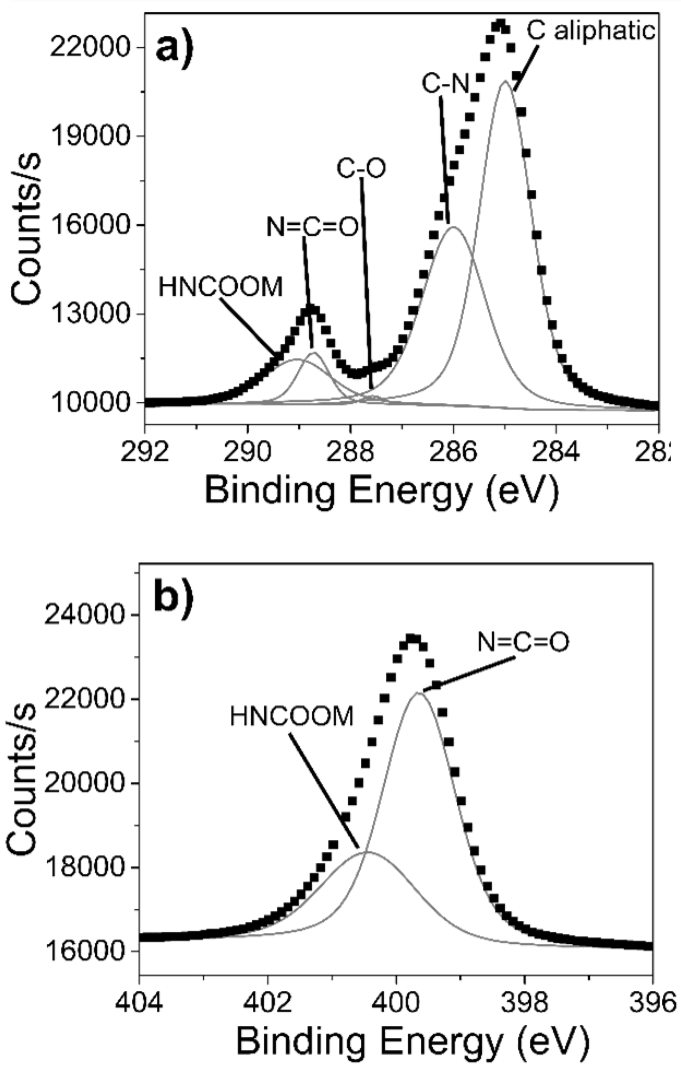

Figure 2.10. XPS spectra of a) C 1s and b) N 1s after HDI incubation.

As a discussion of the XPS C 1s point spectra, almost all binding energy peaks of the main urethane bonds (C-O, C-N, NCOOM, and NCO) have been assigned. In addition, NHCOOM and NCO binding energy peaks were seen as two adjacent peaks only in HDI incubation. The HDI is a linear aliphatic structure that could tend to show well-ordered behavior like thiols/silane molecules on the surface. Additionally, all XPS N 1s point spectra show the similarities of the two binding energy peaks that could be attributed to NHCOOM and NCO.

Table 2.1. The comparative result of C=C and C-C, C 1s XPS in the interaction between the gold surface and isocyanate.

Isocyanate source	C=C	C-C
PDI	284.37 eV FWHM:1 Area: 5552	284.72 eV FWHM:1.42 **Area: 11264**
p-MDI	284.22 eV FWHM:0.85 Area: 7022.6	284.75 eV FWHM:0.92 **Area: 12244.7**
HDI	-	284.99 eV FWHM:1.2 **Area: 15548.6**

Table 2.1 represents the comparative results of the C 1s XPS point spectra binding energies, FWHM, and area values in the interaction between the gold surface and isocyanates. p-MDI, which has two phenyl groups, has the highest C=C bonding energy area (7022.6 CPS.eV.) while HDI has the highest C-C bonding energy area value (**15548.6 CPS.eV.**).

Table 2.2. The comparative result of C-N and C-O, C 1s XPS in the interaction between the gold surface and isocyanate.

Isocyanate source	C-N	C-O
PDI	285.71 eV FWHM:1.44 **Area: 6224.61**	-
p-MDI	285.66 eV FWHM:0.97 **Area: 4085.86**	286.51 eV FWHM:1.13 Area: 1206.91
HDI	285.99 eV FWHM:1.46 **Area: 10337.3**	287.56 eV FWHM:0.5 Area: 172.59

HDI has the highest C-N binding energy area value (10337.3 CPS.eV) while PDI and p-MDI have 6224.61 CPS.eV and 4085.86 CPS.eV, respectively. These results show that the interaction of the N=C=O groups with the gold surface decreases while the aromatic structure and rigidity increase (Table 2.2). PDI does not exhibit a C-O binding energy peak, which could explain why C-O binding energy has the smallest peak, as seen by the p-MDI (area: 1206.91 CPS.eV) and HDI (area: 172.59 CPS.eV) XPS spectra (Table 2.2).

Table 2.3. The comparative results of N=C=O and NHCOOM, C 1s XPS in the interaction between the gold surface and isocyanate.

Isocyanate source	N=C=O	NHCOOM
PDI	288.88 eV FWHM:1.66 Area: 4509.61	
p-MDI	288.82 eV FWHM:1.97 Area: 3889.07	
HDI	288.72 eV FWHM:0.72 Area: 1470.97	289.03 eV FWHM:1.57 Area: 2763.1

Table 2.3 represents the comparative results of the C 1s XPS point spectra high binding energy region, FWHM, and area values in the interaction between the gold surface and isocyanates. These two peaks can be attributed to N=C=O and HNCOOM, which originate from two different types of isocyanate groups. The N=C=O and NHCOOM binding energies of p-MDI and PDI present a single identical binding energy and area value. HDI has deconvoluted to two peaks at a higher energy region. It is assumed that one NCO group interacts with the surface while the other terminal NCO group remains unreacted, since the N=C=O and HNCOOM 1470.97 and 2763.1 area values are close to each other (also see: 2.2.5. Theoretical Calculations section).

Table 2.4. The comparative results of N 1s XPS in the interaction between the gold surface and isocyanates.

Isocyanate source	N=C=O	NHCOOM
PDI	399.54 eV FWHM: 1.34 **Area: 4848.27**	400.06 eV FWHM: 1.31 **Area: 6999.14**
p-MDI	399.96 eV FWHM:1.03 **Area: 2849.48**	400.45 eV FWHM: 2.42 **Area: 4994.48**
HDI	399.64 eV FWHM:1.35 **Area: 9472.08**	400.43 eV FWHM: 1.78 **Area: 4454.03**

Since there are two binding energy peaks originating from different types of isocyanates, the corresponding binding energy profile should be present in the N 1s spectrum. The N 1s spectra split into two peaks. As a similar result, the highest N 1s N=C=O binding energy area belongs to HDI, with 9472.08 CPS.eV, while the lowest value belongs to p-MDI, with 2849.48 CPS.eV. This result shows that HDI is the most yielded and stable structure in the functionalization of the gold surface with N=C=O (Table 2.4).

In conclusion, the results show the functionalization of the gold surface with the N=C=O by incubation with all isocyanate sources (PDI, p-MDI, and HDI) in the presence

of the dibutyltin dilaurate. However, in the experimental conditions, the C 1s and N 1s binding energy peaks of the HDI molecule have become deconvoluted and well-defined.

2.2.4. Hexamethylene Diisocyanate Gold Surface Interaction in the Presence of DABCO and DBTDL

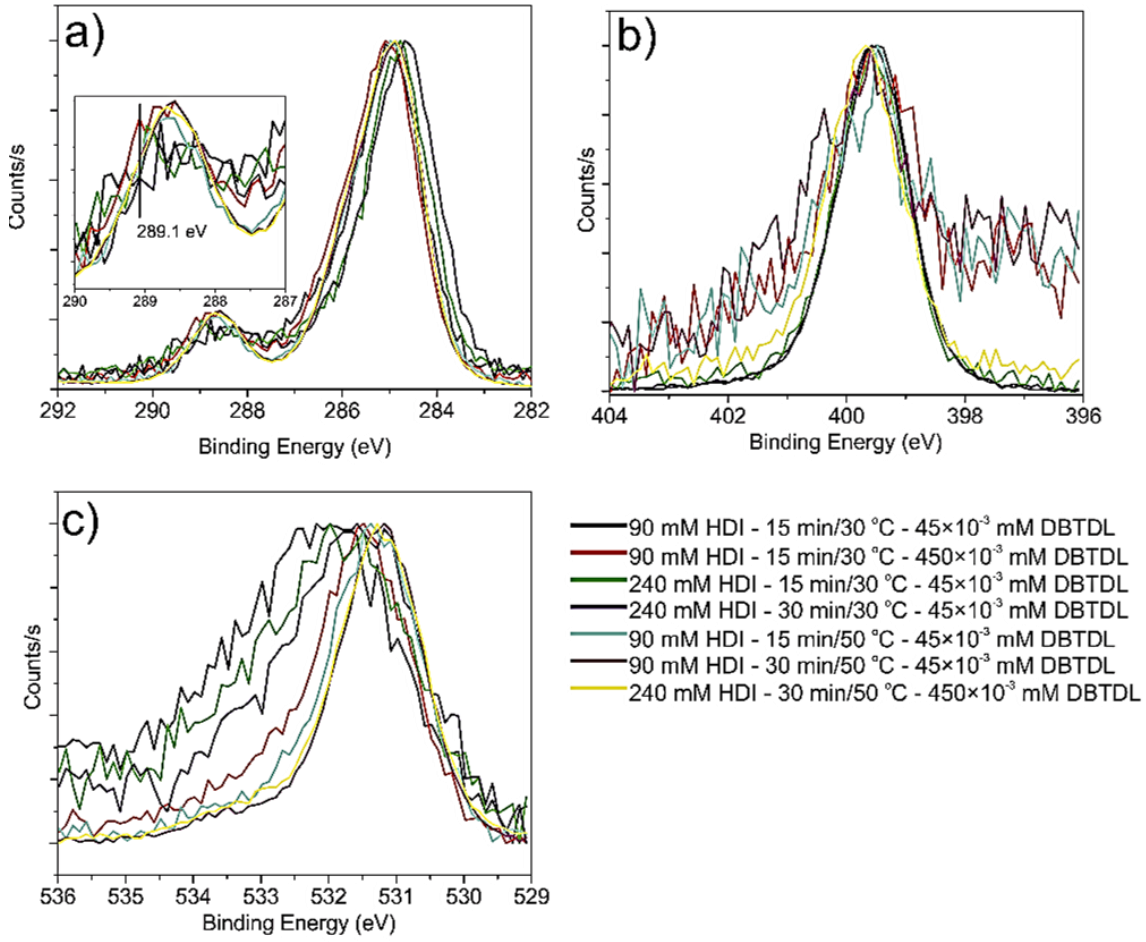

Figure 2.11 XPS spectra of a) C 1s, b) N 1s, and c) O 1s after various conditions of HDI incubations (DBTDL).

Figure 2.11 shows the XPS spectra obtained after the incubation of the gold surface with various condition of HDI incubations in the presence of the DBTDL catalyst. In general, the XPS spectra obtained after various conditions of HDI incubations show that high DBTDL and HDI concentrations give a high yield gold isocyanate interaction at 30°C, while the efficiency of the gold isocyanate interaction decreases at 50°C. 289.1 eV is determined as a reference value, since a high binding energy peak indicates a metal isocyanate interaction in C 1s XPS spectrum. Therefore, it can be assumed that the red

spectrum has the highest count/s value in Figure 2.11a. In addition, the XPS spectra of N1s and O1s, which are shown respectively in Figures 2.11a and c, demonstrate that the peak shape and count/s value are suitable for obtaining the binding energies of the isocyanate/gold interaction. As a result, incubation at 30°C for 15 minutes in the presence of 90 mM HDI and 4.5x10-4 mM DBTDL could be considered the optimum conditions.

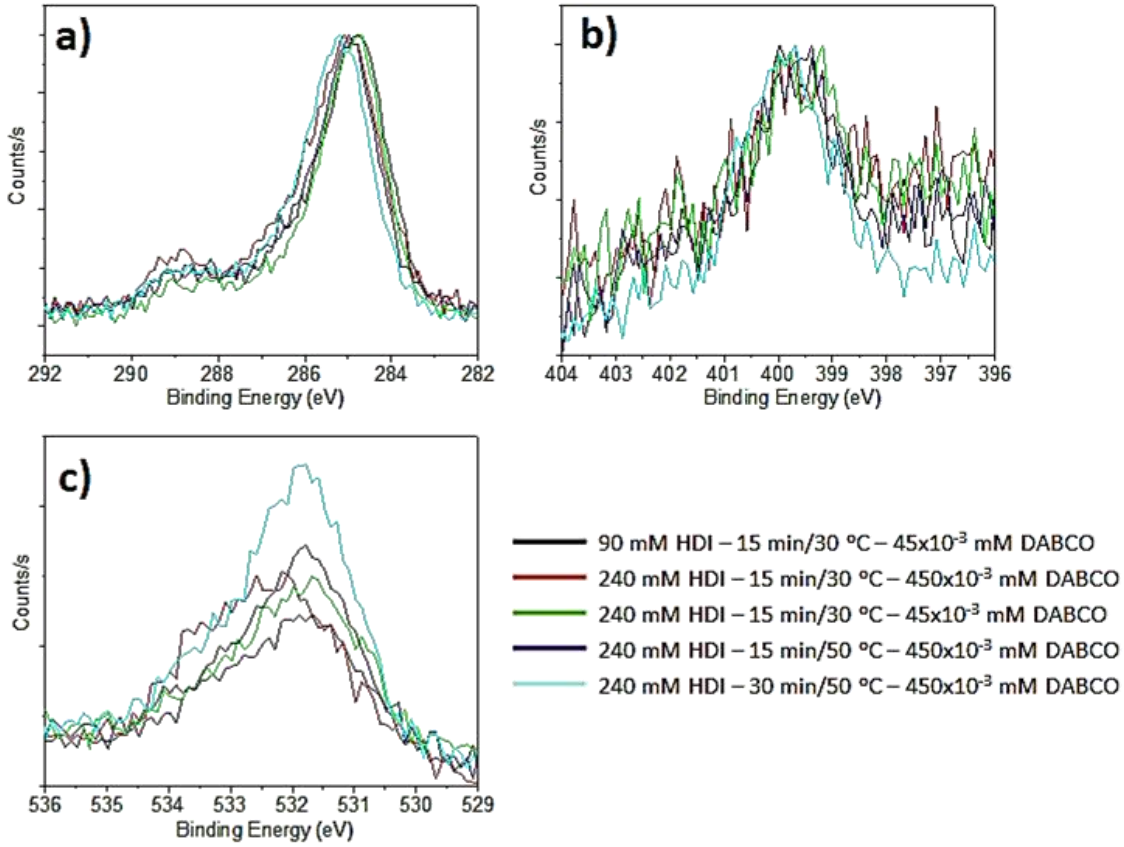

Figure 2.12 XPS spectra of a) C 1s, b) N 1s and c) O 1s after various condition of HDI incubations (DABCO).

Figure 2.12 shows the XPS spectra obtained after the incubation of the gold surface after the various conditions of HDI incubations in the presence of the DABCO catalyst. As the DBTDL XPS spectra results show, high HDI and catalyst concentrations give a high yield isocyanate/gold interaction; mostly 240 mM HDI and $4.5x10^{-4}$ mM DABCO concentrations were selected. Since 289.1 eV is assumed as a reference value of the isocyanate/gold interaction in the C 1s XPS spectrum, it can be assumed that the red spectrum has the highest count/s value in Figure 2.12a. In addition, the XPS spectra of N 1s and O 1s are shown in Figures 2.12a and c, respectively. The N 1s XPS spectrum at various concentrations appears to have identical peak shapes and count/s values while the

red XPS spectrum of O 1s may indicate that the isocyanate/gold interaction is fitting for obtaining binding energies. As a result, incubation at 30°C for 15 minutes in the presence of 240 mM HDI and 450x10^{-3} mM DABCO could be assumed as the optimum conditions.

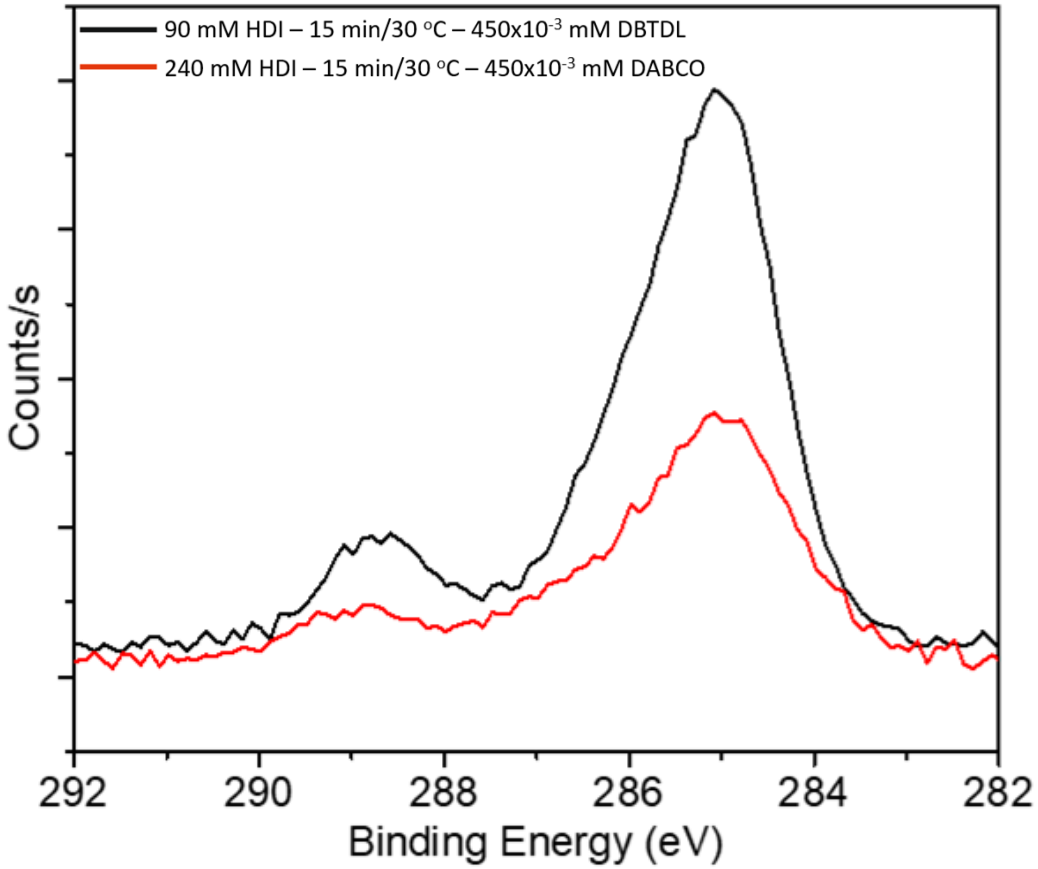

Figure 2.13 Comparison XPS spectra of C 1s after optimum conditions of DBTDL and DABCO.

Figure 2.13 shows the comparison of the XPS spectra obtained after the incubation of the gold surface with optimum conditions of HDI incubations in the presence of DABCO and DBTDL catalysts. The compared XPS results show that XPS incubation in the presence of the DBTDL catalyst has a higher count/s. However, peak fitting was applied to both XPS results (DBTDL and DABCO) for more detailed analysis and comparison, as seen in Figures 2.14 and 2.15.

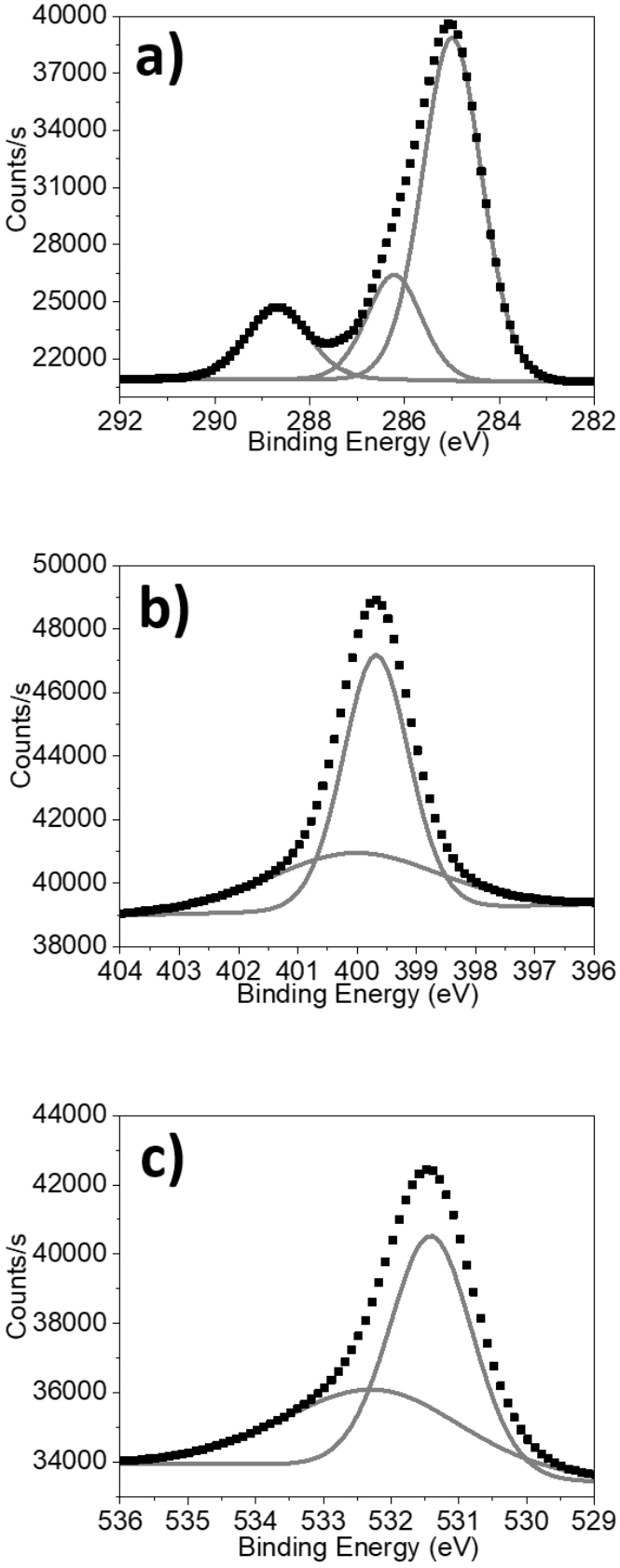

Figure 2.14 XPS spectra of a) C 1s, b) N 1s, and c) O 1s after optimum conditions of HDI incubation (DBTDL).

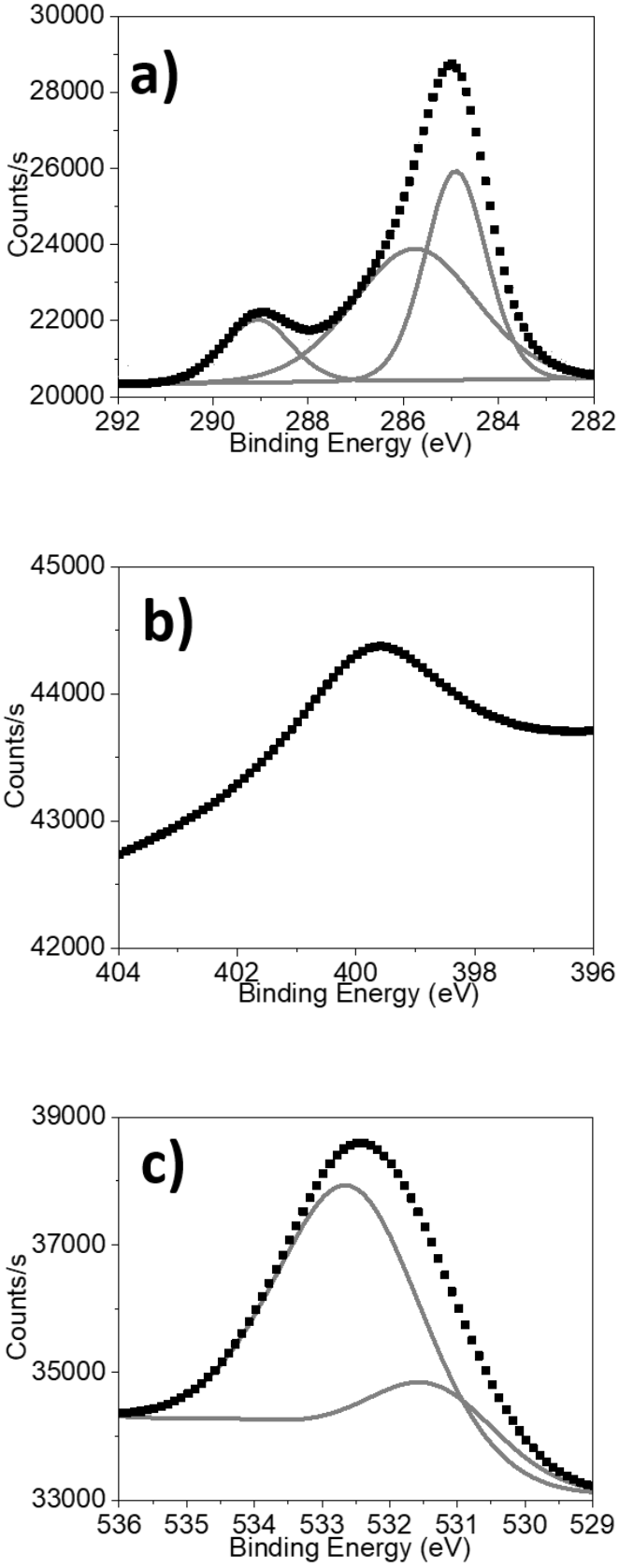

Figure 2.15 XPS spectra of a) C 1s, b) N 1s, and c) O 1s after optimum conditions of HDI incubation (DABCO).

Figure 2.14 shows the XPS spectra obtained after the incubation of the gold surface with HDI in the presence of DBTDL. In Figure 2.14a, the C 1s spectrum is split into four peaks. C−C aliphatic carbons peak at 285 eV (FWHM: 1.47). Additionally, there are two adjacent binding energy peaks of the C-N bond 286.22 eV (FWHM: 1.36) and C−O 287.39 eV (FWHM: 0.64). The broad binding energy peak at 288.68 eV (FWHM: 1.54) could correspond to a combination of the N=C=O group and the gold bonded N=C=O group (NHCOOM). In Figure 2.14b, the N 1s spectra is split into two peaks. The peak at 399.68 eV (FWHM: 1.31) corresponds to the N=C=O functional groups, and a broad peak at 400.05 eV (FWHM: 3.37) is assigned to NHCOOM.[38, 47] In Figure 2.14c, the O 1s spectra split into two peaks. The peak at 531.4 eV (FWHM: 1.44) corresponds to the N=C=O functional group, and a peak at 532.2 eV (FWHM: 3.2) could assigned to C=O functional group.

Figure 2.15 shows the XPS spectra obtained after the incubation of the gold surface with HDI in the presence of DABCO. In Figure 2.15a, the C 1s spectrum is split into three peaks. There is a C−C aliphatic carbons peak at 284.9 eV (FWHM: 1.52). Additionally, there are binding energy peaks of the C-N bond 285.77 eV (FWHM: 3.04). The broad binding energy peak at 289.07 eV (FWHM: 1.65) may correspond to a sum of the N=C=O group and the gold bonded N=C=O group (NHCOOM). In Figure 2.15b, the N 1s spectra peak at 399.73 eV (FWHM: 3.93) corresponds to the N=C=O functional group. In Figure 2.15c, the O 1s spectra split into two peaks. The peak at 531.35 eV (FWHM: 2.26) corresponds to the N=C=O functional group, and a peak at 532.56 eV (FWHM: 2.52) could assigned to C=O functional group.[38, 47]

The HDI is a linear aliphatic structure that could tend to show well-ordered behavior like thiols/silane molecules on the surface. As a general discussion of the XPS C 1s point spectra in the presence of DBTDL, the binding energy peaks of the main urethane bonds (C-O, C-N, NCOOM, and NCO) have been assigned. In Table 2.5, the combinations of the NHCOOM and NCO binding energy peak areas have a twofold higher area value in the DBTDL (6279.84 CPS.eV.) catalyst when compared to the DABCO (2957.83 CPS.eV.) catalyst. Additionally, all XPS O 1s point spectra show similar two binding energy peaks that could be attributed to the N=C=O and C=O functional groups.

Table 2.5. The comparative results of C 1s XPS spectra after optimum conditions of DBTDL and DABCO.

Catalyst source	**C-C**	**C-N**	**C-O**	**N=C=O / NHCOOM**
DBTDL	285 eV FWHM: 1.47 Area: 28748.24	286.22 eV FWHM: 1.36 Area: 8107.43	287.39 eV FWHM: 0.64 Area: 415.78	288.68 eV FWHM: 1.54 Area: 6279.84
DABCO	284.9 eV FWHM: 1.52 Area: 9023.97	285.77eV FWHM: 3.04 Area: 11408.79	-	289.07 eV FWHM: 1.65 Area: 2957.83

The presence of the DBTDL catalyst has a higher C-C binding energy area value (28749.24 CPS.eV) while the DABCO catalyst has a binding energy value of 9023.97 CPS.eV. These results may be because the interaction of the N=C=O groups with the gold surface increases with the use of the DBTDL catalyst. The DABCO catalyst does not exhibit a C-O binding energy peak, which could explain why the C-O binding energy has the smallest peak, as seen by the DBTDL catalyst of (area: 415.78 CPS.eV) the XPS spectra (Table 2.5).

Table 2.6. The comparative results of N 1s XPS spectra after optimum conditions of DBTDL and DABCO.

Catalyst source	**N=C=O**	**NHCOOM**
DBTDL	399.68 eV FWHM: 1.31 Area: **11347.36**	400.05 eV FWHM: 3.37 Area: 6533.52
DABCO	399.73 eV FWHM: 3.93 Area: 8051.17	-

The N 1s spectra split into two peaks in the DBTDL catalyst but only a single peak in the DABCO catalyst. As a result, the highest N 1s N=C=O binding energy area

belongs to the DBTDL catalyst, with 11347.36 CPS.eV. This result shows that the presence of DBTDL is the higher yield in the functionalization of the gold surface with N=C=O (Table 2.6).

Table 2.7. The comparative results of O 1s XPS spectra after optimum conditions of DBTDL and DABCO.

Catalyst source	**C=O**	**N=C=O**
DBTDL	532.2 eV FWHM: 3.2 Area: 7872.59	531.4 eV FWHM: 1.44 Area: **10745.23**
DABCO	532.56 eV FWHM: 2.52 Area: **11186.77**	531.35 eV FWHM: 2.26 Area: 3544.65

The results show the functionalization of the gold surface with N=C=O after optimum incubation conditions with different catalyst sources (DABCO and DBTDL). However, under experimental conditions, the binding energy peaks of C 1s and N 1s in the presence of the DBTDL catalyst are fitted and well-defined when compared to those of the DABCO catalyst. As a result, incubation at 30°C for 15 minutes in the presence of 90 mM HDI and $450x10^{-3}$ mM DBTDL is considered the optimum conditions. In addition, theoretical calculations of adsorption of the HDI molecule on the Au (111) surface were conducted.

2.2.5. Theoretical Calculations of Adsorption of the HDI Molecule on the Au (111) Surface

Figure 2.16a shows the adsorption scheme of HDI molecule of the NCO group aligned horizontally and vertically on the Au(111) surface. Also, possible adsorption sites are demonstrated in the top view of the Au with top-site, hexagonal closed packed site (hcp-site), face-centered cubic site (fcc site), and bridge site. To figure out the interaction

of a single HDI molecule with the surface, the NCO functional group individually interacts vertically and horizontally in each adsorption site.[41]

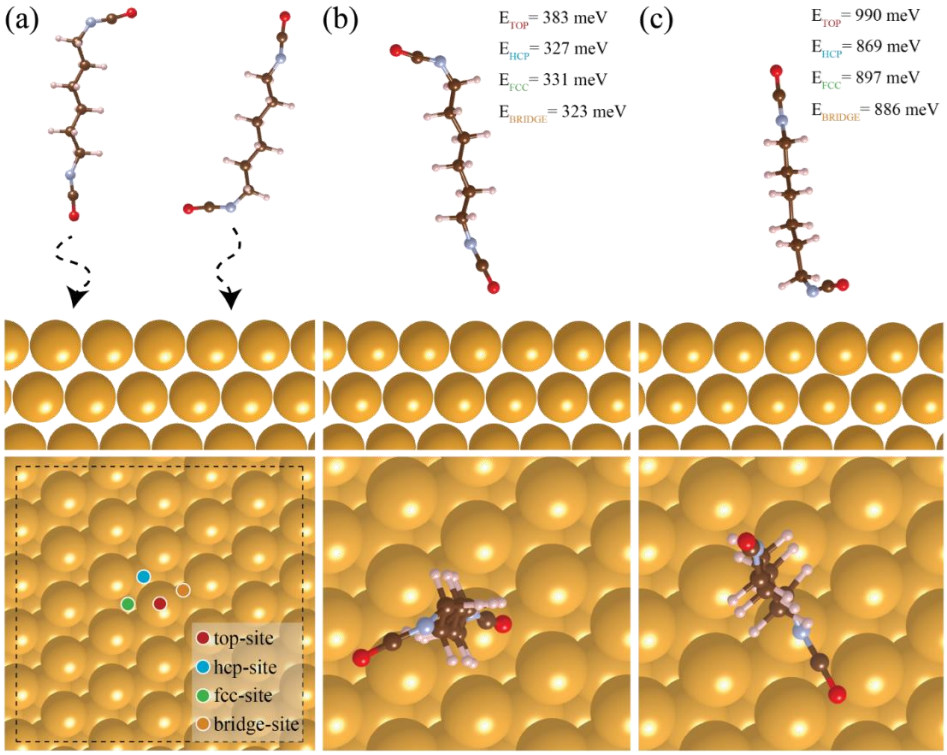

Figure 2.16. a) Scheme of HDI molecule of the NCO group aligned horizontally and vertically on the Au(111) surface. Possible adsorption sites in the top view of the Au (111) surface are indicated by red, blue, green, and orange dots. b and c) Top and side views of the adsorption of the NCO functional group over nitrogen and oxygen to the Au (111) surface and the binding energies calculated for the adsorption sites.

As in Figure 2.16b, when the NCO functional group is aligned vertically to the gold surface, the oxygen atom interacts with the adsorption sites of the surface. The calculated binding energies for the vertically aligned NCO group are top-site, hexagonal closed packed site (hcp-site), face-centered cubic site (fcc site), and bridge site (383 meV, 327 meV, 331 meV, and 323 meV, respectively). As seen in Figure 2.16c, when the NCO functional group is aligned parallel to the gold surface, the nitrogen atom interacts with the adsorption sites of the surface. The calculated binding energies for the aligned parallel are top-site, hexagonal closed packed site (hcp-site), face-centered cubic site (fcc site), and bridge site (990 meV, 869 meV, 897 meV, and 886 meV, respectively). In addition, when the isocyanate group is aligned vertically to the gold surface vertical distance

between the O atom and outermost Au atomic plane is 2.87 angstroms. On the other hand, the isocyanate group is aligned horizontally to the gold surface vertical distance between the N atom and outermost Au atomic plane is 2.60 angstroms.

The further DFT calculation results are shown in Figure 2.17. These results show that the binding energy between the N atom and the top-site of the Au (111) (990 meV) is much higher than the Van der Waals type interaction (35 meV) energy, while the binding energy is lower than the Au-S (1700 meV) bond.[48, 49] In addition, there is a difference of approximately 800 meV between N=C=O and NHCOOM in binding energy values in the XPS spectra of N 1s (Figure 2.10). The difference is consistent with the calculated values of the binding energies between the N atom and top-site Au (111) (990 meV).

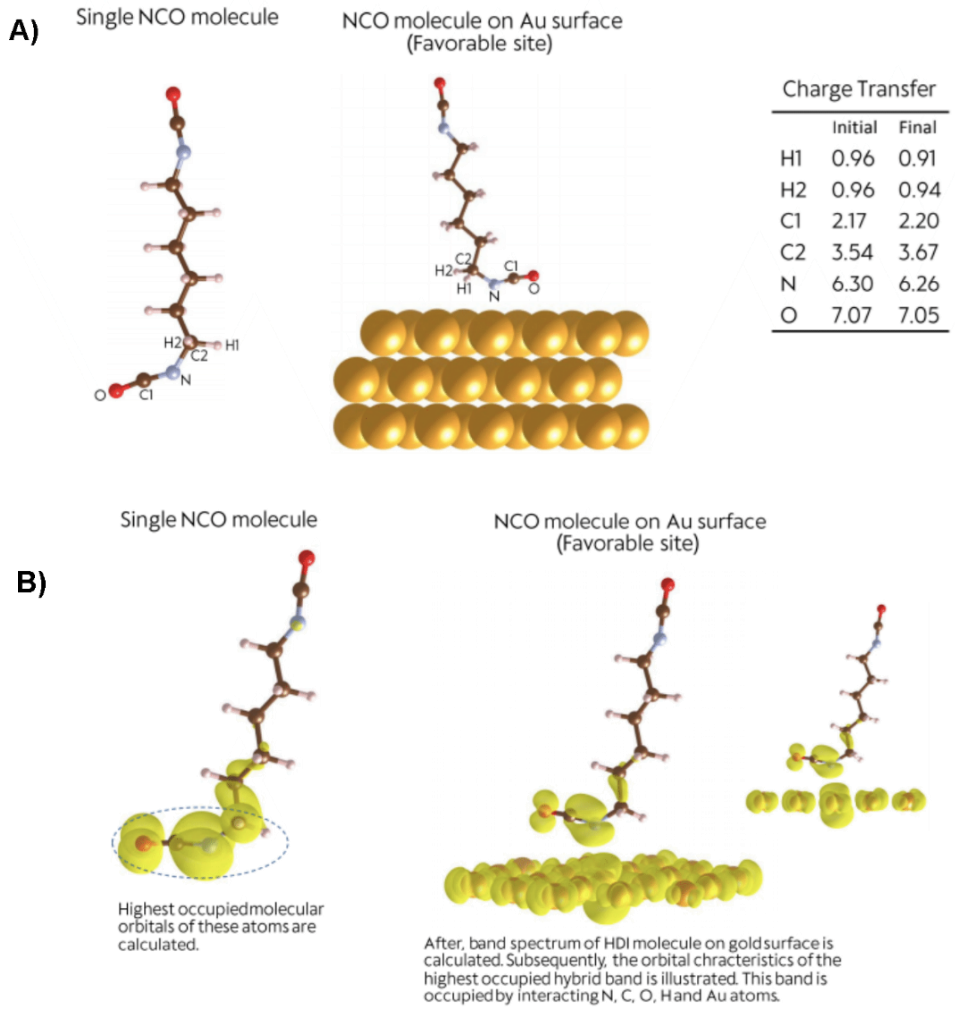

Figure 2.17. a) Calculated charge transfer characteristic of the HDI molecule on the Au surface and b) Calculated band spectrum of the HDI molecule and band occupancy of Au by N, C, O and H atoms.

Calculations show the orbital character of the bonding state, the charge density of the molecule, and the intimate contact point of the surface is reorganized to form bonding. The below Figure 2.17a summarizes the charge density change of surface interacting atoms C, N, O, H. The changes of the surface interacting atoms were found to be marginal as compared to their neutral states. Moreover, the Bader charge analysis reveals that there is no charge transfer between the molecules and surface. Therefore, it can be concluded that the bond has no ionic character. In below Figure 2.17b, the highest occupied molecular orbital of surface interacting atoms was shown, and at the onset of the interaction, the gold band structure is occupied by N, C, O. This overlapping refers to the further DFT analysis points out that the bond between N and Au is partially covalent and metallic character.

As a general discussion of the theoretical calculations of adsorption of the HDI molecule on the Au (111) surface: It has been found that the most favorable adsorption site for the calculated binding energies for both NCO functional groups aligned vertical and parallel are the top-site of the Au (111) surface. Also, when the NCO functional group is aligned parallel to the gold surface, the other terminal NCO group and aliphatic chain are positioned perpendicular to the surface and this is the most favorable energy configuration. The most favorable energy configuration leads to three main results:

i) one of the bifunctional aliphatic isocyanate groups interacts with the top-site of the Au (111) surface through the nitrogen atom,

ii) the other terminal isocyanate remains unreacted with the Au (111) surface and provides the possibility of further polymerization,[50] and

iii) Configuration can give a SAM-like well-ordered structure with Van der Waals interactions between adjacent aliphatic chains that are positioned perpendicular to the surface.

2.3. Conclusions

Surface modification changes the properties of the interface by creating SAM via Van der Waals interactions. Interface modification by using silane and thiol-based agents is the most common method used to obtain surface functionalization. Even though silane and thiol agents are a traditional surface functionalization method, the search for new surface functionalization agents always continues.

Isocyanate is an important functional group that reacts with all hydrogen-containing groups due to the resonance structure. In this chapter, an alternative to traditional interface modification has been investigated by using 1,4-Phenylene diisocyanate (PDI), polymeric methylene diphenyl diisocyanate (p-MDI), and hexamethylene diisocyanate (HDI) to find out most efficient and stable modifications on the gold surface. The C 1s XPS point spectra binding energy shows that p-MDI has the highest C 1s aromatic carbon binding energy area value while HDI has the highest C 1s aliphatic carbon binding energy area value (Table 2.1). In addition, HDI has the highest C-N binding energy area value, and PDI does not exhibit C-O binding energy peak (Table 2.2). Moreover, the N=C=O and NHCOOM binding energies of p-MDI and PDI present a single peak while HDI has deconvoluted to two peaks at a higher energy region (Table 2.3). Furthermore, the highest N 1s N=C=O binding energy area belongs to HDI while the lowest value belongs to p-MDI (Table 2.4).

The XPS point analysis showed that all sources of isocyanate could interact with the gold interface under a certain experimental condition. In addition, the most efficient surface functionalization was obtained with HDI. On the other hand, the XPS results showed that PDI and p-MDI have aromatic rings, they interact with few isocyanate groups on the gold surface due to their higher steric hindrance compared to linear HDI. Therefore, the binding energies of the isocyanate groups of the linear HDI molecule with the gold surface in the high energy region have a characteristic profile, which is compatible with the literature results.[38] This characteristic binding energy profile indicates that the interaction of N=C=O groups with the gold surface decreases as the aromatic structure and rigidity increase as similar to less stable aromatic structure-based thiol molecules.[32] In addition, it can be assumed that the CH_2 groups of the linear HDI molecule will provide a secondary interaction to obtain a well-ordered structure on the gold surface. Therefore, the HDI molecule was used as an isocyanate source in the following chapter. In addition, incubation at 30^{o}C for 15 minutes in the presence of 90 mM HDI and $450x10^{-3}$ mM DBTDL is considered as the optimum conditions.

The XPS point analysis results were supported by theoretical calculations of adsorption of the HDI molecule on the Au (111) surface. Binding energy of the most favorable energy configuration indicates that there is a much stronger force than the Van der Waals-type interactions when the NCO functional group is aligned parallel on Au (111) interface. Also, as seen in Figure 2.17, calculated results demonstrate that the bond between N and Au is of a partially covalent and metallic character.

The XPS and theoretical calculations results show that the isocyanate group interacts with the top-site of the Au (111) surface through the nitrogen atom, and the other terminal isocyanate remains unreacted with the Au (111) surface. In addition, SAM-like well-ordered structures between adjacent HDI molecules could occur. As a result of this chapter, the functionalization with isocyanate sources could pave the way for the preparation of a well-defined polymeric structure, which could serve as a biosensor platform.

CHAPTER 3

SURFACE-ASSISTED URETHANE POLYMERIZATION

Biosensors[51, 52] and implantable bioelectronic systems[53-55] have become important areas of research due to increasing interactions between living beings and electronic systems.[56] Determining, conserving, and maintaining the delicate balance at the interface between bio and electronic components is important to the success of the biosensor field.[57] Therefore, the interface is combined with metals or semiconductors, which are electronic components of bioelectronic systems, to produce a soft and stimulus-sensitive interface.[58-63] Basically, the permanence of achievement can be provided with the continuity of well-defined alternative interface studies. Consequently, the stimulus-sensitive interface has become an always up to date research field that needs to be constantly explored.

Biofouling caused by the irreversible adsorption of bio-macromolecules such as proteins and DNAs is one of the major challenges for the bioelectronic interface. As a result of non-specific binding problems encountered in antibody research protein microarray, detection platforms may generate false-positive signals. Therefore, protein sensing platforms can be provided by surface modification in antibody research without encountering the problem of non-specific binding that produces false-positive signals (Figure 3.1).

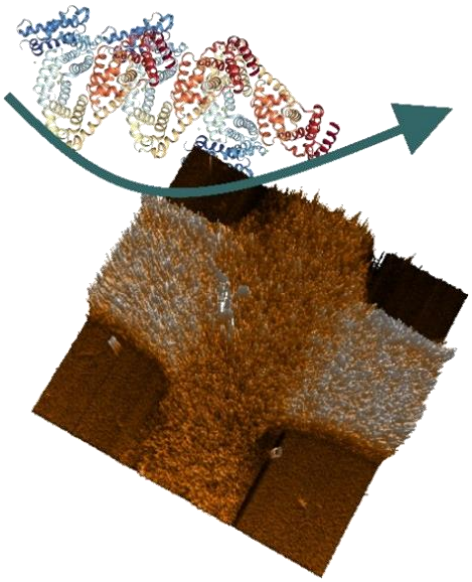

Figure 3.1 Representation of a bio-fouling surface.

As a general rule, ethylene glycol terminated alkanethiols prevent non-specific protein adsorption on the gold surface; however, the solely SAM layer has limited robustness.[64] Therefore *grafting from* methodologies for manufacturing bio-repellent polymer functionalized interfaces, like activators regenerated by electron transfer (ARGET) ATRP and surface-initiated atom transfer radical polymerization (SI-ATRP), have been developed.[65-68] Thus, the SI-ATRP methodology presented is an important and valuable method in surface and interface architecture. Generally, the SI-ATRP used to create the polymer brush on the surface is performed in the following two steps: (i) modification of the initiator on the surface and (ii) ATRP performed to obtain the polymer brush on the surface with air-free conditions. In the second stage, deoxygenation (airtight conditions) should be done using a sophisticated apparatus. In addition, a large amount of copper (Cu) catalyst is deposited on the resulting polymer brush; therefore, a long-washing step is often required for complete catalyst-removal[69]. Pinto et al. manufactured ultrathin polymethyl methacrylate brush gate insulators by using the ATRP method. The polymer brush presented good homogeneity and high capacitance that are used for low-voltage organic field-effect transistors (OFETs).[70] Ge et al. have demonstrated that modifying the Si surface with polystyrene brushes synthesized by SI-ATRP facilitates the manufacture of inkjet-printable OFETs.[71] Recently, Joh et al. reported that the metal-oxide Al_2O_3, ZrO_2, and SiO_2 dielectric materials were functionalized with non-fouling poly(oligo (ethylene glycol) methyl ether methacrylate) (POEGMA) brushes for biosensing applications. Also, the results demonstrate that POEGMA modified biosensor platforms show non-specific adsorption and improve the performance of sensing devices.[72, 64]

Tang et al. found that poly(oligo (2-alkyl-2-oxazoline) methacrylate) functionalized gold surfaces obtained with ATRP show antifouling properties that are characterized by surface plasmon resonance sensor interface.[73] As mentioned in literature studies, time-consuming degassing steps that restrict the applicability of SI-ATRP are the main drawback; thus, air-tolerant methodologies present a more applicable approach to SI-ATRP. Yeow et al. have examined novel studies involving the advantages and disadvantages of air-resistant controlled live radical polymerization methodologies.[74] Jeong et al. exhibited the air-tolerant SI-ARGET ATRP method for the polymerization of sulfobetaine acrylamide (SBAA) on various surfaces, and the poly(SBAA) brush on the gold surface has been reported to present 12-14% protein adsorption.[69] Furthermore,

Hong et al. produced ultra-low fouling gold surfaces through the polymerization of carboxybetaine (CB) by SI-ARGET ATRP.[75]

Although SI-ATRP and SI-ARGET ATRP are useful methods for obtaining polymer brushes on diverse surfaces, the methods require long, laborious polymerization stages, and a large number of chemicals consumed with purification steps can be considered a drawbacks for biosensor applications.[11, 69]

In this chapter, we have performed the surface-assisted (SurfAst) urethane polymerization that provides a polyurethane (PU) interface using the isocyanate-functionalized gold surfaces prepared in the *Chapter 2*. A novel, straightforward SurfAst methodology does not need air-tight conditions, degassing, costly catalysts, high amounts of chemicals, or tedious purification steps that may restrain the practicability of a large-area application of the biosensor interface.

3.1. Materials and Methods

11-Mercapto-1-undecanol, poly(ethylene glycol) (Mw: 1000 Da), 1,4 butanediol (1,4-BDO), hexamethylene diisocyanate (HDI), isophorone diisocyanate (IPDI), 1,4-Phenylene diisocyanate (PDI), acetone, ethanol, and DBTDL 95% were purchased from Sigma-Aldrich. Texas Red-conjugated bovine serum albumin (T-BSA) was purchased from Thermo Fisher. Atomic Force Spectroscopy was conducted by Nanosurf AFM (Stat0.2LAuD - k = 0.2 N/m, static force) and was used for topographical characterization and adhesion force mapping. The EFM measurement was carried out in contour mode (Multi75E-G - k = 3 N/m, dynamic force, tip lift: 40 nm), at room temperature. Quanta 250 FEG scanning electron microscope was used for examining the gold surface morphology. Raman spectrum (MonoVista-Princeton Instruments) were recorded using 532 nm laser to investigate polyurethane (PU) functional groups on the surface. Infrared measurements were carried out by using PerkinElmer Spectrum 100 FTIR with VeeMAX III Variable Angle Specular Reflectance Accessory at variable angle reflectance (ZnSe p-polarizer) in a spectral range between 1000 and 3600 cm^{-1}. XPS analyses were performed at a pass energy of 30 eV. An Al Kα monochromatic (1486.68 eV) beam was used with a spot size of 300 μm (10 numbers of scans).

Surface passivation procedure: Gold substrates (1 cm^2) were cleaned by RCA cleaning. For gold surface passivation, 11-Mercapto-1-undecanol was used.

Polydimethylsiloxane (PDMS) stamp (Figure 3.2) was incubated in 1 mM 11-mercapto-1-undecanol for 5 minutes in an ethanolic solution. After the stamp was dried by N_2, it was located by applying mild pressure to the gold surface for 5 min. The gold surface was rinsed with EtOH.

SurfAst urethane polymerization general procedure: Isocyanate source (HDI, IPDI, or PDI) and 1,4-BDO concentrations were prepared 80 mM in the acetone solutions. DBTDL was added to the acetone solutions as the catalyst (4.5×10^{-2} mM) in the SurfAst urethane polymerization. The first step of passivated gold was incubated with isocyanate source solutions at 40°C for 20 minutes. The second step of passivated gold was incubated with 1,4-BDO solutions at 40°C for 20 minutes. SurfAst urethane polymerization was carried out with the eight-step sequential incubation of an isocyanate source and 1,4-BDO. After every step, the gold surface was sonicated with acetone.

Antifouling assay: After SurfAst urethane polymerization, PEG 1000 was grafted on the PU interface, and an antifouling study was performed (Figure 3.3). To understand the antifouling property of the PEG 1000-end PU interface, the gold surface was incubated with T-BSA (1 mg/mL in 1× PBS) for 3 hours at ambient temperature. After incubation with BSA, the gold surface was rinsed with plenty of 1× PBS. Zeiss fluorescence microscopy was utilized for fluorescence imaging with an exciting wavelength of 541 nm.

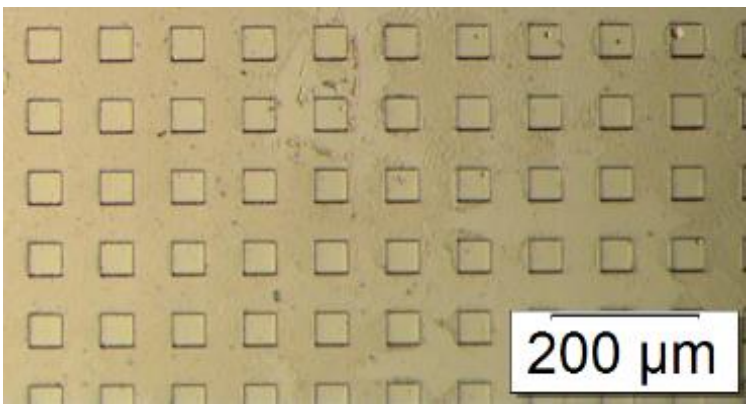

Figure 3.2 Microscope image of PDMS.

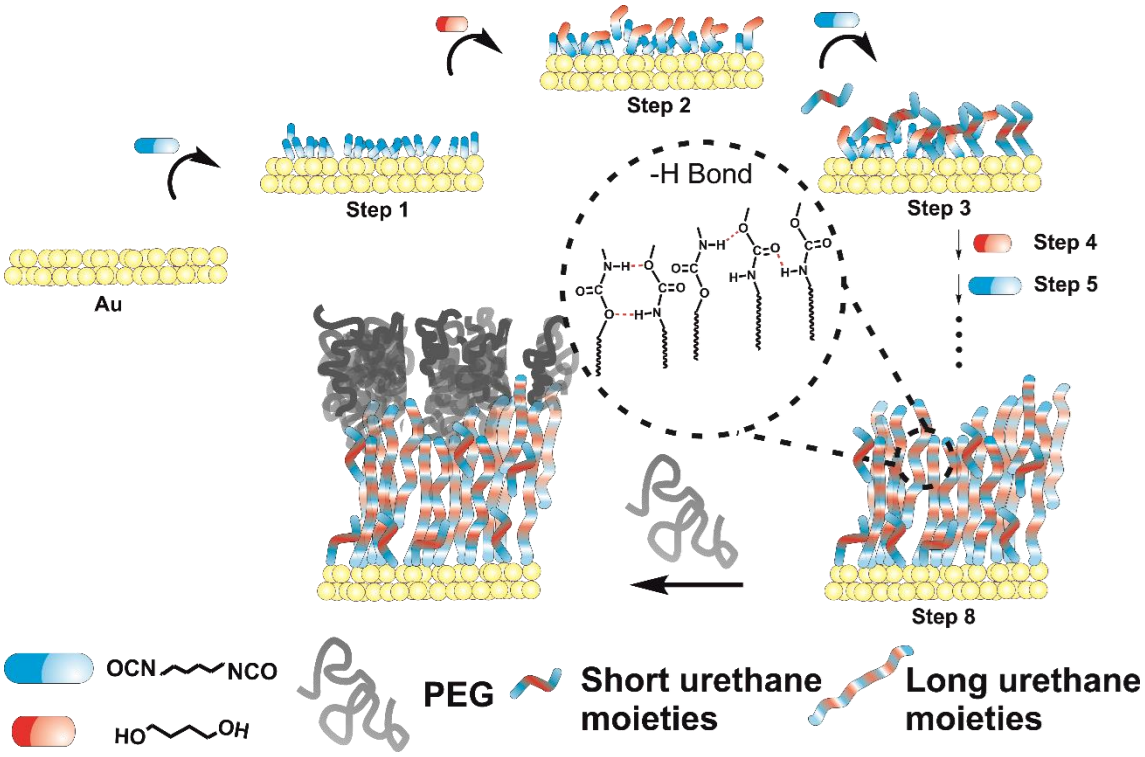

Figure 3.3 Illustration of SurfAst urethane polymerization for HDI and 1,4-BDO system.[41]

Figure 3.3 shows the SurfAst urethane polymerization. After RCA cleaning, the gold surface was incubated with HDI in the first step. At the end of the first step, one terminal isocyanate interacted with the gold surface while the other remained unreacted on the gold surface (See: *Chapter 2*). In the second step, the surface was incubated with 1,4-BDO, and the first urethane bond formed on the gold surface. After each step, the gold surface was rinsed with plenty of acetone to remove unbounded HDI and 1,4-BDO monomers. After the sequential incubation of HDI and 1,4-BDO, an interface was obtained by short and long urethane moieties at the end of the eighth step. The interface had a mixed secondary interaction involving at least three hydrogen bonds (see FTIR section). In addition, PEG 1000 could be covalently grafted onto the NCO-end polyurethane interface to obtain an antifouling surface.[41]

3.2. Results and Discussions

To determine the optimum step number, the gold surface was incubated in the HDI solution in the first step. As a result of this process, HDI monomers interacted on the gold surface. In the next step, the gold surface was incubated in the 1,4-BDO solution.

As a result of this process, one urethane group was theoretically formed on the surface; this process was denoted as two steps. Figure 4.4 shows the XPS chemical mapping results of C, N, O, and Au within four steps, six steps, and eight steps. The XPS chemical mapping of the PU interface with different step numbers is shown in Figures 4.4 a−d. Green, blue, light blue, and red regions refer to the sum concentration distributions of C 1s, N 1s, O 1s, and Au 4f of the PU interface on the gold surface. The chemical abundance of carbon, oxygen, nitrogen, and gold was analyzed based on the ratio of black to colored regions, demonstrating that carbon, oxygen, nitrogen, and gold existed on the cover on the surface within various abundances in four, six, and eight steps. The major difference in chemical abundance according to the step number was determined as Au 4f. While Au 4f chemical abundance was 0.971 area units in four steps, it decreased to 0.575 area units in six steps and reached 0.901 units in eight steps (Figure 3.4d).

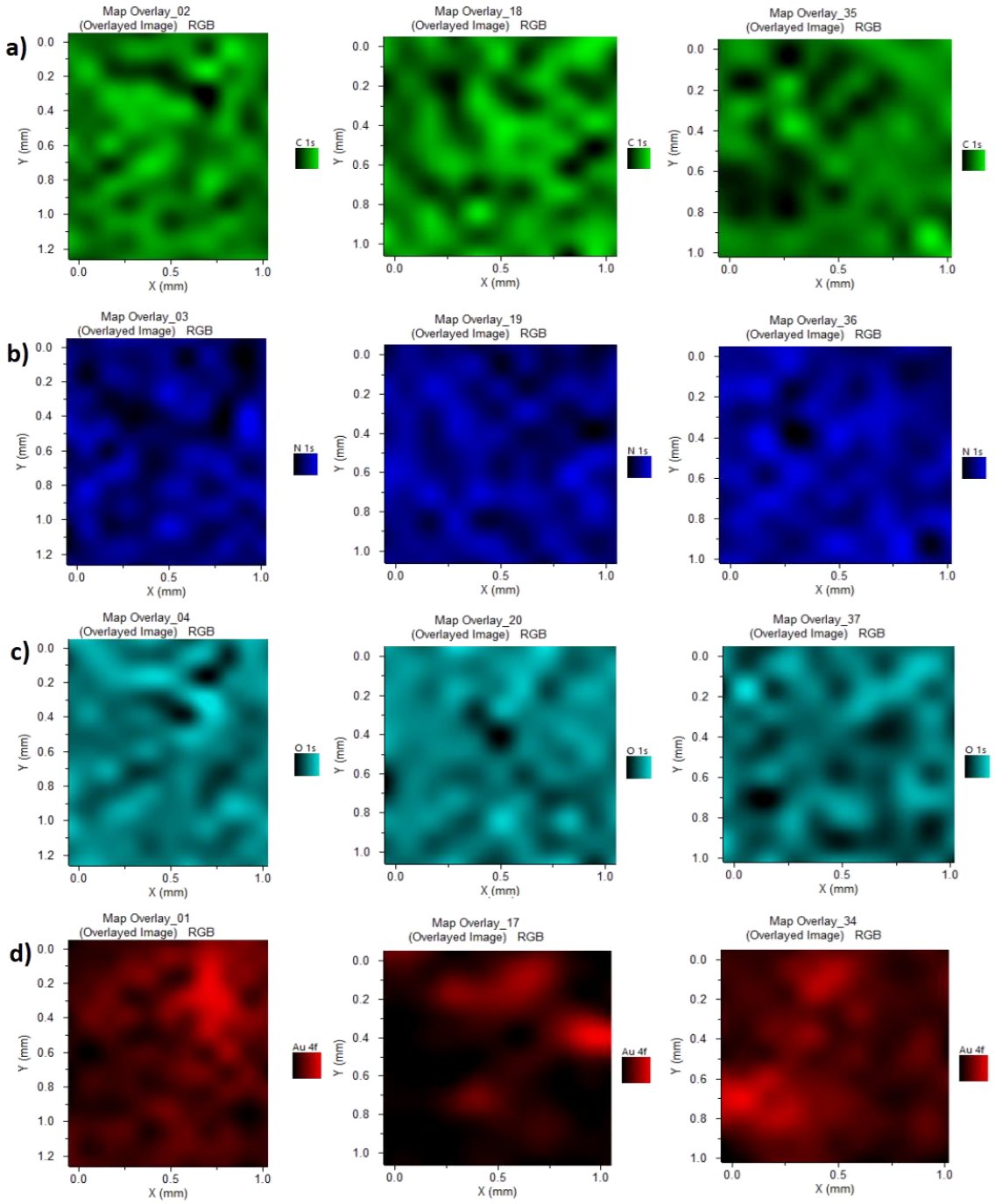

Figure 3.4 XPS chemical mapping results of a) C, b) N, c) O, and d) Au (left: four steps, middle: six steps, right: eight steps).

Figure 3.5 and Figure 3.6 depict the XPS binary chemical mapping results of a) Au-C, b) Au-N, c) Au-O, d) C-N, e) N-O, and f) C-O and XPS tertiary chemical mapping results of a) Au-C-N, b) Au-C-O, c) Au-N-O, and d) C-N-O (left: four steps, middle: six steps, right: eight steps), respectively.

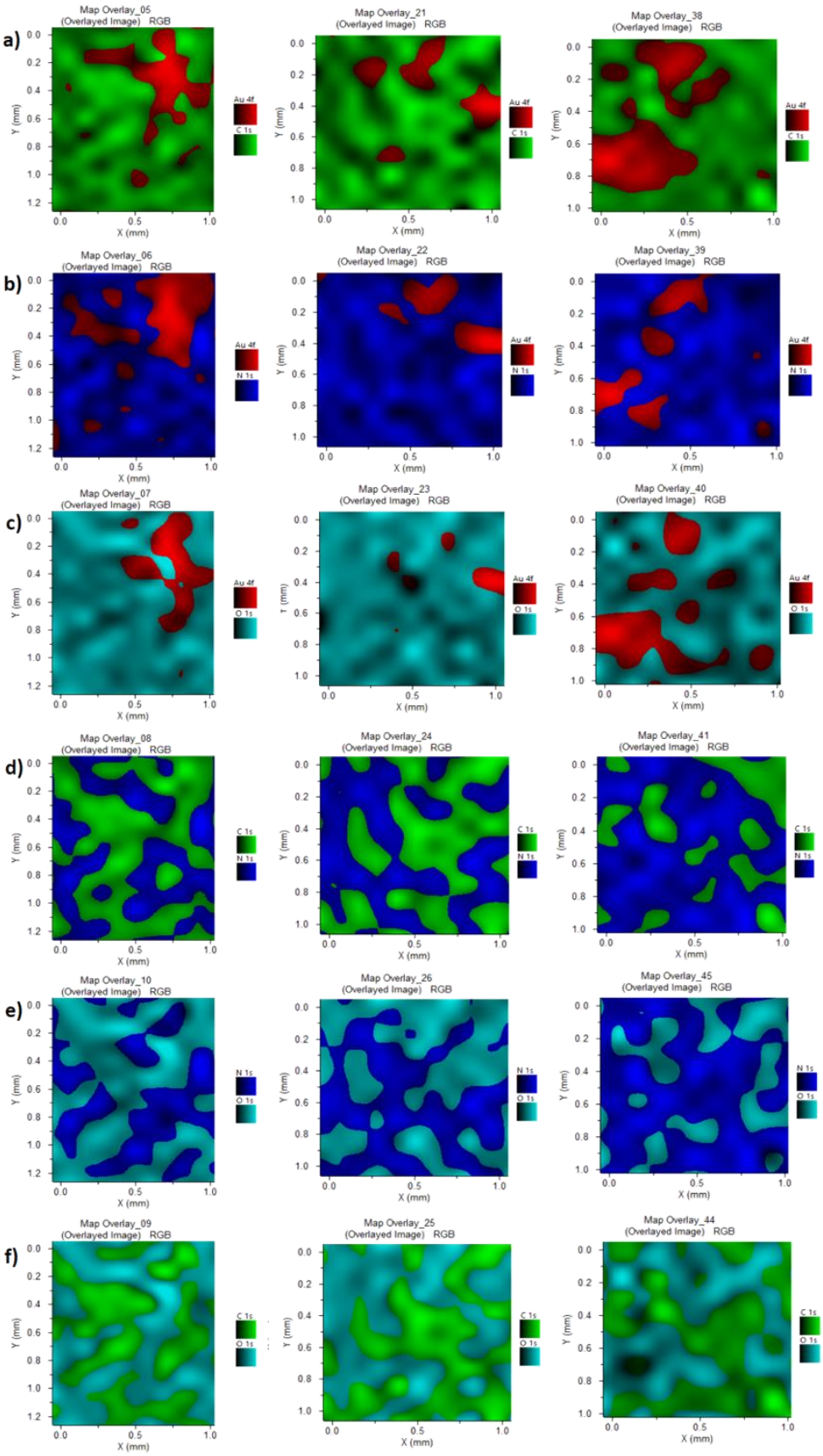

Figure 3.5 XPS binary chemical mapping results of a) Au-C, b) Au-N, c) Au-O, d) C-N, e) N-O, and f) C-O (left: four steps, middle: six steps, right: eight steps).

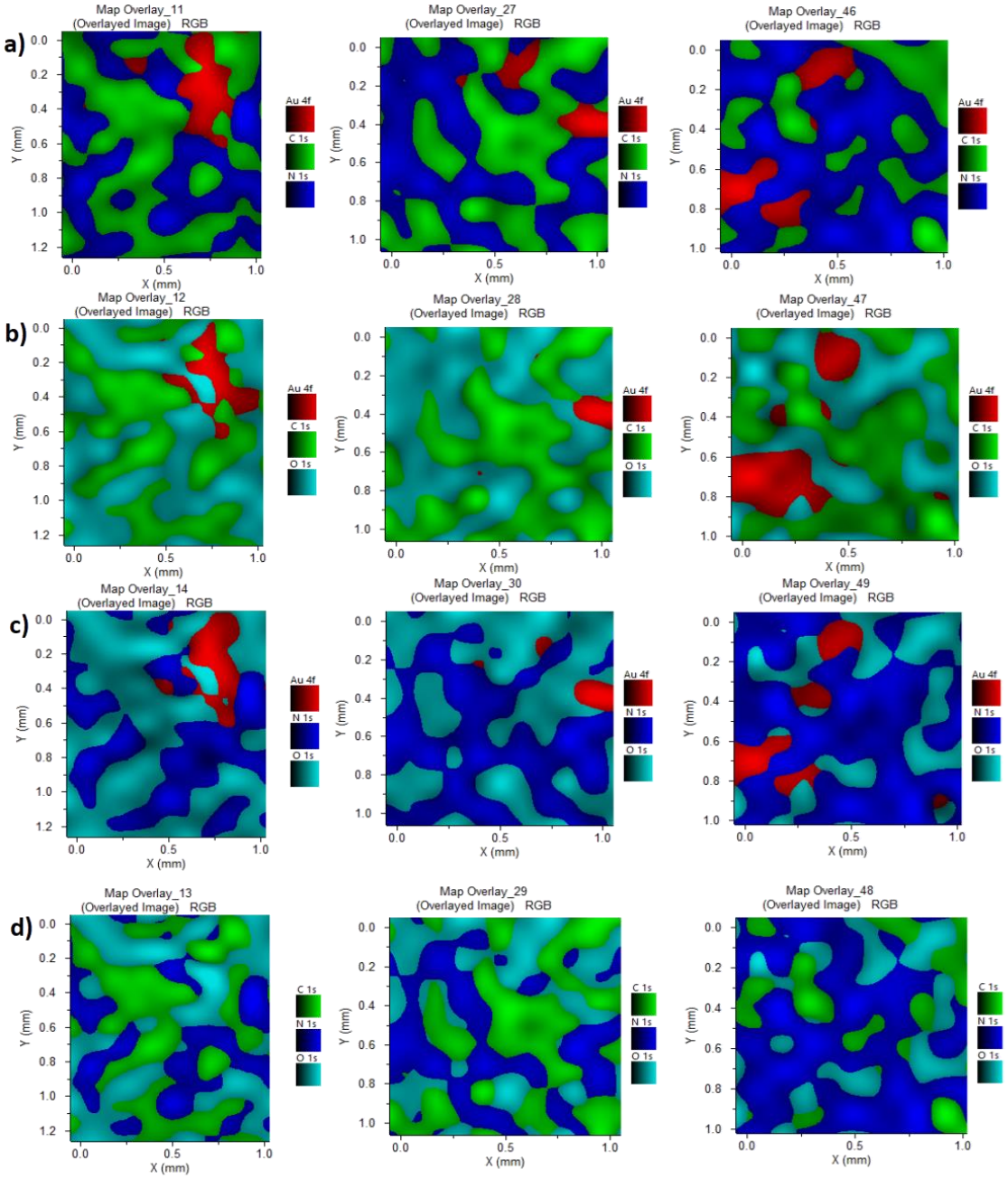

Figure 3.6 XPS tertiary chemical mapping results of a) Au-C-N, b) Au-C-O, c) Au-N-O, and d) C-N-O (left: four steps, middle: six steps, right: eight steps).

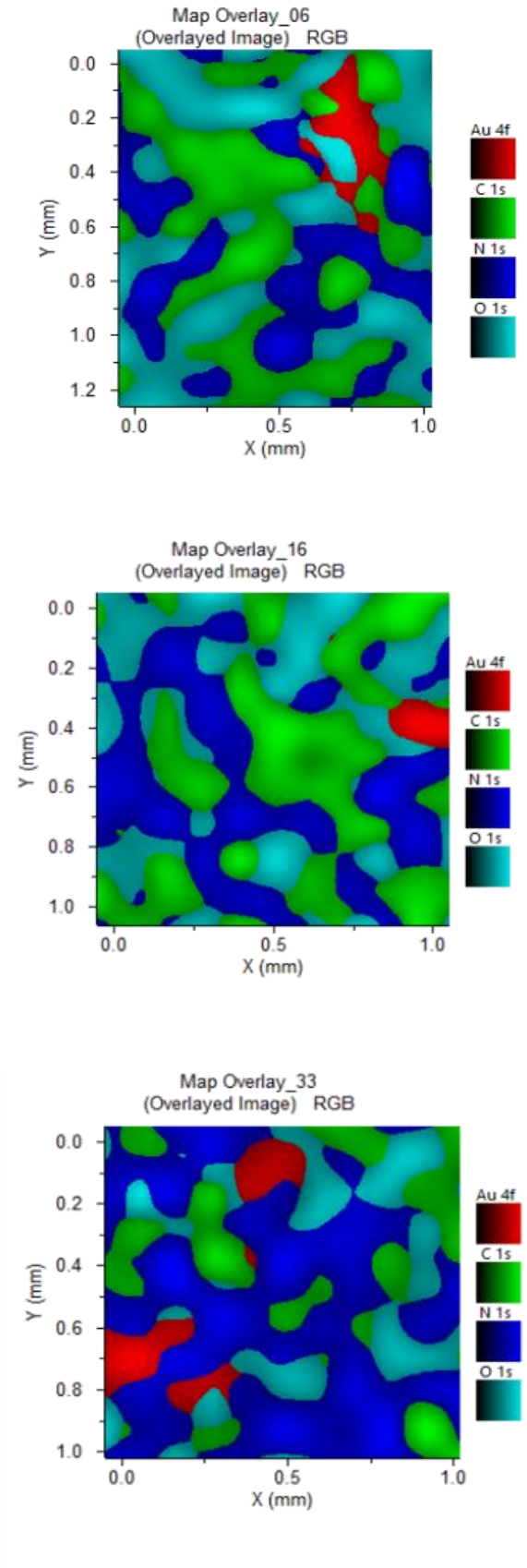

Figure 3.7 XPS quaternary chemical mapping results of a) Au-C-N-O (left: four steps, middle: six steps, right: eight steps).

Figure 3.7 depicts XPS quaternary chemical mapping results of Au-C-N-O with respect to chemical abundance of binding energy of carbon, oxygen, nitrogen and gold. When the presence of Au binding energy is assumed to be related to the PU coating efficiency, the gold chemical abundance rate is 5.5% in four steps, 1.9% in six steps, and 8.9% in eight steps. Figure 3.7 shows that for a high yield PU interface a minimum of six steps should be applied.

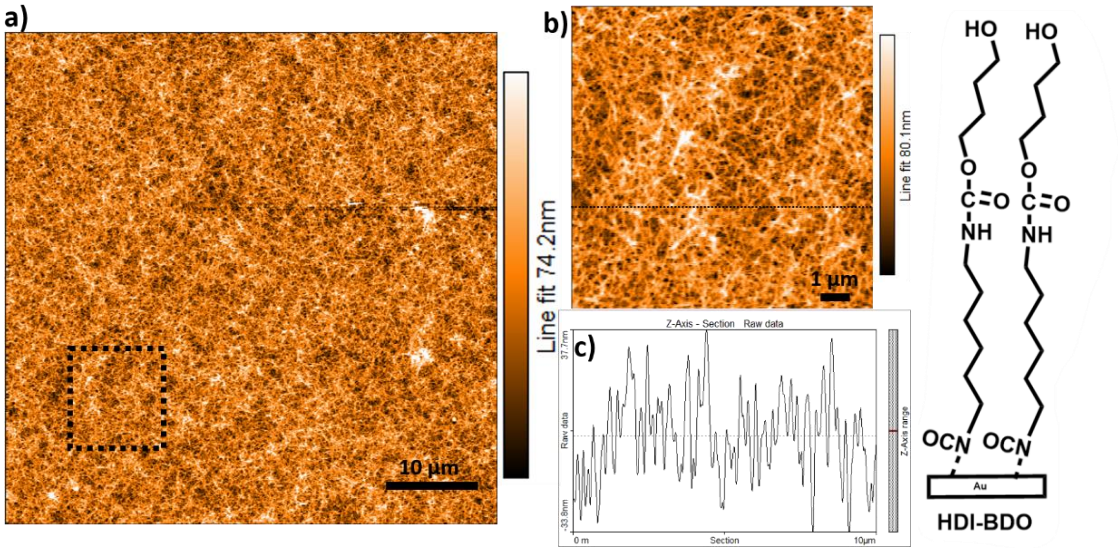

Figure 3.8 a) AFM height image and cross-section of six steps of HDI-1,4-BDO SurfAst urethane polymerization on gold surface. b) AFM height image of a magnified view of Figure 3.8a (black dashed square). c) Cross-section of Figure 3.8b (black dashed line).

Figure 3.8a shows the AFM image of six steps of SurfAst urethane polymerization (3 sequential reactions between 1,4-BDO and HDI) on the gold surface. In Figure 3.8b, the PU interface is found to be various height values between 5 and 30 nm that have to correspond to a roughness of 63 nm. Since the AFM image of the bare gold surface has a 5 nm area roughness, these results demonstrate that the thin polyurethane (PU) interface provides a porous structure on the gold surface which increases the roughness of the surface. Consequently, the thin polyurethane (PU) yielded on the gold surface by using SurfAst urethane polymerization. These results show that the gold substrate has a fully covered and rougher surface after the SurfAst urethane polymerization.

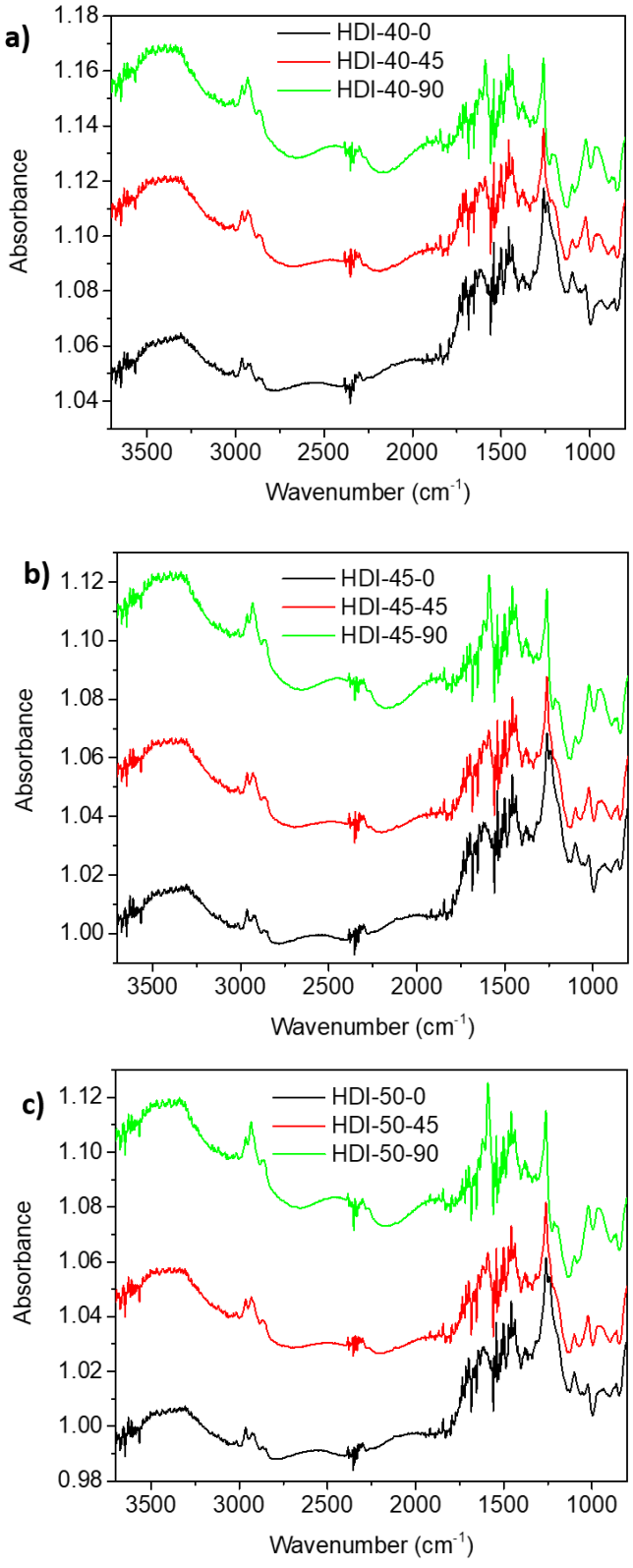

Figure 3.9 FTIR spectrum of six steps of HDI-1,4-BDO SurfAst urethane polymerization on gold surface with a) 40° VeeMAX III angle and 0° 45° 90° Zn-Se p-polarizer. b) 45° VeeMAX III angle and 0° 45° 90° Zn-Se p-polarizer. c) 50° VeeMAX III angle and 0° 45° 90° Zn-Se p-polarizer.

For general information, the maximum throughput of the VeeMAX III occurs at a set angle of incidence of about 45° to 50° and declines to less than 15% throughput at extreme set angles of 30° and 80°. The theoretical beam dimensions at higher angles of incidence become increasingly elliptical in shape. The IR spectra in Figures 3.9 confirms the HDI-1,4-BDO SurfAst urethane polymerization on the gold surface. In particular, signals of the carbamate (urethane) group formed by the reaction of hydroxyl with isocyanate groups appear at 1716 cm^{-1}. The signal at 1020 cm^{-1} is attributed to a C-O stretch. The 1250 and 1542 cm^{-1} amide III, C-N stretching (and N-H bending of amide bond) and amide II, bending vibration of N-H groups (and stretching vibrations of C-N), respectively. Two peaks at 2850 cm^{-1} and 2919 cm^{-1}, which are attributed to the symmetric and asymmetric stretching modes of CH_2 groups, respectively, can be used as references for well-ordered alkyl chains in SAMs.[30, 76] For the ZnSe p-polarizer, when the polarizer is set to 0°, the grid lines run parallel to the width of the polarizer mount, and the transmitted IR radiation will be perpendicular to this. When the polarizer is set to 90°, the grid lines run parallel to the length of the polarizer mount, and the transmitted IR radiation will be perpendicular to this. Thus, the N-H bending vibration peak appears at 1589 cm^{-1} when the polarization degree is 90, while it is absent at 0°. On the other hand, well-defined symmetric and asymmetric stretching modes of CH_2 groups were obtained at a 90° p-polarizer angle from 40°, 45°, and 50° VeeMax III measurements (Figure 3.10). In conclusion, the results show a PU orientation of approximately 90° with respect to the surface and carbon chain packing as the self-assembled monolayers.

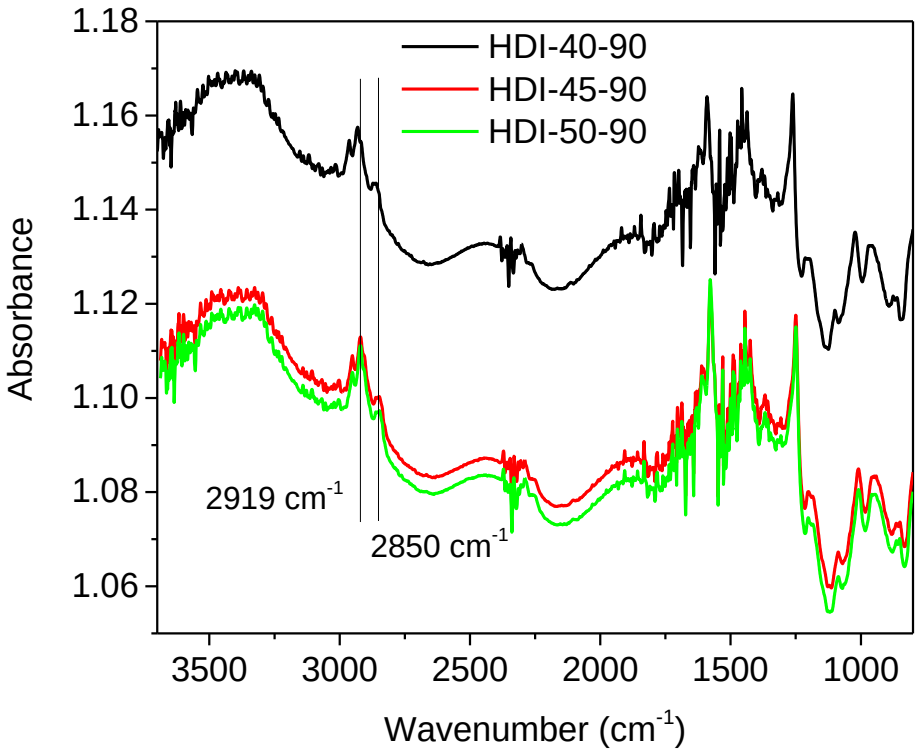

Figure 3.10 FTIR spectrum of six steps of HDI-1,4-BDO SurfAst urethane polymerization on the gold surface with 40°, 45°, and 50° VeeMax III angles and a 90° Zn-Se p-polarizer degree.

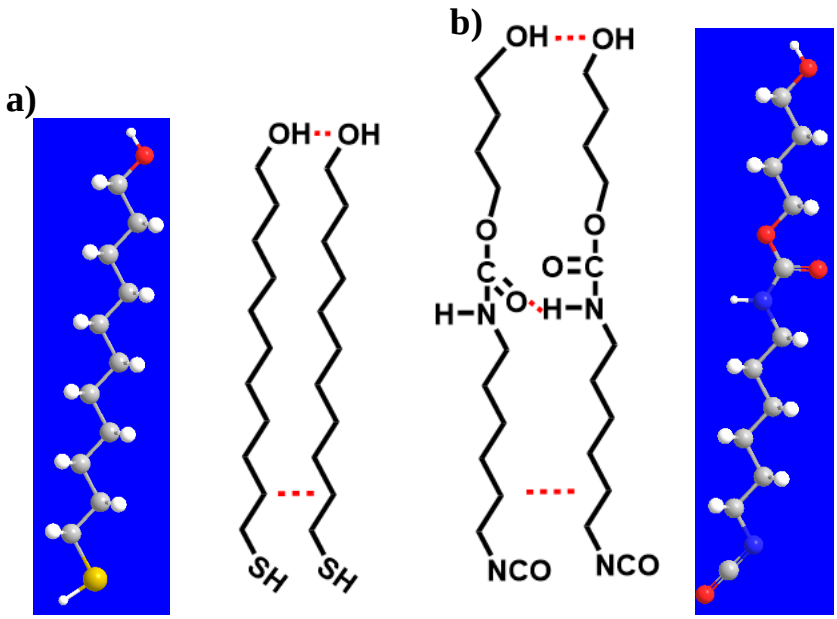

Figure 3.11 Chemical representation of a) 11-mercapto-1-undecanol and b) Two steps SurfAst urethane polymerization.

In another aspect, the chemical representation of the 11-mercapto-1-undecanol yielding a stable SAM structure, and two steps SurfAst urethane polymerization is given in Figure 3.11. The stretched molecule length of the 11-mercapto-1-undecanol and two steps (HDI-1,4-BDO) SurfAst urethane polymerization is nearly 2 nm.[41] By a basic calculation, the ideal secondary interaction value of the between 11-mercapto-1-undecanol molecules that contain eleven -CH_2 (London Dispersion 0.05 kj/mol) and one -OH (Hydrogen bond 10 kj/mol) is about 10.55 kj/mol (Figure 3.11a). On the other hand, the ideal secondary interaction value of the two steps SurfAst urethane polymerization that contains ten -CH_2 (London Dispersion 0.05 kj/mol) and one -OH, one urethane bond (Hydrogen bond 10 kj/mol) is about 20.5 kj/mol (Figure 3.11b). Therefore, it can be assumed that the SurfAst urethane reaction could be twofold as strong in terms of secondary interaction energy per unit length on the surface. This may explain that the PU orientation of approximately 90° with respect to the surface and SAM-like well-ordered structures on the surface.

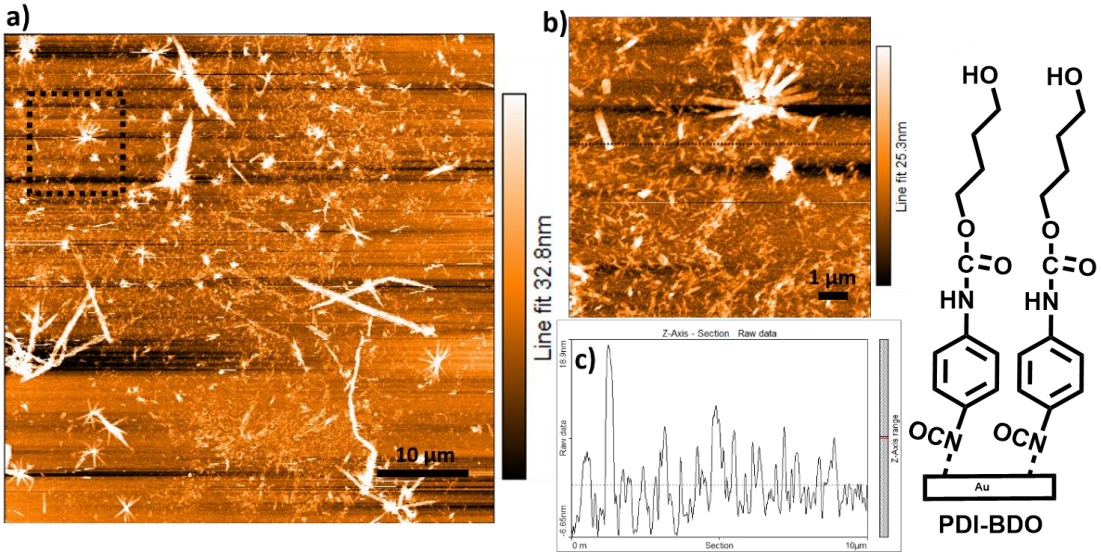

Figure 3.12 a) AFM height image and cross-section of six steps of PDI-1,4-BDO SurfAst urethane polymerization on the gold surface. b) AFM height image of a magnified view of Figure 3.12a (black dashed square). c) Cross-section of Figure 3.12b (black dashed line).

Figure 3.12a shows the AFM image of six steps of SurfAst urethane polymerization (3 sequential reactions between 1,4-BDO and PDI) on the gold surface. The AFM image shows that short and long rod-like structures are formed on the gold

surface. In Figure 3.12b, the rod-like structures may result from the dense urethane bond (hard segment) formed as a result of the reaction between the rigid PDI and the low molecular mass hydroxyl source (1,4-BDO). However, the rod-like structures were not covered homogeneously and continuously on the gold surface as in Figures 3.8a and b (1,4-BDO and HDI). This result may be due to the low yield of the interaction of the PDI with the gold surface as compared to the high yield of linear HDI. Figure 3.12c shows that the short rod-like structures have an identical average height distribution while the long rod-like structures are about three times higher. Since the SurfAst urethane polymerization on the gold surface was not homogeneous, the incubation concentration was increased twofold (concentrated PDI-1,4-BDO) to enhance PDI gold interaction.

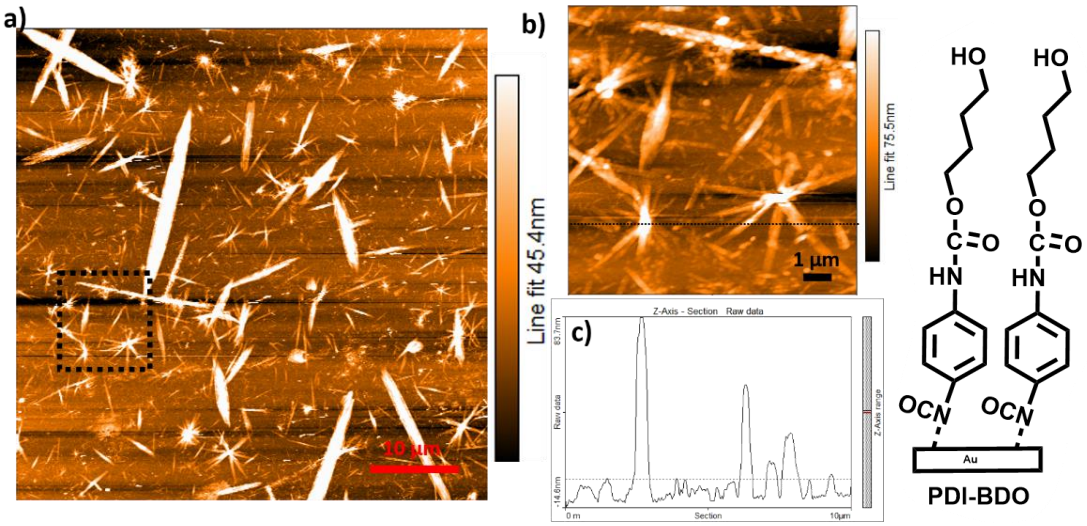

Figure 3.13 a) AFM height image and cross-section of six steps of concentrated PDI-1,4-BDO SurfAst urethane polymerization on the gold surface. b) AFM height image of a magnified view of Figure 3.13a (black dashed square). c) Cross-section of Figure 3.13b (black dashed line).

Figure 3.13a shows the AFM image of six steps of concentrated PDI-1,4-BDO SurfAst urethane polymerization (3 sequential reactions between 1,4-BDO and PDI) on the gold surface. The AFM image shows that extended rod-like structures are formed on the gold surface as compared to Figure 3.13a. An increased PDI and 1,4-BDO concentration could be formed due to an increased number of rigid segments on the gold surface, resulting in the extension of rod-like structures. Figure 3.13c shows that the center of the rod-like structures has a twofold higher average height distribution than the short rod-like structures.

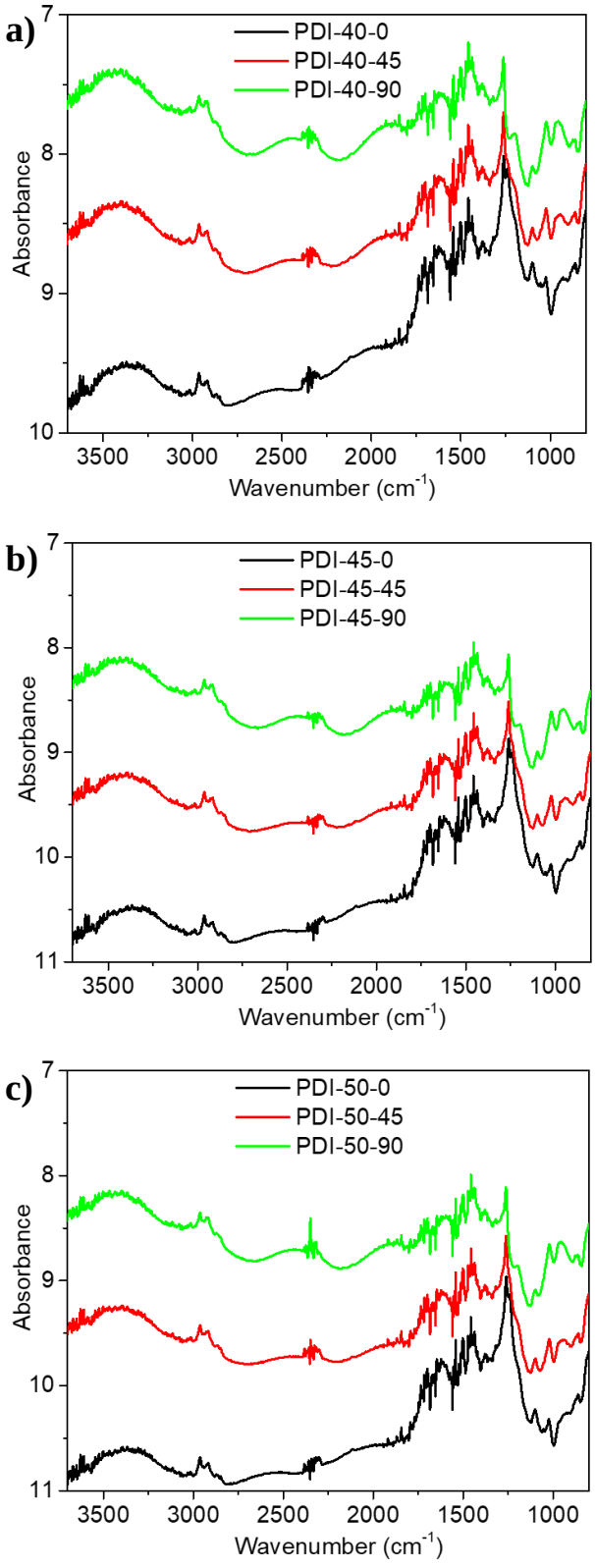

Figure 3.14 FTIR spectrum of six steps of concentrated PDI-1,4-BDO SurfAst urethane polymerization on the gold surface with a) 40° VeeMAX III angle and 0° 45° 90° Zn-Se p-polarizer. b) 45° VeeMAX III angle and 0° 45° 90° Zn-Se p-polarizer. c) 50° VeeMAX III angle and 0° 45° 90° Zn-Se p-polarizer.

The IR spectra in Figure 3.14 confirm the six steps of concentrated PDI-1,4-BDO SurfAst urethane polymerization on the gold surface. In particular, signals of the carbamate (urethane) group formed by the reaction of hydroxyl with isocyanate groups appear at 1715 cm^{-1}. The signal at 1020 cm^{-1} is attributed to a C-O stretch. The 1250 and 1542 cm^{-1} amide III, C-N stretching (and N-H bending of amide bond) and amide II, bending vibration of N-H groups (and stretching vibrations of C-N), respectively. Two peaks at 2850 cm^{-1} and 2919 cm^{-1}, which are attributed to the symmetric and asymmetric stretching modes of the CH_2 groups, respectively, can be used as references for well-ordered alkyl chains in SAMs.[30, 76] Symmetric and asymmetric stretching modes of CH_2 groups were found to be identical at all angles (0°, 45°, and 90° p-polarizer) by using VeeMax III measurements. In conclusion, the results show the PU orientation of all directions with respect to the surface and do not show self-assembly-like properties.

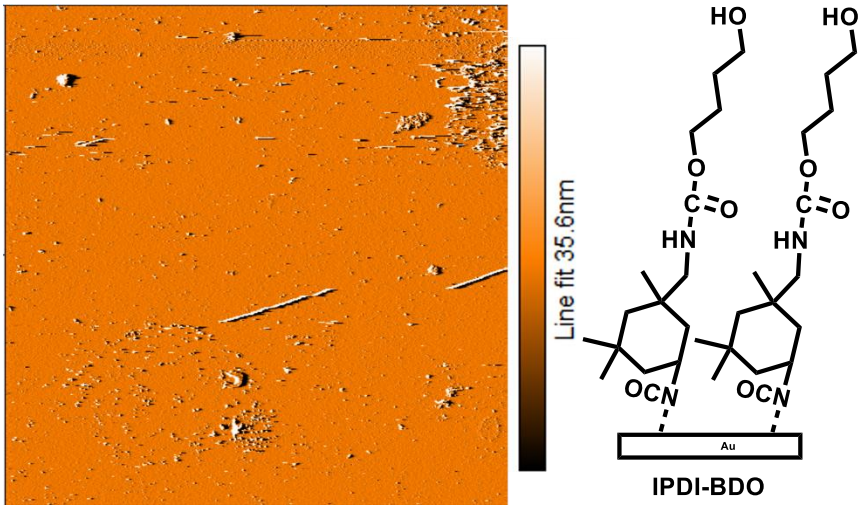

Figure 3.15 AFM height image of six steps of IPDI-1,4-BDO SurfAst urethane polymerization on the gold surface.

Figure 3.15a shows the AFM image of six steps of SurfAst urethane polymerization (3 sequential reactions between IPDI-1,4-BDO) on the gold surface. The AFM image indicates that there are no reactions between IPDI-1,4-BDO; therefore, the PU interface did not form on the gold surface. The reaction may not have happened on the gold surface since -NCO functional groups have low reactivity due to their cycloaliphatic structure of IPDI. As such, IPDI is used in waterborne PU production due to its low reactivity.[77]

3.2.1. Passivating with 11-Mercapto-1-Undecanol of the Gold Surface

Figure 3.16 shows the AFM image of the 11-mercapto-1-undecanol passivated gold surface and its cross-section and the microscope image of the passivated gold surface. The gold surface was passivated with 11-mercapto-1-undecanol to find out the average height distribution of the nanoporous structure formed after SurfAst urethane polymerization. Figure 3.16a shows the AFM image of 11 mercapto-1-undecanol molecules with a sharp square pattern before SurfAst urethane polymerization reactions. The average height is approximately 2.5 nm, indicating that the resulting 11-mercapto-1-undecanol structure is perfectly packaged to prevent the interaction of the diisocyanate with the gold surface (Figure 3.16b). Also, Figure 3.16c shows a microscope image of the gold surface that is passivated with 11-mercapto-1-undecanol.

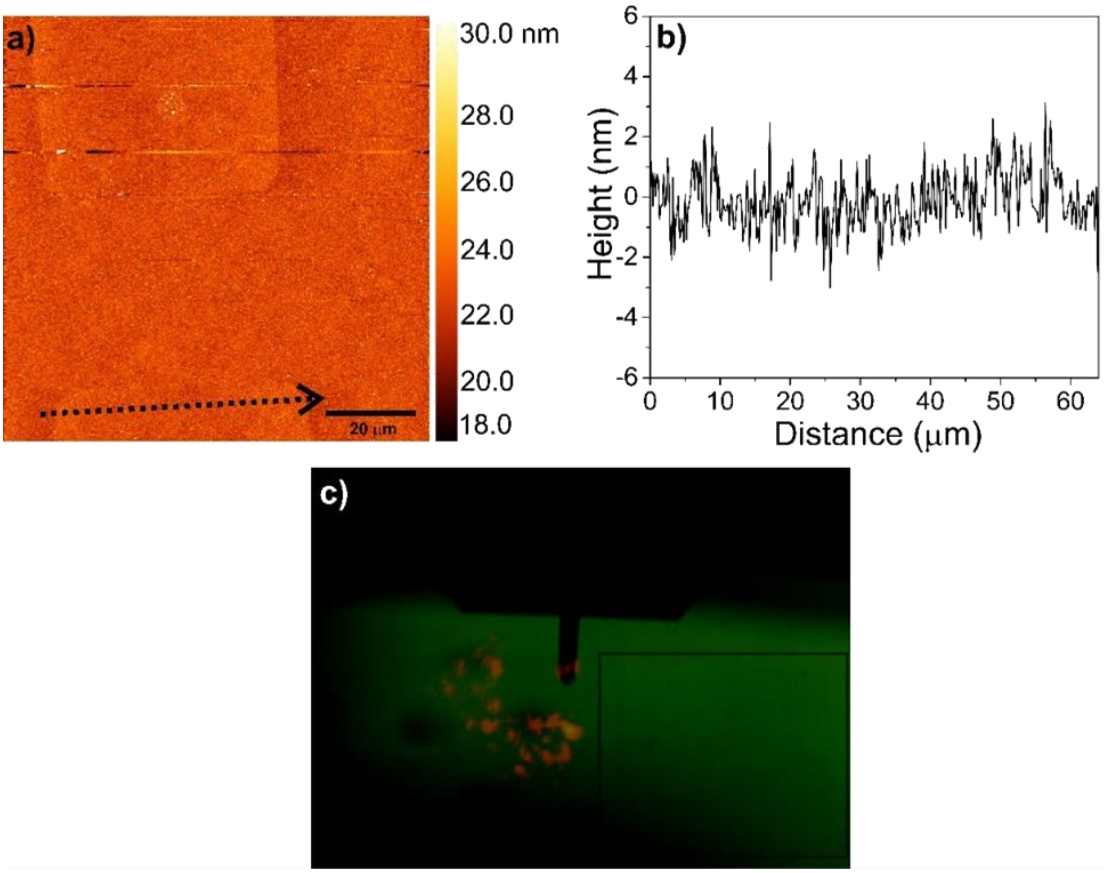

Figure 3.16. a) AFM image of 11-mercapto-1-undecanol passivated gold surface. b) Cross-section (black dashed line) of Figure A. c) Microscope image of the 11-mercapto-1-undecanol passivated gold surface.

3.2.2. Surface Assisted Urethane (SurfAst) Polymerization

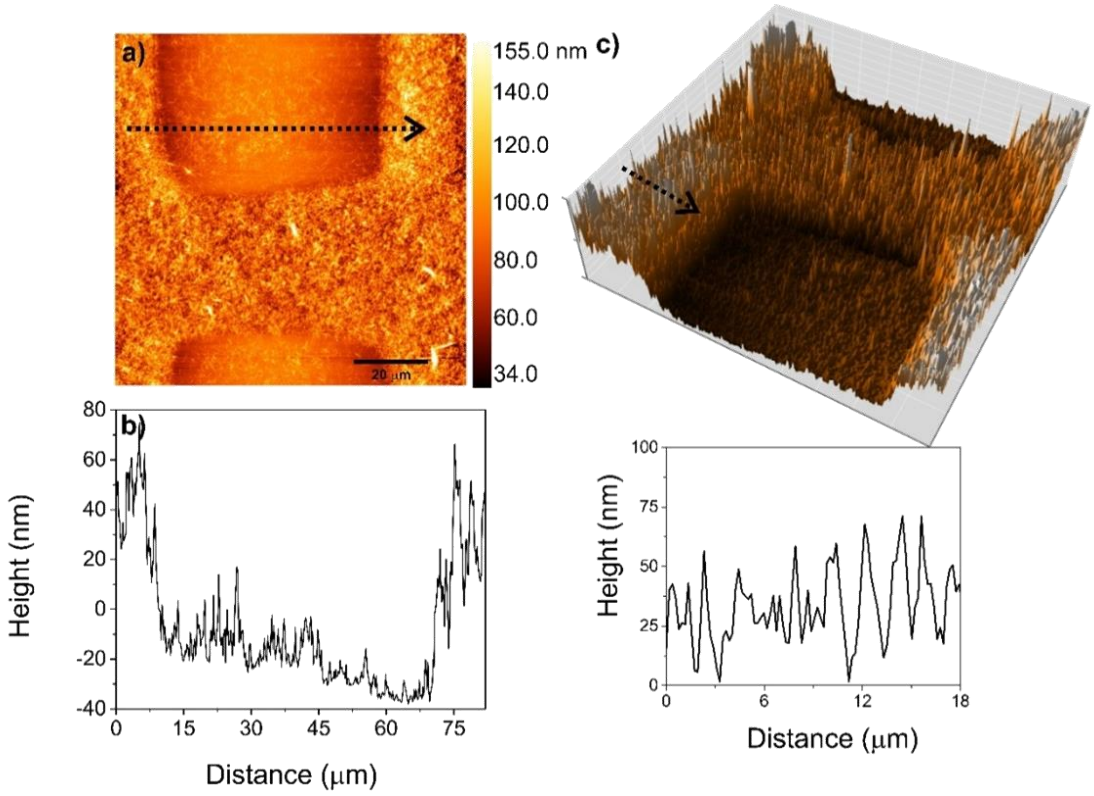

Figure 3.17. a) AFM image of the gold surface after eight-step SurfAst urethane polymerization. b) Cross-section (black dashed line) of Figure 3.17a. c) 3D chart view of Figure 3.17a and cross-section (black dashed arrow).

Figure 3.17a shows the AFM image after eight-step SurfAst urethane polymerization (HDI and 1,4-BDO, respectively) reactions on the gold surface. The PU interface has formed a sharp edge homogeneously on a non-passivated gold area. The average height distribution of the nanoporous PU structure is approximately 70 nm, indicating the resulting high yield PU reaction on the gold interface. Considering that there is one reaction between BDO and HDI on the gold surface in each step as a result of the four sequential (eight-step) reactions of SurfAst urethane polymerization, the coating height should be about 9 nm. However, the AFM cross-section analysis shows a profile height of more than 9 nm (height profile presented in Figure 3.17b), indicating that more than four reactions occurred between BDO and HDI at the gold surface. The reason for this phenomenon is that the HDI and BDO monomers could be transported between the incubation mediums via non-specific adsorption on the gold surface despite rinsing with acetone every step. Thus, the urethane bond can be formed on the surface as

well as in the liquid phase and be subsequently bound to the gold surface or remain in the liquid medium. The most obvious proof is the observation of cloudy polymeric structures in the acetone during the isocyanate incubation (fifth step) of the SurfAst urethane polymerization. The formation of this cloudy polymeric structure can be explained by the supersaturation surface that was formed by the accumulation of monomers adsorbed to the surface in previous steps due to the rapid urethane polymerization. As seen in the 3D map in Figure 3.17c, hydrogen-bonding between urethane groups and the Van der Waals interactions between the CH_2 groups of HDI and BDO jointly provide interchain interactions and create a nanoporous structure with a certain chain propagation angle on the gold surface (see FTIR section).

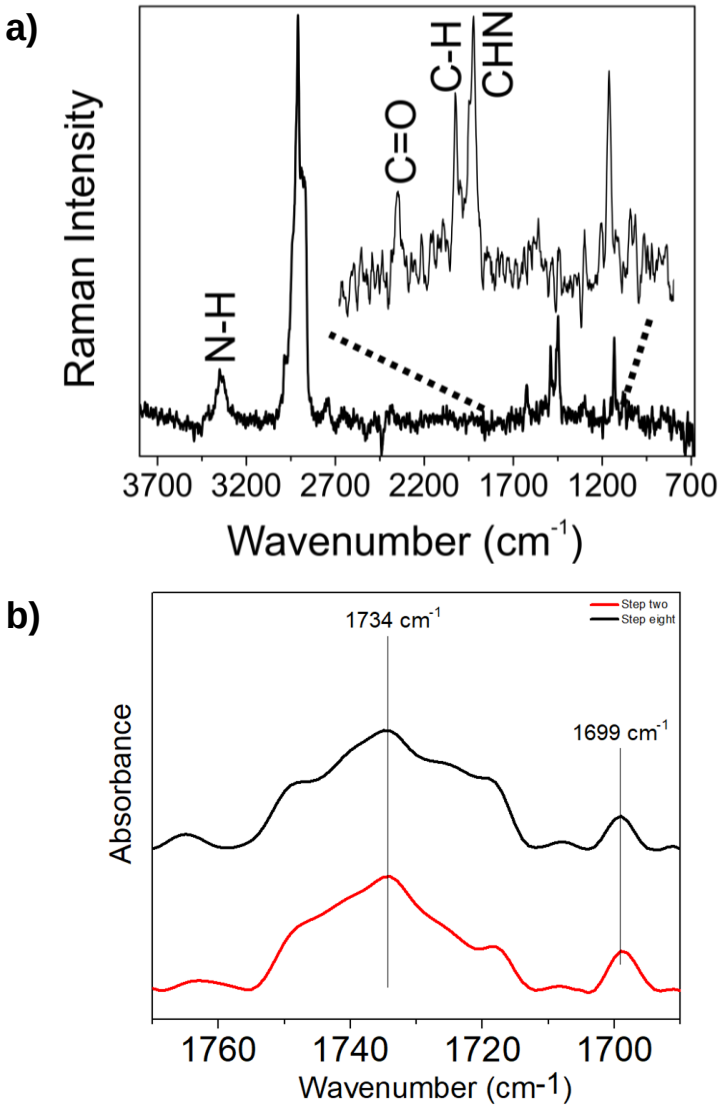

Figure 3.18. a) Raman spectrum of the PU interface inset: magnified view of the fingerprint region. b) FTIR spectrum of step two and eight.

A functional group analysis of the PU interface was performed with Raman spectroscopy and Fourier transform infrared (FTIR) spectroscopy. The Raman spectra of the PU interface is shown in Figure 3.18a. Figure 3.18a shows asymmetric aliphatic C−H stretching at 2907 cm^{-1}, symmetric stretching at 2873 cm^{-1}, C−H bending vibration band at 1445 cm^{-1}, and CHN group vibration at 1490 cm^{-1}. Hydrogen bond-associated secondary urethane (−HN−CO−O−) N−H stretching was found at ca. 3330 cm^{-1} and secondary amide C=O stretching (solid phase) at ca. 1625 cm^{-1}. The peak observed at 1130 cm^{-1} was assigned to urethane-attached C - H deformation.[76, 78] The Raman spectrum confirms that the nanoporous structure is made of urethane bonds. Kojio et al.[79] investigated the FTIR peaks of PU films. The results show that the hydrogen-bonded carbonyl stretching band and free one exhibit two characteristic peaks at 1704 and 1730 cm^{-1}, respectively. As shown in Figure 3.18b, two characteristic peaks at 1734 and 1699 cm^{-1} were obtained as a result of the FTIR characterization of the PU interface. Since peak densities at 1699 cm^{-1} decrease slightly as the number of steps increases, it can be assumed that the hydrogen-bonded carbonyl stretching decreases marginally. In addition, five absorption bands are seen at approximately 1740 and 1730 cm^{-1} for free carbonyls and 1725, 1713, and 1702 cm^{-1} for hydrogen-bonded carbonyls.[80, 81] The remaining three peaks were assigned at 1708 and 1718 cm^{-1} for hydrogen-bonded carbonyl and 1750 cm^{-1} for free carbonyl. Hydrogen bonds between hard segments can be interpreted as NH···O−C at 1708 cm^{-1} and binary NH···O−C at 1718 cm^{-1}. FTIR spectroscopy results show that there are at least three types of hydrogen bonds at the PU interface (Figure 3.19).

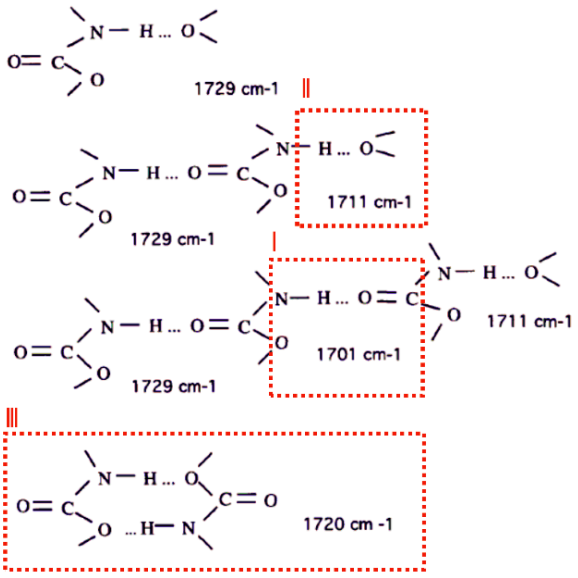

Figure 3.19. Wavenumbers of the hydrogen bond types.[81]

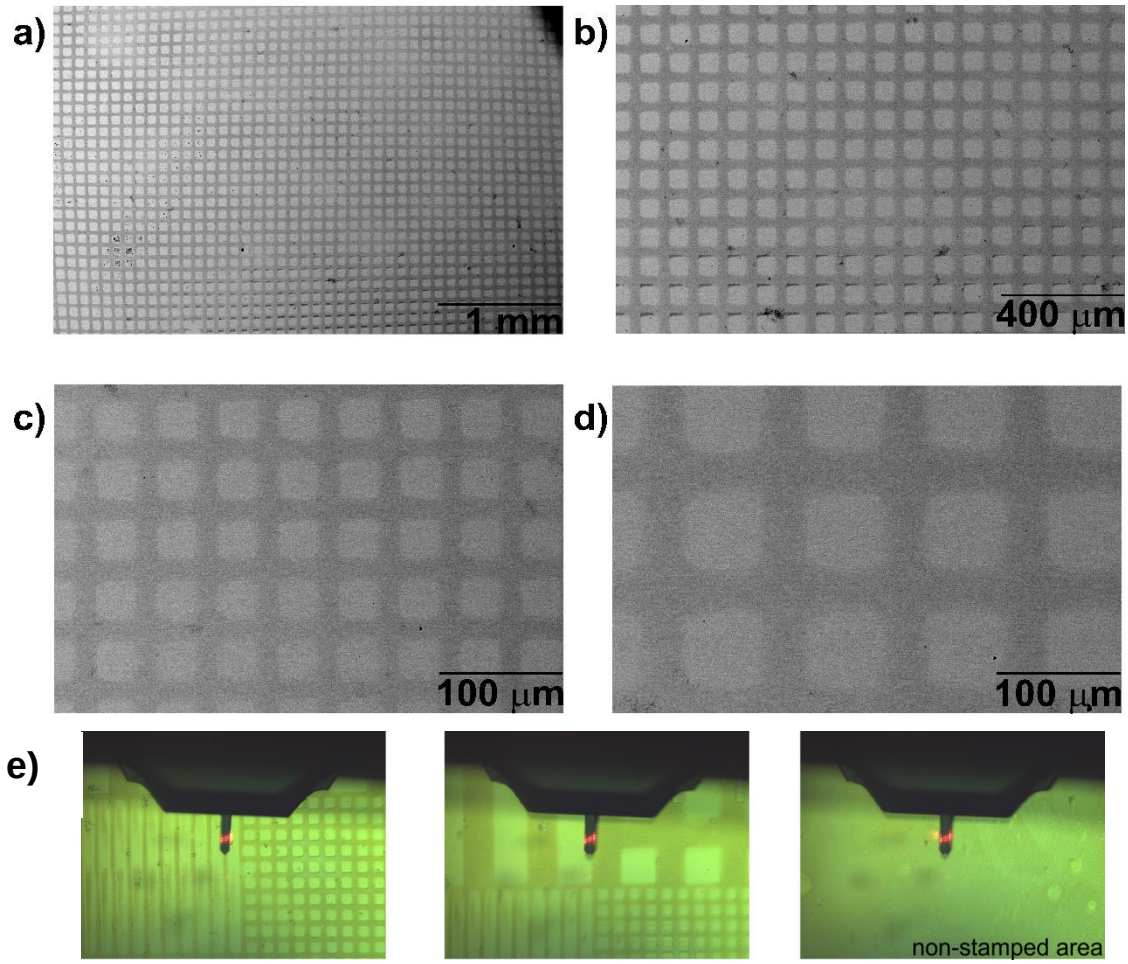

Figure 3.20. SEM images after SurfAst urethane polymerization. a) 100x, b) 250x, c) 500x, and d) 1000x. e) Light microscope image after SurfAst polymerization.

Figure 3.20 shows the scanning electron microscopy SEM images after SurfAst urethane polymerization. Figure 3.20a demonstrates approximately 6 mm^2 areas, indicating that SurfAst urethane polymerization can be applied uniformly over a large area. Increasing the scanning electron microscope (SEM) magnification of the gold surface, the image (Figure 3.20b, c, and d) reveals that the nanoporous structure has sharp edges and is homogeneously distributed. Also, these SEM results confirm the AFM results. Furthermore, the light microscope images shown in Figure 3.20e are similar to the SEM images and indicate that the large-area interface with nanopore is readily achieved by SurfAst polymerization.

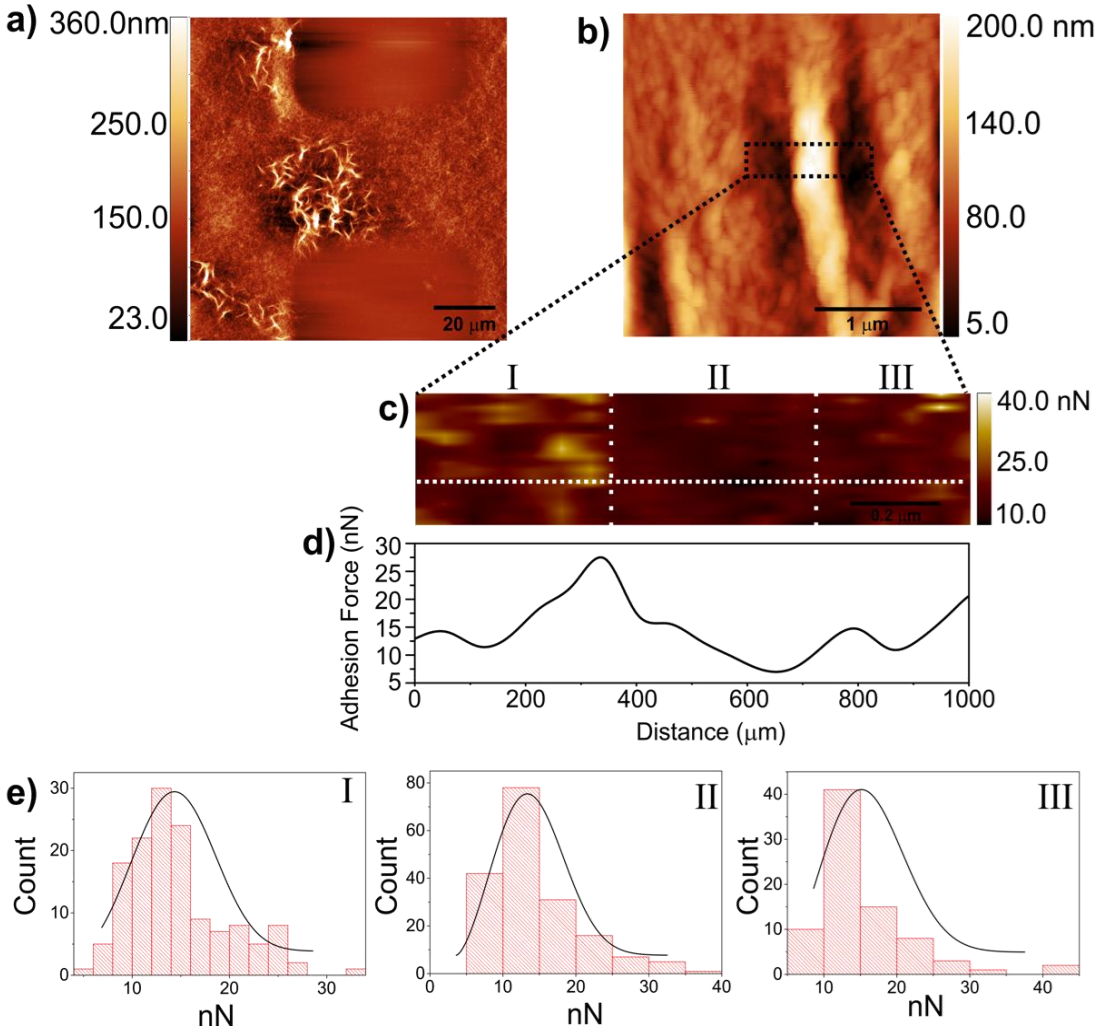

Figure 3.21. a, b) AFM images of nanoporous and rod-like structures after SurfAst polymerization. c) Adhesion force mapping both nanoporous and rod-like structures (rectangular black dashed). d) Adhesive force profile (horizontal white dashed line). e) The distribution of area I (left), II (middle), and III (right) adhesive force.[41]

As seen in Figures 3.21a and b, the AFM characterization sharply shows that there are two types of nanoporous and rod-like structures on the gold surface. The nanoporous structure may be formed by a small number of polyurethane bundles, and the rod-like structures could occur via parallel stacking of more polyurethane bundles through hydrogen bonding between urethane groups.[82] The frequent observation of rod-like structures in the AFM image is due to a linear molecular structure of HDI and 1,4-BDO. Besides, Mishra et al.[83] reported that polyurethane containing linear isocyanate exhibits micro-cluster structures consisting of parallel stacking of urethane groups. In addition,

Yılgör et al. reported that the symmetry of urethane monomers (HDI / 1,4-BDO) contributes to the strong interaction of repeated urethane groups and increases hydrogen bond strength. In conclusion, we assume that the symmetry of the monomers of HDI and 1,4-BDO used in the study contributes to the formation of rod-like areas on the gold surface.[84, 85] Figure 3.21c is the adhesion force mapping of the rectangular black dashed region in Figure 3.21b containing both nanoporous and rod-like structures. In order to understand the eligibility of the two types of structures at the gold interface for antifouling application, adherence force measurements were made. Thus, the adhesion behavior of the two types of formations at the PU interface can be compared with the nN values. As seen in the adhesion force mapping Figure 3.21c, the rod-like structure results in a darker color while the left and the right areas are lighter and correspond to the nanoporous section. This slight color difference may be due to the high interaction of the nanoporous structure with the AFM tip as it consists of a loose polymer chain bundle. On the contrary, the rod-like structure interacts less with the AFM tip, as it forms a stiff polymer bundle. Figure 3.21d shows the adhesion values corresponding to the dashed white line in the adhesion force mapping. Figure 3.21e shows the distribution of the area of I (left), II (middle), and III (right) adhesive force values. As a result of the distribution of adhesion force, the values of the rod-like and nanoporous structures are 13.30 nN and 14.36 nN, respectively. This result proves that the PU interface shows a uniform structure with a slight difference in adhesion values.

Figure 3.22 shows the XPS point analysis results and chemical mapping image of the PU interface after SurfAst polymerization. Figures 3.22a, b, and c demonstrate the XPS spectra of C 1s, N 1s, and O 1s, respectively. In Figure 3.22a, the C 1s spectrum has deconvoluted into four peaks. The peak at 284.8 eV corresponds to **C**-C aliphatic carbons, and a minor peak at 283.5 eV is present. The binding energy of ether carbon **C**-O(C=O) and N-(**C**=O)-O carbamate groups are assigned to 286.0 eV and 288.35 eV. In the N 1s spectrum, a sharp peak located at 399.4 eV can be attributed to (O=C)-**N** groups (Figure 3.22b). The O 1s spectrum has one broad peak at 531.4 eV corresponding to group C-(C=**O**)-O. Also, it can be assumed that peak broadening toward higher energy at 532.5 eV may refer to ether oxygen in C-(C=O)-**O** (Figure 3.22c). These results show that the XPS point analysis peaks are broader than the XPS results presented in *Chapter 2*. In addition, the XPS point analysis includes all the characteristic binding energy peaks of polyurethane. Therefore, the results indicate that polymerization has taken place on the gold surface.[86-88]

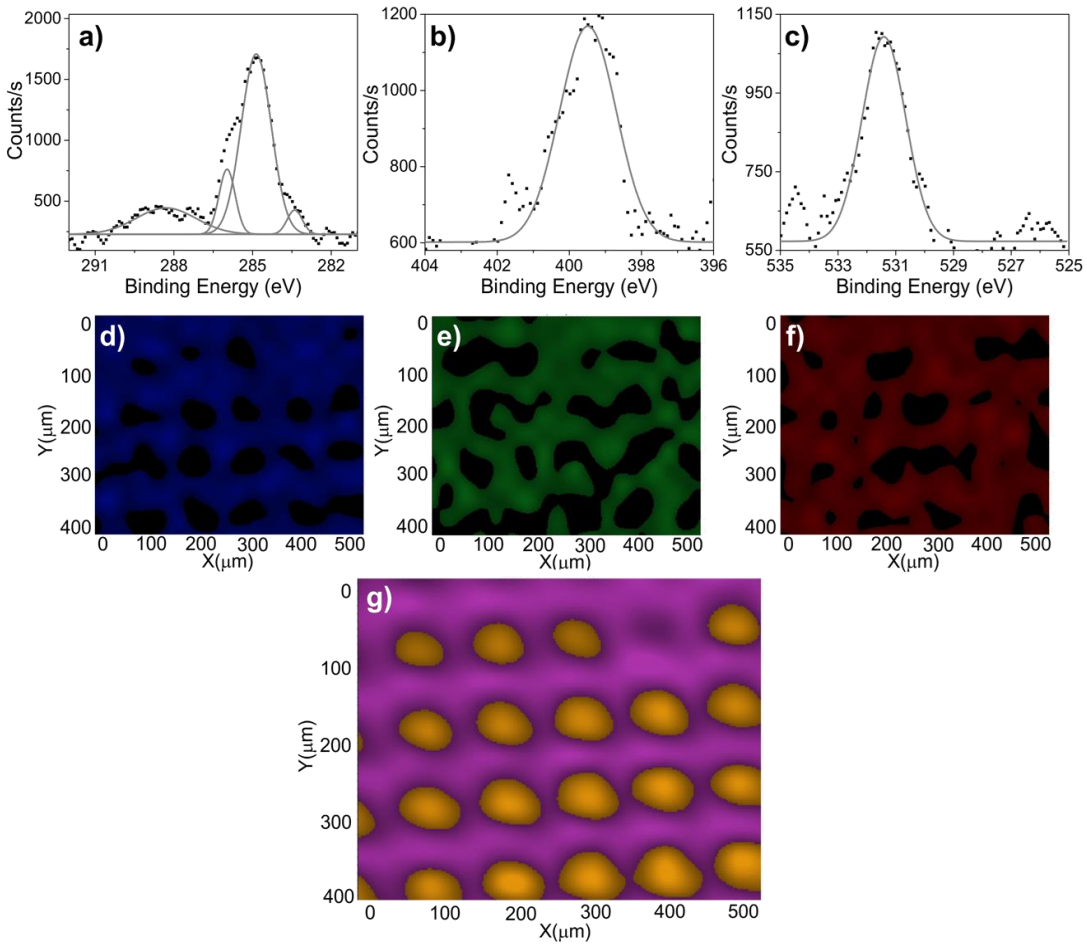

Figure 3.22. XPS spectra of a) C 1s, b) N 1s, and c) O 1s chemical mapping results of d) C 1s, e) N 1s, and f) O 1s after SurfAst polymerization. g) XPS chemical mapping of the PU interface.[41]

XPS chemical mapping (500 × 400 μm) of the PU interface shown in Figures 3.22d, e, and f corresponds to the chemical abundance of carbon, oxygen, and nitrogen on the gold surface, which is shown in blue, green, and red, respectively. Black regions describe the absence of the corresponding binding energy in each representation. C, N, and O images are seen in every region where there is a PU interface on the gold surface. Figure 3.22g shows the XPS chemical mapping representing the sum of the abundance of C, N, and O (purple: PU; yellow: gold surface). The results are consistent with AFM topography mapping and SEM images, and these results prove that the nanoporous structure is PU on the gold surface.

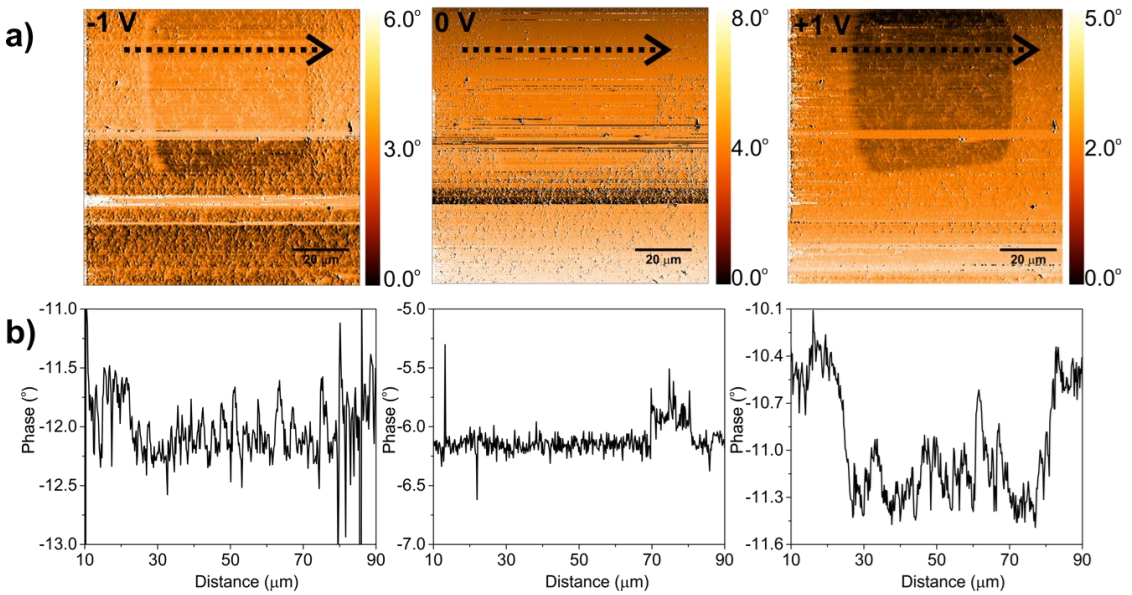

Figure 3.23. a) EFM image after SurfAst polymerization with -1, 0, and +1 V, respectively. b) Phase shift profiles.[41]

Electrostatic force microscopy (EFM) was used to determine long-range interactions and local electrostatic characteristics that play a crucial role in protein adsorption. Therefore, it has simulated the behavior of the interface against charged proteins by realizing the interaction profile of a charged object (AFM tip) on the nanoporous PU. All EFM measurements were carried out in double-pass mode with a 40 nm tip lift, and the EFM image was obtained by applying to the tip 0, +1, and -1 V, respectively (Figure 3.23a). Also, Figure 3.23b indicates the EFM phase shift measurement corresponding to -1 V, 0 V, and +1 V voltages applied to the tip. The Vtip is set to 0 V as a reference measurement, where there is no difference between the gold surface and the polymer. When the Vtip is set to -1 V, it causes a phase shift of 0.49° between the polymer and the gold surface, while a Vtip set to +1 V causes a phase shift of 1.57.° These results show that charged species with +1 V tend to interact more with PU on the gold surface than charged species with -1 V charge.[27]

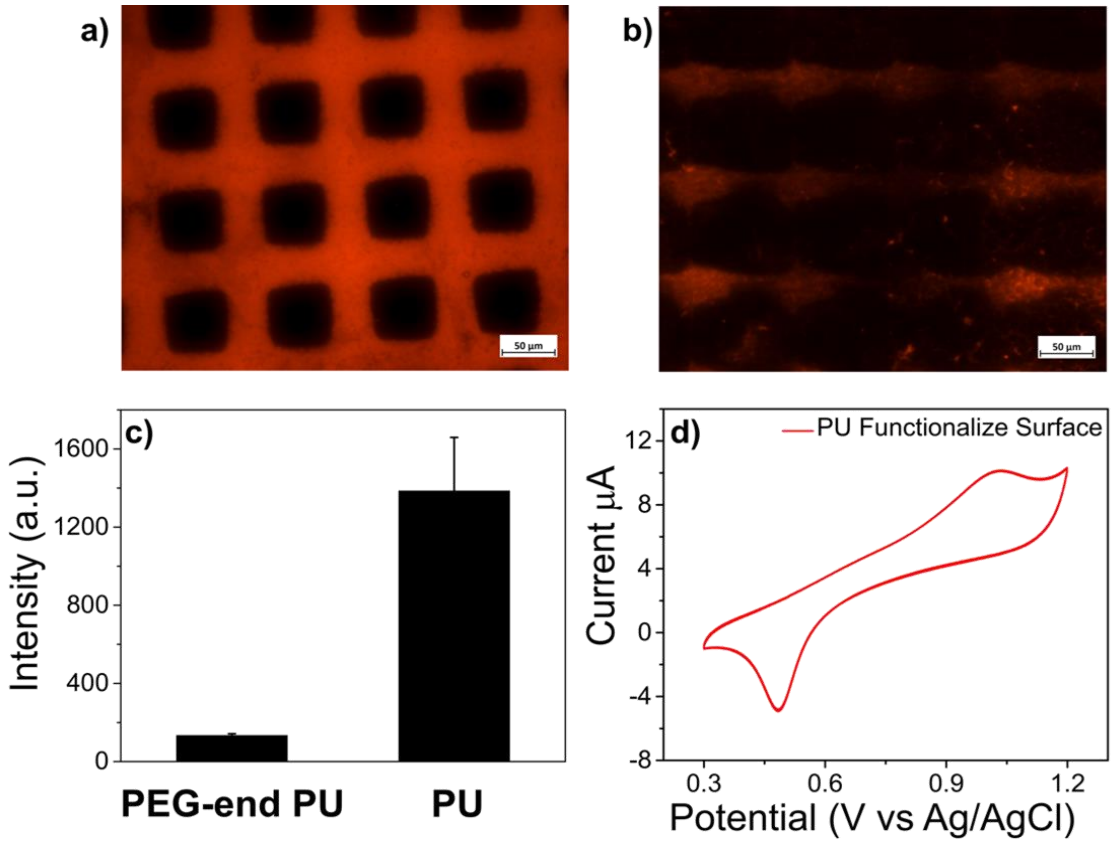

Figure 3.24. a) Fluorescence image of the PU interface after incubation with Texas Red-conjugated bovine serum albumin (BSA-T). b) Fluorescence image of the PEG-end PU-functionalized interface after incubation with BSA-T. c) Fluorescence intensity of PU and PEG-end PU-functionalized interface. d) Cyclic voltammogram of PU-functionalized interface (reference electrode: Ag/AgCl).[41]

It has been proven with the results of XPS and AFM that SurfAst urethane polymerization gives uniform PU consisting of a nanoporous interface that provides a homogeneous surface in large areas. Moreover, the postfunctionalizable nanoporous PU shows that it can be designed as a tailoring interface depending on the application. As proof of the tailoring interface, the -NCO-end PU chain was reacted with polyethylene glycol (PEG 1000) to postfunctionalize at the interface. The hydrophilic polymer chains of PEGs could create hydrogen-bonds with numerous water molecules to produce a hydration layer. Thence, the PEG offers a passive mechanism to enhance the hydrophilicity of the surface and prevent protein adsorption.[89] For instance, poly(dimethylsiloxane) has an interface energy of 52 mJ/m^2 with water while polar polymers such as PEG have less than 5 mJ/m^2. As a result, amphiphilic biomolecules like

proteins exhibit notable adsorption when in contact with a hydrophobic surface to minimize interface energy.[90] Heuberger et al. reported that the conformational area of the PEG chains is modulated in water and that the water content in the PEG-grafted layers is above 80% by volume.[91] Additionally, the flexibility of the polyether backbone nature of a PEG and hydration pressure acting as a barrier creates configurative mobility due to the steric excluded volume effects and blocks potential protein adsorption sites. Therefore, an antifouling surface is obtained since the entropic energy cost to exceed the excluded volume is too high for proteins to adsorb to the surface (Figure 3.26).[67] When the biomolecule approaches a surface that has a flexible polymer chain, the long-chain is compressed to produce elastic repulsion (the mechanism is illustrated in Figure 3.25).[92]

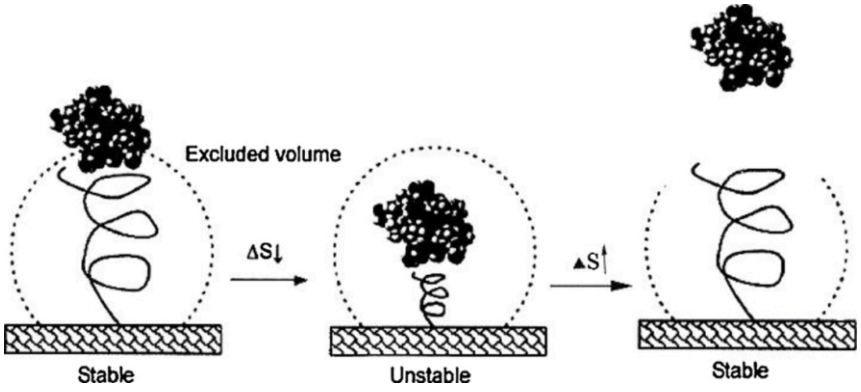

Figure 3.25. Schematic of the steric hindrance theory.[92]

Benhabbour et al. stated that dendronization of PEGylated (generations 1 to 4) surfaces increased surface hydrophilicity, however, also increased protein adsorption. Thus, it has been revealed that PEG chain flexibility is vital in antifouling surface modulation.[93] Additionally, Sharma et al. investigated the longtime endurance of PEG-modified silicone surfaces in the biological environment. They demonstrated that surfaces retained their protein and cell-repellent properties even after immersion for at least four weeks.[94]

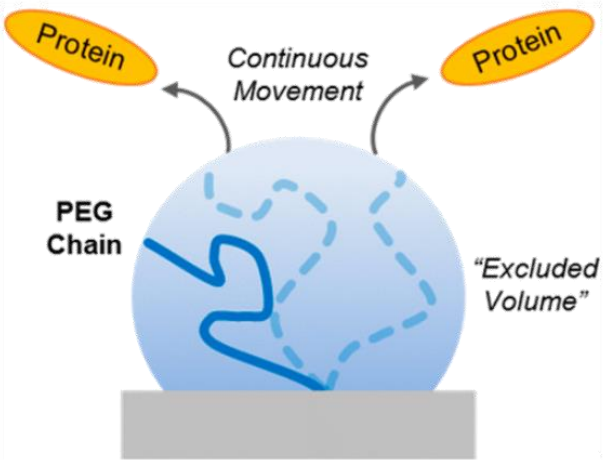

Figure 3.26. Schematic of the steric excluded volume effects.[67]

Figure 3.24a is the fluorescence image of the PU-coated gold surface after incubation with BSA-T. The fluorescence image showed that homogeneous protein adhesion occurred at the PU interface. This result also confirms the adhesion force mapping result (see Figure 3.4). In contrast, after PEG functionalization, a significant drop in the fluorescence intensity of BSA-T has been observed (Figure 3.24b), which proves the efficient functionalization of the PEG layer on PU. A significant decrease in the fluorescence intensity of BSA-T was observed after the PEG functionalization of the PU interface, as seen in Figure 3.24b. Figure 3.24c shows that the fluorescence intensity was reduced approximately tenfold by the PEG-end PU surface. This result indicates the achievement of PEG functionalization, and the PEG layer presented an efficient antifouling property. Cyclic voltammetry measurements were made for the PU interface on the gold surface. Figure 3.24d represents the electroactivity of the approximately 70 nm PU interface with a peak current value of 11 μA. This result proves that the PU-functionalized gold surface is electroactive.

3.3. Conclusion

Biosensors and implantable bioelectronic systems need a delicate balance at the interface between living beings and electronic systems. Metals or semiconductors offer a soft and stimulus-sensitive interface, as well as a well-defined interface opportunity. Non-specific binding generated by irreversible adsorption of bio-macromolecules could generate false-positive signals in a bioelectronic interface. To obtain an antifouling gold surface, oligo ethylene-glycol (OEG) terminated alkanethiol derivatives were used;

nevertheless, the solely OEG layer has limited robustness. By using activators regenerated by electron transfer (ARGET) ATRP and surface-initiated atom transfer radical polymerization (SI-ATRP) methodologies manufacture bio-repellent polymer functionalized surface. However, these methodologies have various drawbacks, like laborious steps with numerous chemicals and purification steps.

The XPS mapping analysis determines the optimum step number values of the SurfAst urethane polymerization. These results indicate that the optimum coating yield is achieved in six steps. A FTIR (VeeMAX III) spectroscopy and AFM images showed that performing SurfAst urethane polymerization with hexamethylene diisocyanate and 1,4-Butanediol demonstrated self-assembly-like properties by using the optimum condition and step number, resulting in an orientation of approximately 90° with respect to the surface. The results demonstrate that a novel gold functionalization methodology is suitable for the fabrication of the nanoporous polymer interface on a gold substrate.

In this chapter, the novel SurfAst methodology provides a polyurethane (PU) interface that does not need air-tight conditions, degassing, costly catalysts, a high number of chemicals, or tedious purification steps. The approximately 70 nm-thick nanoporous PU interface on a gold substrate is formed by the sequential incubation of HDI and 1,4-BDO. With four sequential (eight-step) reactions between BDO and HDI on the gold surface, the coating height should be about 9 nm. Indeed, it could be assumed that SurfAst urethane polymerization has occurred with high yield. SEM images and light microscope images after SurfAst urethane polymerization indicate that SurfAst urethane polymerization can be readily applied homogeneously on a large area with a sharp structure. The PU interface on the gold surface consists of two types of structures with rodlike domains and nanoporous structures. However, the adhesion force results show that rod-like structures that occur via parallel stacking of polyurethane bundles have an average of 13.30 nN while nanoporous structures have an average of 14.36 nN. Broadening of the XPS spectra peaks of C 1s, N 1s, and O 1s indicates that polymerization has taken place on the gold surface, especially when considering the XPS spectra of C 1s and N 1s after HDI incubation in Figure 2.10 (*Chapter 2*). Additionally, chemical mapping images of the PU interface represent carbon, oxygen, and nitrogen, and the sum of the C, N, and O promotes that the nanoporous structure is made from PU.

EFM monitoring is used to discover long-range interactions of the charged particles on the nanoporous PU. The results indicate that the interface tends to interact more with positively charged species, which had a phase shift of 1.57° while the

negatively charged species had a phase shift of 0.49°. Following the adhesion force and EFM investigation, the PU interface is post-functionalized with PEG 1000 to obtain antifouling properties. PEG post-functionalization reduced fluorescence intensity by approximately tenfold when compared with the PU interface. The results demonstrate that the PEG layer ensures an antifouling property. Additionally, cyclic voltammetry results describe the electroactivity of the PU interface with a peak current value of 11 μA. While Raman spectrum results show basic and specific all urethane bonds, FTIR spectra show that there are three types of hydrogen bonds at the PU interface, which has a mixed secondary interaction.

As a result of this chapter, gold surface functionalization with isocyanate gives a high yield, well-defined polymeric structureby using the novel SurfAst urethane polymerization method. This PU interface shows homogeneous mechanical and structural properties and could be post-functionalized by using active hydrogen compounds. In particular, the SurfAst methodology has promised the straightforward fabrication of an electroactive bio-interface with the antifouling property.

CHAPTER 4

CATIONIC POLYTHIOPHENE GRAFTING ON THE GOLD SURFACE

Conjugated polyelectrolytes (CPEs) containing a pendant ionic group on the polymer backbone are remarkable materials due to the control of their aromatic structure. Electron delocalization is modulated by the aromatic structure that determines the CPEs' optical and charge transport properties and is thus a remarkable material in the field of bioelectronics and sensors.[95] On the other hand, it has been found that the structural and chemical properties of the interfaces of conjugated polymers have a huge effect on device performance in the electronics field. The conjugated polymers show various electrical performances from the molecular structure and conformation that exhibit varying degrees of morphological disorder, from completely amorphous to polycrystalline.[96] Although microstructure films can be coated on substrates by using various methods (e.g., dip coating, spin-coating, and roll-to-roll processing) through secondary interactions, charge transport may no longer be valid by disrupting the initial film through the reorganization of the polymer chain or the removal of the underlying film on steam or solvent exposure.[97]

To overcome the stability problem, covalent bonding by *grafting to* conjugated polymers onto the substrate provides a solution to film instability by providing rigidity and solvent resistance to the semiconductor layers of the films. In addition, "freezing" the polymer chains in position has been shown to develop the electronic properties of the device.[96-99] Martin et al. demonstrated that thiol-ene click chemistry offers a simple method to graft functionalized poly(thiophene)s' well-oriented, electroactive, solvent-resistant, and ultrathin films on SiO_2 modified with (3-mercaptopropyl)triethoxysilane (Figure 4.1).[99] In addition, Davis et al. investigated the effect of photoinduced thiol-ene surface grafting on the optoelectronic properties of end-group and side-chain functionalized conjugated poly(fluorene).[98]

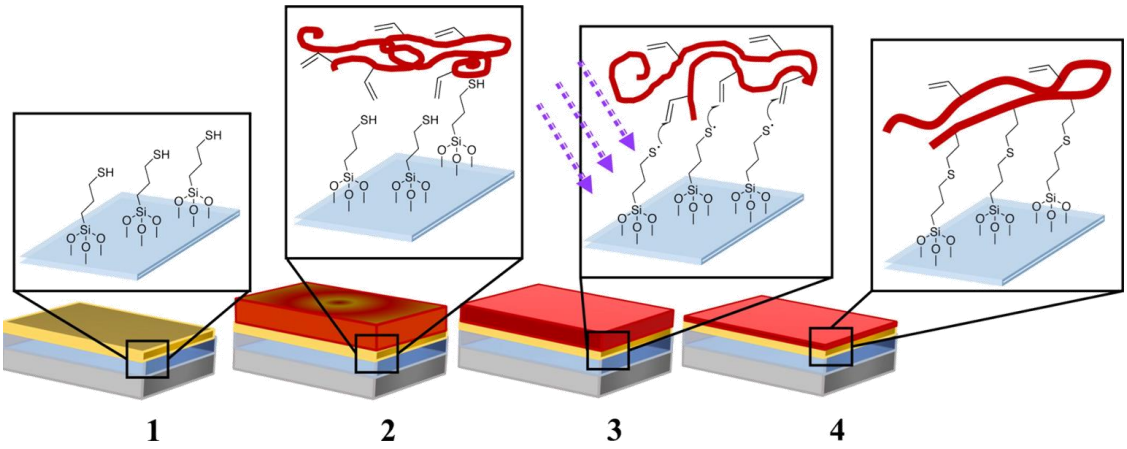

Figure 4.1. Illustration of thiol-ene grafting (1) monolayer fabrication, (2) spin coat of vinyl modified polythiophene, (3) UV light and heat treatment, and (4) washing step.[99]

This chapter investigate the structural effect of surface-assisted (SurfAst) urethane polymerization stamped and incubated with 11-mercaptoundecanoic acid on the gold surface. Also, the results demonstrate that a methacrylate-end PU interface is post-functionalized by poly(N-allyl-N-methyl-N-(3-((4-methylthiophen-3-yl)oxy)propyl)prop-2-en-1-aminium bromide as cationic polythiophene nanowire via a reaction between methacrylate and allyl groups on the gold surface.[100]

4.1. Materials and Methods

11-mercaptoundecanoic acid, 11-mercapto-1-undecanol, 1,4 butanediol (1,4-BDO), hexamethylene diisocyanate (HDI), 2-isocyanatoethyl methacrylate, acetone, ethanol, and DBTDL 95% were purchased from Sigma-Aldrich. Poly(N-allyl-N-methyl-N-(3-((4-methylthiophen-3-yl)oxy)propyl)prop-2-en-1-aminium bromide as cationic polythiophene was synthesized as described elsewhere.[101] Nanosurf AFM (Stat0.2LAuD - k = 0.2 N/m, static force) was used for the topographical characterization of gold surfaces. To investigate electrostatic properties, electrostatic force microscopy (EFM) measurements were applied in double-pass mode with a 40 nm height and charged by applying 0V, +2 V, and -2 V at room temperature (Multi75E-G - k = 3 N/m, dynamic force, tip lift: 40 nm).

Stamping procedure: 11-mercaptoundecanoic acid was used for gold surface activation. Polydimethylsiloxane (soft lithography - PDMS) stamp was incubated in 1mM

11-mercaptoundecanoic acid in ethanolic solution for five minutes. The stamp was dried by a jet of nitrogen. The stamp was placed on the gold surface by applying slight pressure to ensure good contact and was then passivated to the surface. The stamp remained in contact for five minutes, and the gold surface was rinsed with plenty of EtOH.

The 11-mercaptoundecanoic acid stamped gold surface was incubated with 1mM 11-mercapto-1-undecanol in ethanolic solution overnight. After incubation, the gold surface was rinsed with plenty of EtOH (backfilling procedure). The gold surface was incubated with HDI in acetone at 40°C for 20 minutes (step one). Then, the gold surface was incubated with 1,4-BDO in acetone at 40°C for 20 minutes (step two). The stamping surface experiment consisted of eight steps that included step one and step two, respectively (Figure 4.2).

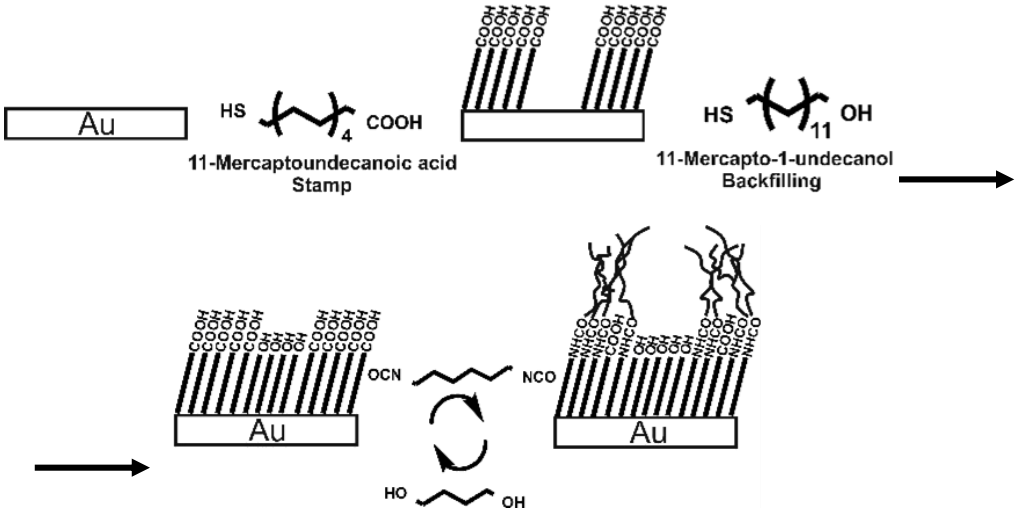

Figure 4.2. Fabrication of the stamping surface.

Surface 1: The gold surface was incubated with 1mM 11-mercaptoundecanoic acid in ethanolic solution overnight. After incubation, the gold surface was rinsed with plenty of EtOH. The gold surface was incubated with HDI in acetone at 40°C for 20 minutes (step one). Then, the gold surface was incubated with 1,4-BDO in acetone at 40°C for 20 minutes (step two). The surface 1 experiment consisted of seven steps that included step one and step two, respectively. The hydroxyl-end gold surface was incubated with 2-isocyanatoethyl methacrylate in the last step (step eight) to obtain methacrylate-end PU interface (Figure 4.3).

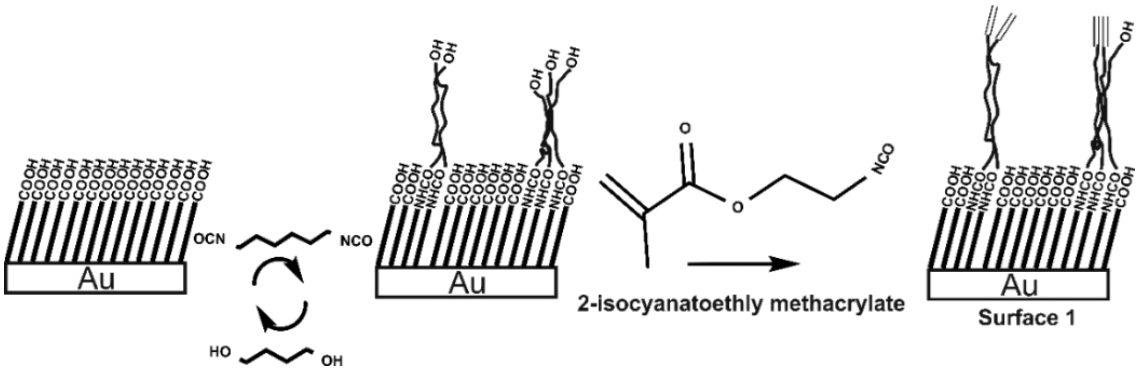

Figure 4.3 Fabrication of surface 1.

Surface 2: Surface 1 (methacrylate-end PU interface) was irradiated with 1.8% Irgacure in ethylene glycol (EG) solution (Figure 4.4).

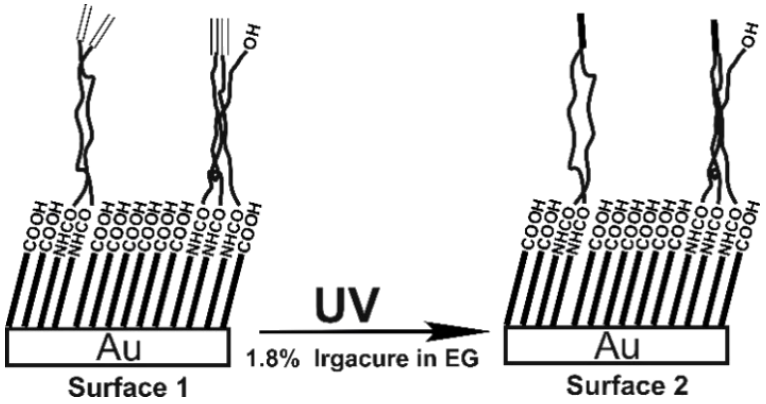

Figure 4.4 Fabrication of surface 2.

Surface 3: Surface 1 (methacrylate-end PU interface) was irradiated with 1.8% Irgacure in ethylene glycol (EG) solution with poly(N-allyl-N-methyl-N-(3-((4-methylthiophen-3-yl)oxy)propyl)prop-2-en-1-aminium bromide (cationic polythiophene (PT)) (Figure 4.5).

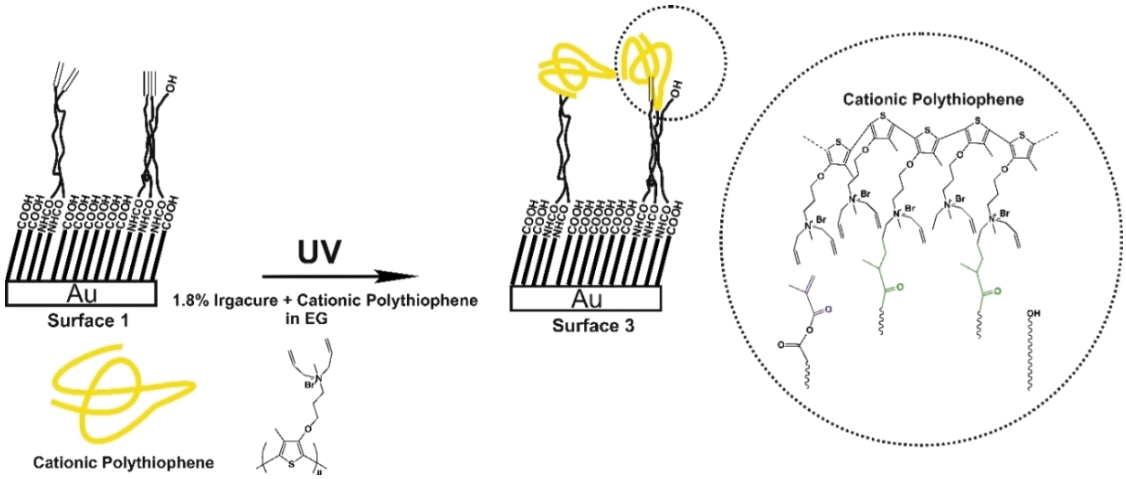

Figure 4.5 Fabrication of surface 3.

Surface 4: After RCA cleaning, the gold surface was incubated with HDI in acetone at 40^{o}C for 20 minutes (step one). Then, the gold surface was incubated with 1,4-BDO in acetone at 40°C for 20 minutes (step two). The surface 4 experiment consisted of seven steps that included step one and step two, respectively. The hydroxyl-end gold surface was incubated with 2-isocyanatoethyl methacrylate in the last step (step eight) to obtain methacrylate-end PU interface. After step eight, the gold surface was irradiated with 1.8% Irgacure in ethylene glycol (EG) solution with poly(N-allyl-N-methyl-N-(3-((4-methylthiophen-3-yl)oxy)propyl)prop-2-en-1-aminium bromide (cationic polythiophene (PT)). Finally, the gold surface was washed with plenty of water (Figure 4.6).

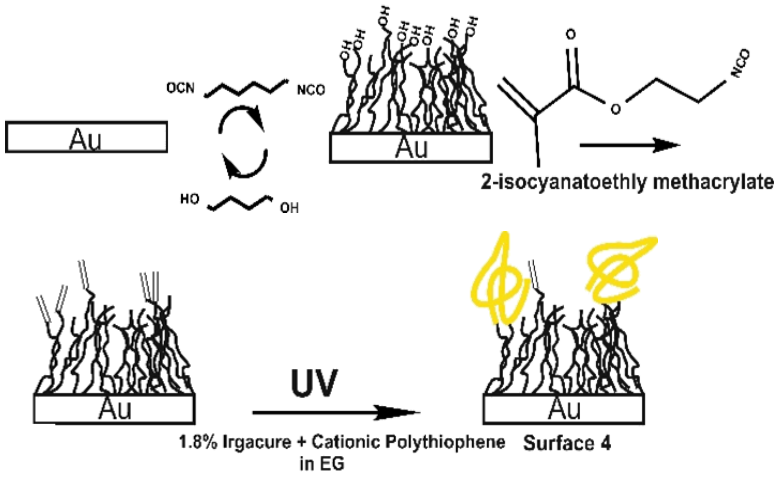

Figure 4.6 Fabrication of surface 4.

4.2. Results and Discussion

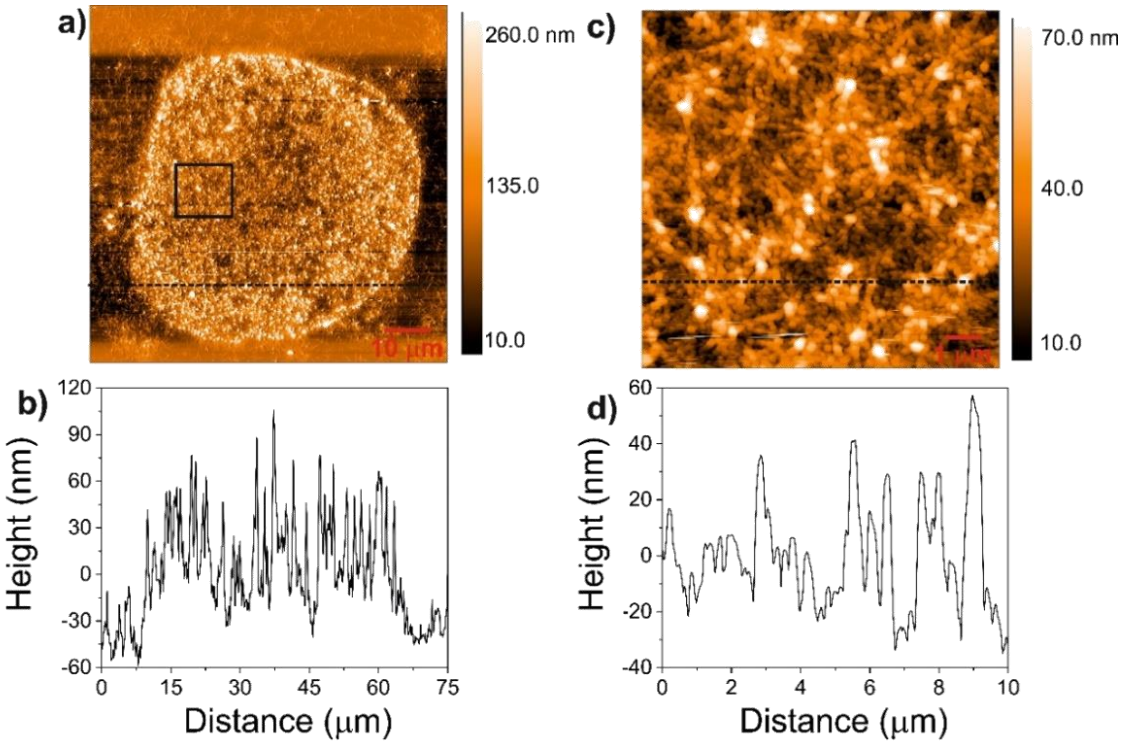

Figure 4.7. a, b) AFM height image and cross-section (black dashed line) after eight steps of SurfAst polymerization of the 11-mercaptoundecanoic acid stamped gold surface. c, d) AFM height image and cross-section (black dashed line) of a magnified view of Figure 4.7a (solid black square).

Figure 4.7a shows the AFM image of the gold surface of eight steps of SurfAst polymerization (four sequential reactions between 1,4-BDO and HDI) after the 11-mercaptoundecanoic acid stamped gold surface and the 11-mercapto-1-undecanol backfilling on the gold surface. First, the incubation of hexamethylene diisocyanate (HDI) on the gold surface initially could yield the acid-anhydride, which leads to the amide after decarboxylation.[102] At the second step, an isocyanate functionalized surface (stamped area) is then incubated with 1,4-BDO (1,4-butanediol) to form a urethane bond. In the third step, the hydroxyl end group of 1,4-BDO remains unreacted and incubated HDI to form urethane once again. The multiple sequential incubations yield a nanoporous polyurethane (PU) layer with a sharp border on the 11-mercaptoundecanoic acid stamped gold surface. In Figure 4.7b, a cross-section image shows the average height distribution is 130 nm. In Figure 4.7c, the PU interface shows bundle-like structures that gather polymer chains. In Figure 4.7d, the PU interface at the patterned area is found to be

various height values between 30 and 90 nm. The average surface roughness is nearly 150 nm. These results assure that the bundle-like PU structure is obtained by applying the SurfAst reaction on the 11-mercaptoundecanoic acid stamped gold surface.

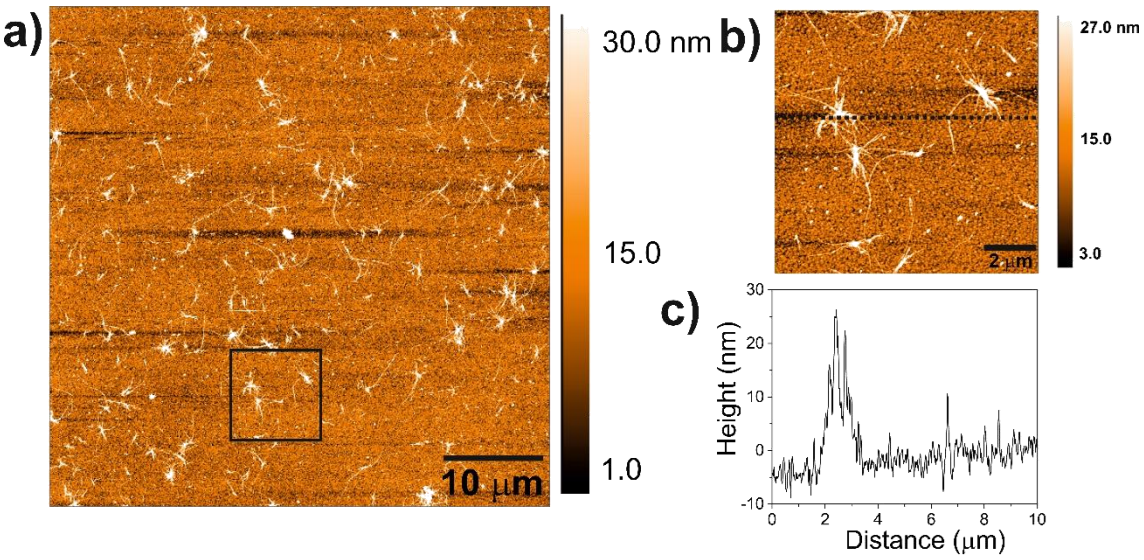

Figure 4.8 a) AFM height image and cross-section (black dashed line) of the 2-isocyanatoethyl methacrylate end gold surface (surface 1). b, c) AFM height image and cross-section (black dashed line) of a magnified view of Figure 4.8a (solid black square).

The incubation of 11-mercaptoundecanoic acid created a self-assembled structure on the gold surface. However, a pin hole and other defects may exist in the monolayer on the gold surface.[103] Sabatani and Rubinstein demonstrated that the pin-hole defects are distributed as an array of extremely small ultramicroelectrodes.[104] Thus, the SurfAst polymerization may start from these pin-hole defects with the gold-isocyanate interaction that was demonstrated in *Chapter 3*.

Figure 4.7 shows that carboxylic acid groups react with isocyanate. On the other hand, SurfAst polymerization can be initiated between the carboxylic acid groups of 11-mercaptoundecanoic acid, which have weak secondary interactions on the gold surface since the reactivity of isocyanates toward carboxylic acids is much lower than the one with amines, alcohols, and water.[37] Figure 4.8a shows the AFM image of eight steps of SurfAst polymerization of the gold surface after incubation with 11-mercaptoundecanoic acid. The hydroxyl-end PU interface (step seven) was incubated with 2-isocyanatoethyl methacrylate in the last step (step eight), and a methacrylate functionalized surface was

obtained. Figures 4.8b and c show the AFM height image and cross-section of a magnified view of Figure 4.8a. While an interwoven thread-like PU structure has a 40 nm area roughness, the well-ordered 11-mercaptoundecanoic acid region has a 7 nm area roughness that is similar to the bare gold surface's roughness. Also, interwoven thread-like PU structures have centers with an average 40 nm height and fibers with ~200 nm width (7 nm height profile) and ~1µm length. These results demonstrate that a thread-like PU interface yielded on the gold surface, which increases the roughness of the surface.

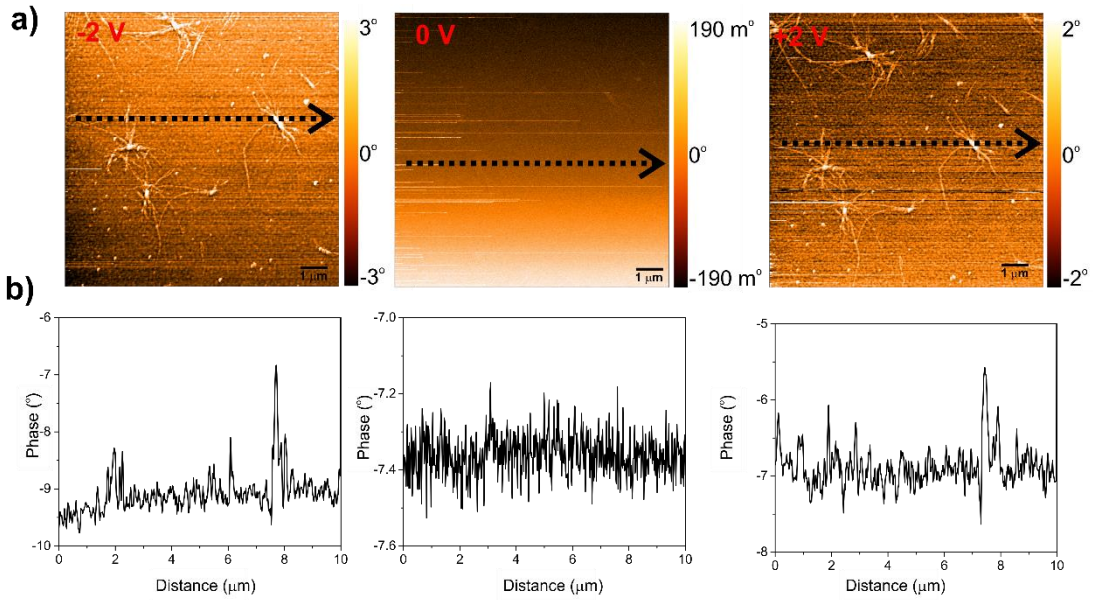

Figure 4.9. a) EFM image of the 2-isocyanatoethyl methacrylate end gold surface (surface 1) with -2, 0, and +2 V, respectively. b) Phase shift profiles.

EFM is used to determine the electrostatic interactions that are assumed to be long-range interactions of interwoven thread-like PU structures. Considering the differentiation of the phase to the tip voltage graph of the interwoven thread-like PU structures and the gold surface, the tip voltage was chosen as ±2 volts; also, the tip voltage 0 V was carried out to reference the EFM measurement in Figure 4.9a. All EFM measurements were conducted in double-pass mode with a 40 nm second tip lift in *Chapter 4*. Figure 4.9b represents the EFM (phase shift) measurement for ±2 volts and the tip voltage 0V. In Figure 4.9b, the Vtip set to -2V causes a 2.30° phase shift between the polymer and the gold layer. When the Vtip is set to +2V, it causes a 1.80° phase shift between the polymer and the gold layer. These results show that negatively charged species cause slightly stronger electrostatic interactions than positively charged species.

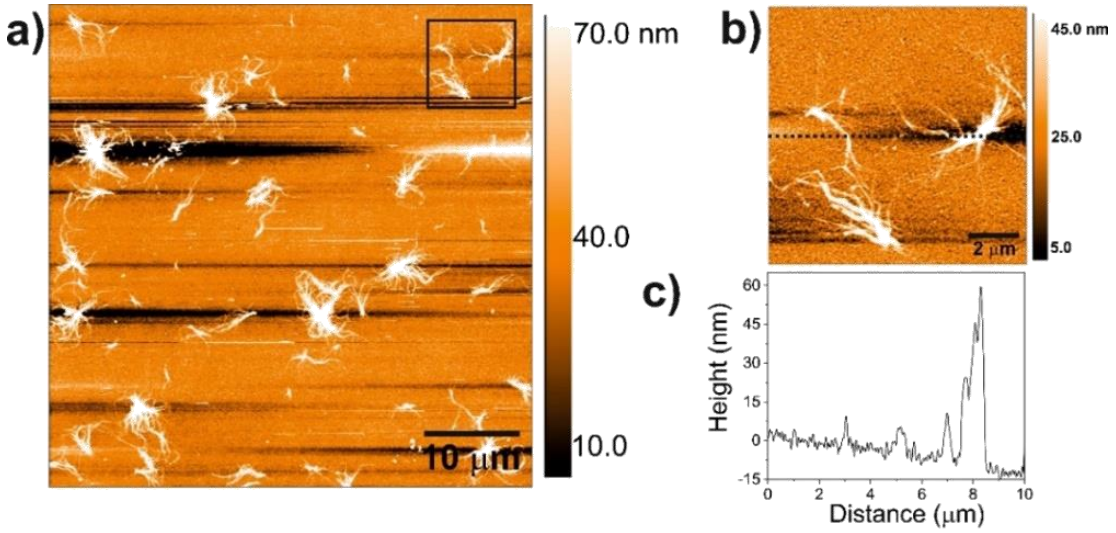

Figure 4.10 a) AFM height image of UV curing after 2-isocyanatoethyl methacrylate-end surface (surface 2). b, c) AFM height image and cross-section (black dashed line) of a magnified view of Figure 4.10a (solid black square).

Figure 4.10a shows the AFM image after the gold surface 1 was irradiated with 1.8% Irgacure in ethylene glycol (EG) solution. A self-assembled monolayer structure has a highly ordered structure with a secondary interaction between thiol molecules on the gold surface, which creates an antifouling surface that decreases the tendency to react.[105] Methacrylate groups on the gold surface could be interconnected by UV irradiation; therefore, the PU interface could fabricate a woven-like structure. Figures 4.10b and c show the AFM height image and cross-section of a magnified view of Figure 4.10a. While a woven-like PU structure has a 100 nm area roughness, the well-ordered 11-mercaptoundecanoic acid region has a 6 nm area roughness that is similar to the bare gold surface's roughness. Also, woven-like PU structures have dense centers with an average 80 nm height and fibers with ~300 nm width (13 nm height profile) and ~2μm length. These results demonstrate that a woven-like PU yielded on the gold surface, which increases the roughness of the surface.

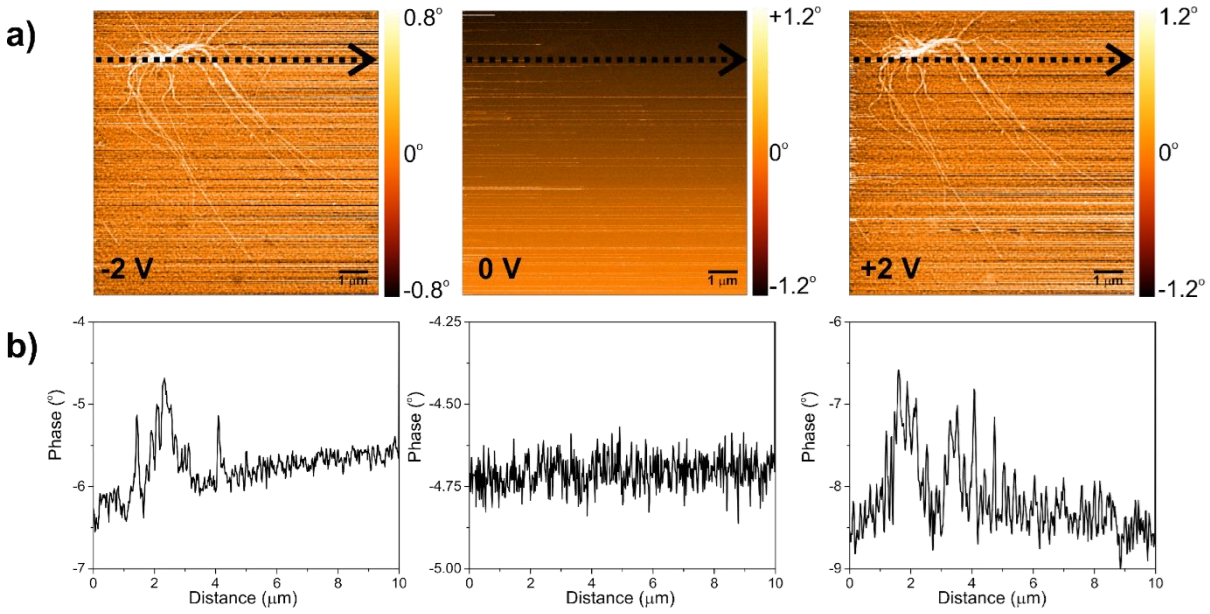

Figure 4.11 a) EFM image of UV curing after 2-isocyanatoethyl methacrylate-end surface (surface 2) with -2, 0, and +2 V, respectively. b) Phase shift profiles.

EFM is used to determine the electrostatic interactions that are assumed to be long-range interactions of woven-like PU structures at atmospheric pressure. Considering the differentiation of the phase to the tip voltage graph of the woven-like PU structures and the gold surface, the tip voltage was chosen as ±2 volts; also, the tip voltage 0V was carried out to reference the EFM measurement in Figure 4.11a. Figure 4.11b represents the EFM (phase shift) measurement for three different voltages applied to the tip. In Figure 4.11b, the Vtip set to -2V causes a 1.53° phase shift between the polymer and the gold layer. When the Vtip is set to +2V, it causes a 1.70° phase shift between the polymer and the gold layer. These results show that positively charged species cause almost the same electrostatic interactions as negatively charged species.

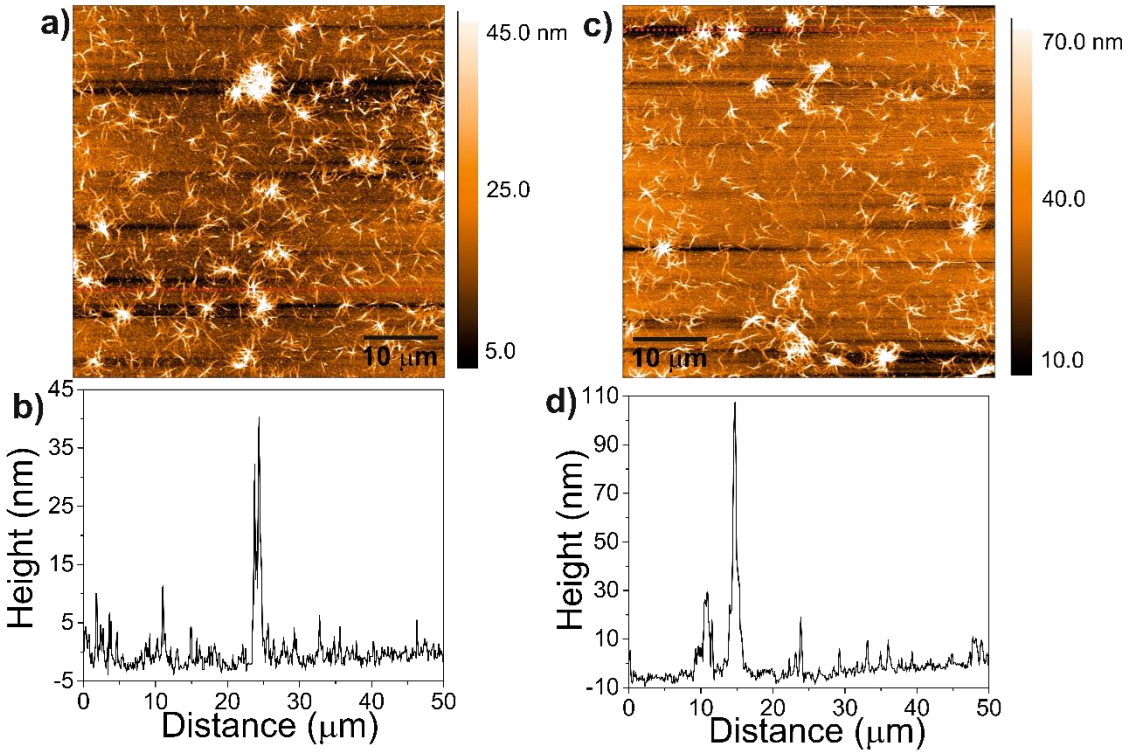

Figure 4.12. a, b) AFM height image of UV curing Poly(N-allyl-N-methyl-N-(3-((4-methylthiophen-3-yl)oxy)propyl)prop-2-en-1-aminium bromide) on the 2-isocyanatoethyl methacrylate-end gold surface (surface 3). c, d) Cross-section (red dashed line).

Figures 4.12a and b show the AFM image after the gold surface 1 was irradiated with 1.8% Irgacure in ethylene glycol (EG) solution with cationic polythiophene. Methacrylate groups could be linked with an allyl group of cationic polythiophene by UV irradiation on the gold surface; therefore, the PU interface could fabricate a nanowire PT structure.[100] Our group has recently demonstrated that ethylene glycol is a good solvent of cationic polythiophene and obtained single-chain cationic polymer dots (Pdots) structure using a water-ethylene glycol solvent system.[106] In addition, since the cationic polymer swells in ethylene glycol as a good solvent, the good solvent can increase the reaction efficiency between the acrylate group on the gold surface and the allyl group of the cationic polymer. Chen et al. synthesized a regioregular poly(3-hexylthiophene)-block-poly(3-bromohexylthiophene) (P3HT-b-P3BrHT) block copolymer with various block ratios.[107] Nanowire structures induced by pi-pi stacking were obtained in P3HT-b-P3BrHT with 70:30 and 50:50 block ratios. They also showed that P3BrHT content higher than 50% significantly disrupted the polymer chain and reduced crystallization. On the

other hand, Danielsen et al. synthesized the P3BrHT:P3HT copolymer and obtained charge ratios ranging from 0 to 1 by the Menshutkin amine quaternization reaction. The results showed that the persistence lengths of all charge ratios were approximately 3 nm, which indicates that electrostatic rigidity is ineffective for conjugated polyelectrolytes with pendant charges in dilute solutions.[95] According to the study, nanowire PT could be considered a mixture of semiflexible or rigid rod structures of polymer backbone behavior. Figures 4.12c and d show the AFM image and the cross-section, respectively. While a nanowire PT structure has a 70 nm area roughness, the well-ordered 11-mercaptoundecanoic acid region has a 5 nm area roughness that is similar to the bare gold surface's roughness. The nanowire PT structure shows dense centers with an average 100 nm height and fibers with ~250 nm width (12 nm height profile) and ~7µm length.

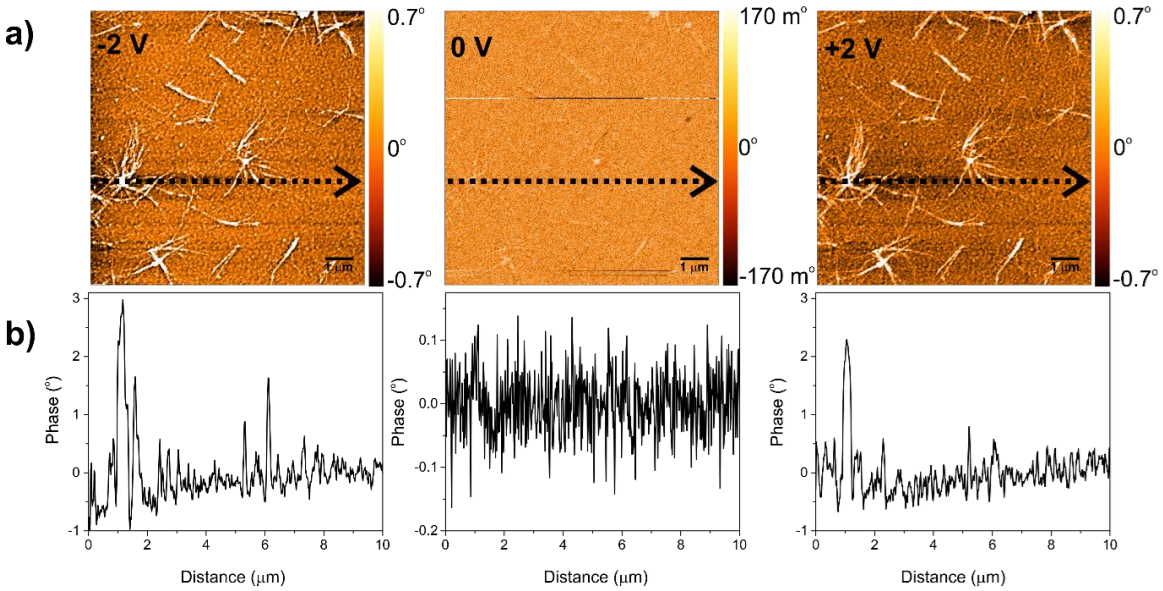

Figure 4.13. a) EFM image of UV curing Poly(N-allyl-N-methyl-N-(3-((4-methylthiophen-3-yl)oxy)propyl)prop-2-en-1-aminium bromide) on 2-isocyanatoethyl methacrylate-end gold surface with -2, 0, and +2 V, respectively (surface 3). b) Phase shift profiles.

Considering the phase shift of the nanowire PT structure and the gold surface, the tip voltage was chosen as ±2 volts, and 0V was carried out to reference the EFM measurement (Figure 4.13a). Figure 4.13b represents the EFM (phase shift) measurement for three different voltages applied to the tip. In Figure 4.13b, the Vtip was set to -2V, causing a 3.81° phase shift between the nanowire PT structure and the gold layer. When

the Vtip was set to +2V, it caused a 2.74° phase shift between the nanowire PT structure and the gold layer. These results show that negatively charged tip cause stronger electrostatic interactions than positively charged species due to the effect of the cationic polythiophene on the gold surface.

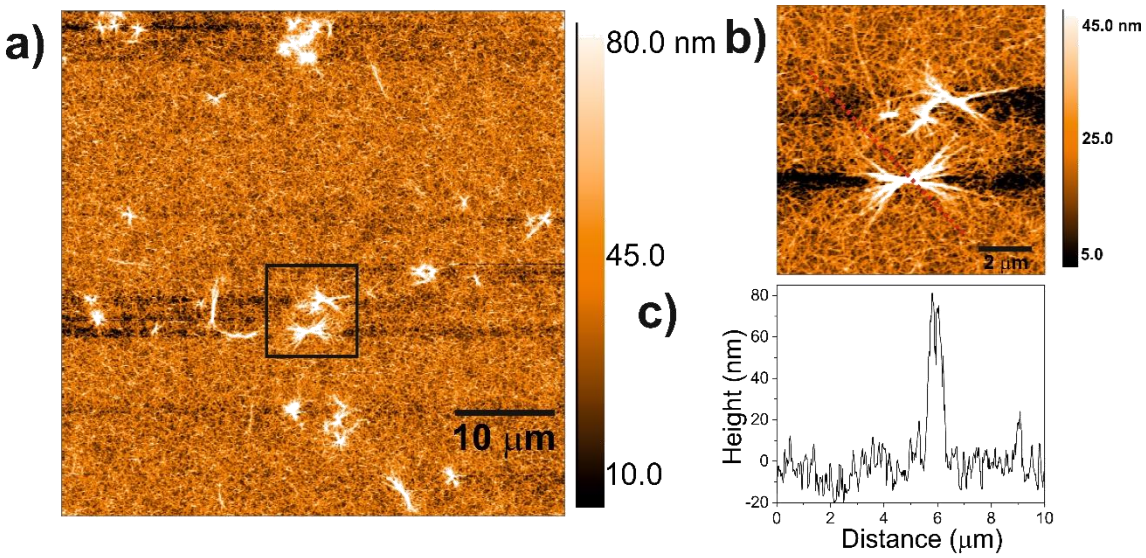

Figure 4.14. a) AFM height image of UV curing Poly(N-allyl-N-methyl-N-(3-((4-methylthiophen-3-yl)oxy)propyl)prop-2-en-1-aminium bromide) on the 2-isocyanatoethyl methacrylate-end PU interface on the gold surface (surface 4). b and c) AFM height image and cross-section (red dashed line) of a magnified view of Figure 4.14a (solid black square).

Chapter 3 presents a well-defined and homogeneous PU interface with SurfAst urethane polymerization by utilizing the isocyanate modified gold surface. Figure 4.14a shows the AFM image height image of UV curing cationic polythiophene on the 2-isocyanatoethyl methacrylate-end PU interface on the gold surface (surface 4). Surface 4 can be considered the control surface to prove whether the cationic polythiophene is grafted to the surface. While 11-mercaptoundecanoic acid forms the ground of surface 1, 2, and 3, the PU interface composes the basis of the surface on surface 4. Therefore, the average surface roughness of surface 4 of the non-grafted area (surface region without the cationic polythiophene) is 50 nm, while the previous surfaces are around 5 nm. These results show that the PU interface can be post-functionalized by the reaction between the acrylate group-end PU surface and the allyl group of the cationic polymer. Figure 4.14a shows that the cationic polythiophene is formed by many short filament-like structures

growing from a center. It could be assumed that the PU structures were fabricated using the *grafting from* methodology and the nanowire PT structures were fabricated using the *grafting to* methodology. It is observed that the PU structures give a higher yield polymer brush, while the nanowire PT structures provide a lower yield grafting on the gold surface as discussed in *Chapter 1* (1.4.1 Grafting from and Grafting to Methodologies) where the grafting methodologies are compared. The cationic polythiophene grafted area has a 170 nm area roughness with an average 120 nm height of the center and filament-like structures with ~240 nm width (40 nm height profile) and ~1.5 µm length (Figures 4.14b and c).

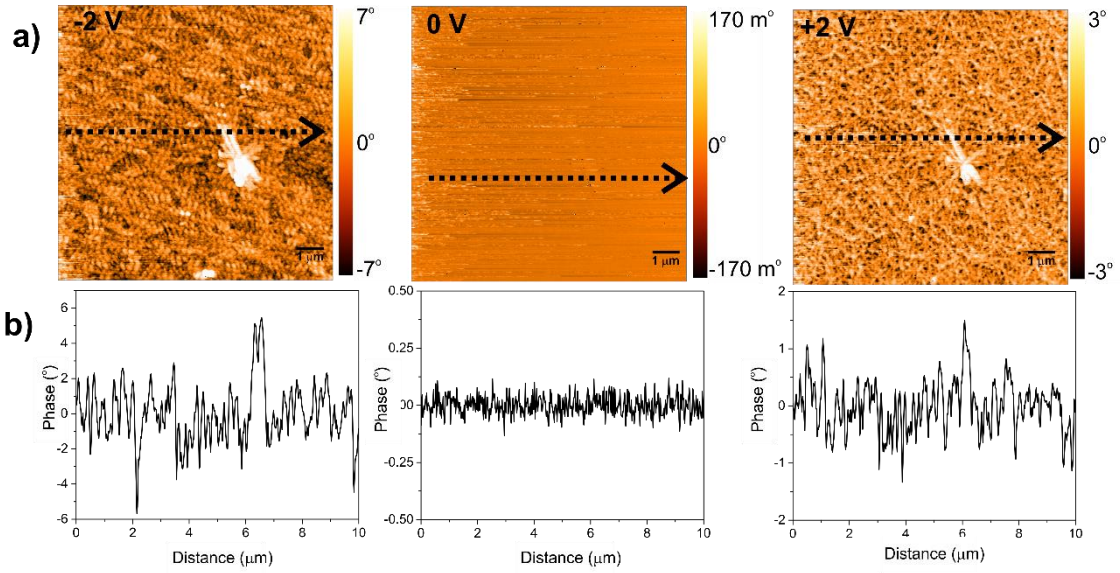

Figure 4.15 a) EFM image of UV curing Poly(N-allyl-N-methyl-N-(3-((4-methylthiophen-3-yl)oxy)propyl)prop-2-en-1-aminium bromide) on the 2-isocyanatoethyl methacrylate-end PU interface on the gold surface (surface 4) with -2, 0, and +2 V, respectively. b) Phase shift profiles.

To determine the phase shift of the nanowire PT structure on the PU surface, the tip voltage was chosen as ±2 volts, and 0V (Figure 4.15a). Figure 4.15b represents the EFM (phase shift) measurement for three different voltages applied to the tip. In Figure 4.15b, the Vtip was set to -2V, causing a 3.28° phase shift between the nanowire PT structure and the PU layer. When the Vtip was set to +2V, it caused a 1.12° phase shift between the nanowire PT structure and the PU layer. These results show that negatively charged tip cause three-fold stronger electrostatic interactions than positively charged species due to the effect of the cationic polythiophene on the PU surface.

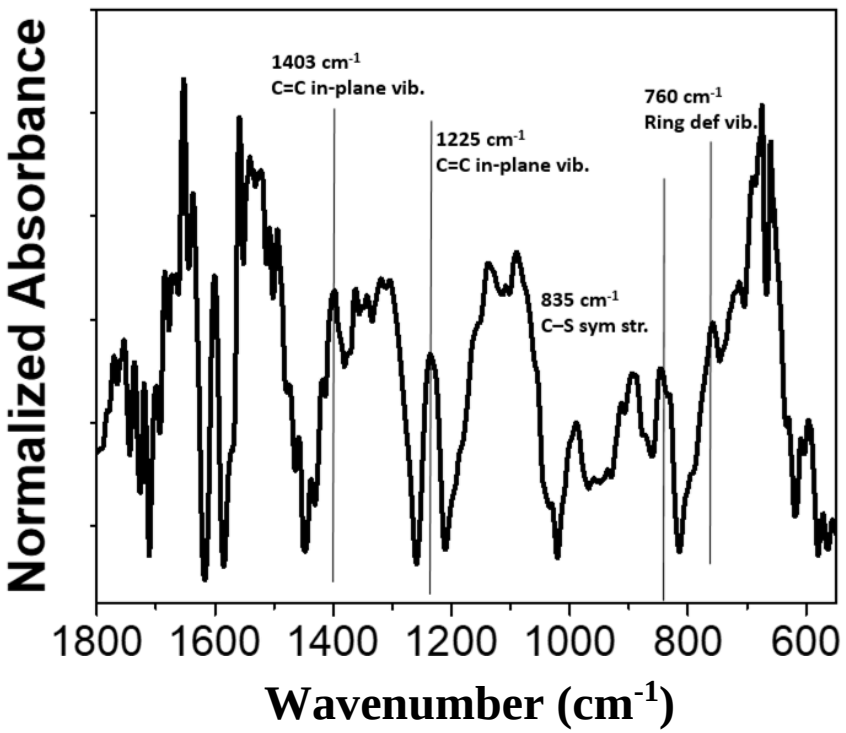

Figure 4.16. FTIR spectrum of surface 3.

A functional group analysis of cationic polythiophene grafted on the gold surface was performed by Fourier-transform infrared (FTIR) spectroscopy. As shown in Figure 4.16, the FTIR spectrum of the gold surface exhibits in-plane vibration C=C of thiophenes at 1403 cm^{-1} and 1225 cm^{-1}. C-S symmetric stretching is found at 835 cm^{-1} while C-S asymmetric stretching is found at 895 cm^{-1}. Also, the peak observed at 760 cm^{-1} could be attributed to a ring deformation vibration.[76]

4.3. Conclusion

In the electronics field, it has been noted that the structural properties and chemical stability of conjugated polymers on the surface have a huge effect on device performance. In this chapter, we investigate the structural properties of *grafting to* poly(N-allyl-N-methyl-N-(3-((4-methylthiophen-3-yl)oxy)propyl)prop-2-en-1-aminium bromide as a conjugated polymer by using the surface-assisted (SurfAst) urethane polymerization method on the stamped/incubated 11-mercaptodecanoic acid gold surface.

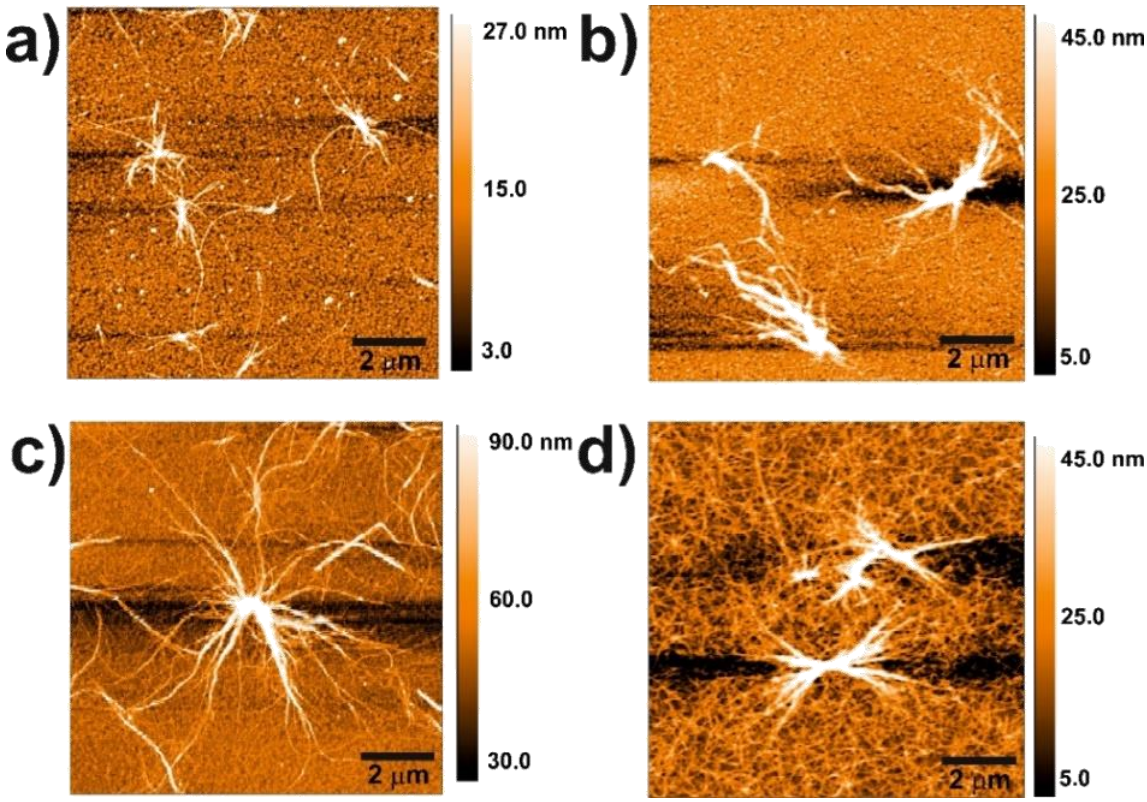

Figure 4.17. AFM height image comparison of a) Surface 1, b) Surface 2, c) Surface 3, and d) Surface 4.

In summary, the grafted area of surface 1 has the lowest roughness, which could be due to the separate acrylate groups that form when UV irradiation does not perform. After the UV was applied to surface 1 has more than twofold the surface roughness value (surface 2). The non-grafted area on the gold surface has area-roughness values very similar at surfaces 1, 2, and 3 because the non-grafted area consists of SAM units of 11-mercaptoundecanoic acid, and there is no additional polymeric interface. However, since there are no SAM units of 11-mercaptoundecanoic acid on surface 4, the non-grafted area (PU interface) has an area roughness of about 40 nm. UV irradiated surfaces could be assumed, as the growing filaments start from a center (Figure 4.17). The central heights of the cationic polythiophene grafted surfaces are similar; however, the center height of the UV irradiated surface without cationic polythiophene (surface 2) is lower. This may be caused by the cationic polythiophene reactions with the 2-isocyanatoethyl methacrylate-end gold surface, which result in a higher graft center with an increased amount of polymer (Table 4.1).

Figure 4.18 shows EFM images (-2V) comparison of surface 1, surface 2, surface 3, and surface 4. The phase shift values of the EFM images that show similar images to the AFM height images are 2.30°, 1.53°, 3.81°, and 3.28°, respectively. The phase shift values of surfaces 3 and 4 containing cationic PT nanowires are similar while higher than surfaces 1 and 2. This significant change in phase shift value could be assumed as an alternative characterization technique of *grafting to* PT nanowire by using EFM.

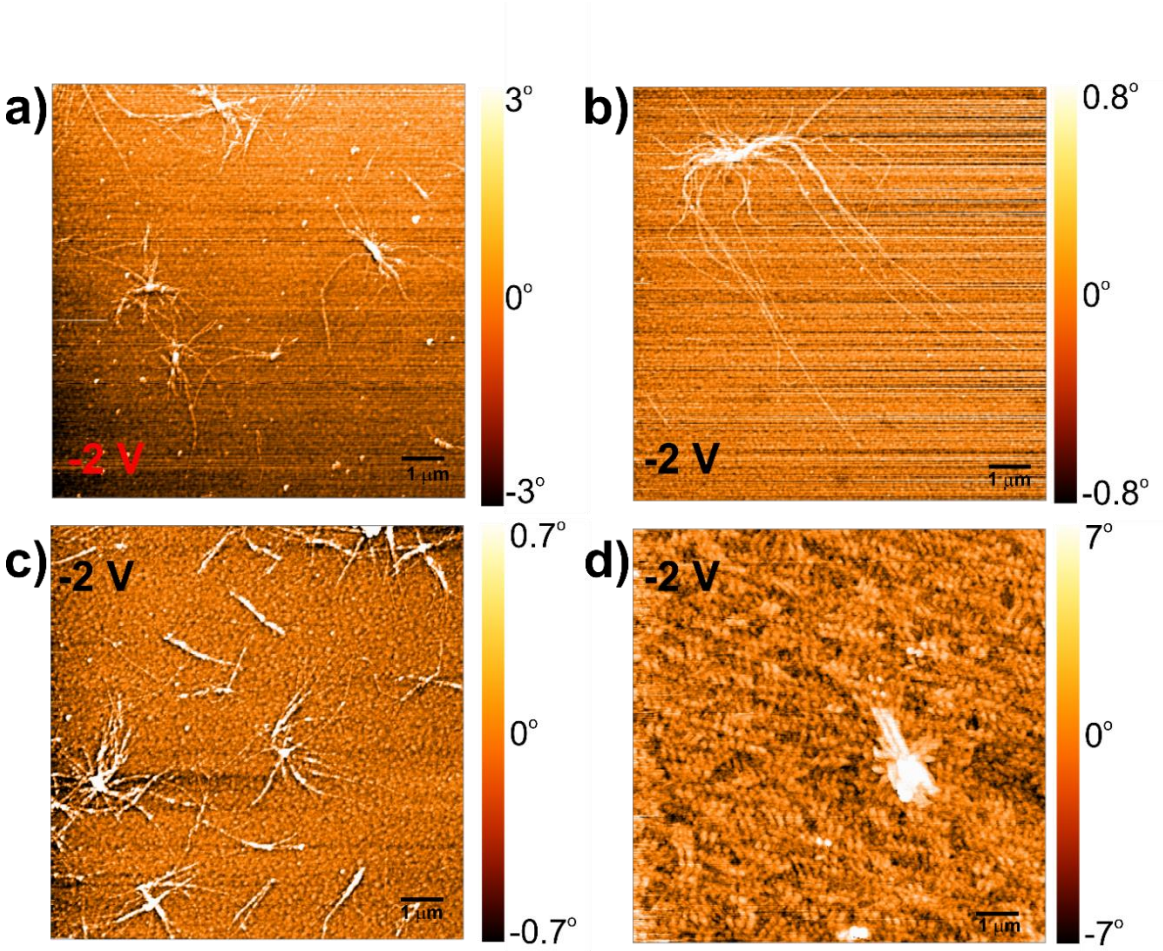

Figure 4.18. EFM image comparison of -2V a) Surface 1, b) Surface 2, c) Surface 3, and d) Surface 4.

Table 4.1. The comparative results of AFM height images between surface 1, surface 2, surface 3, and surface 4.

	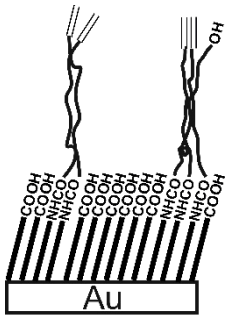 Surface 1	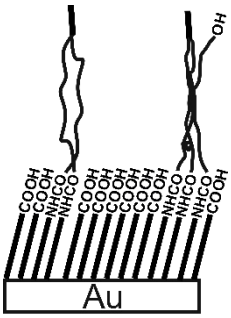 Surface 2	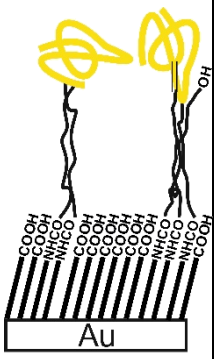 Surface 3	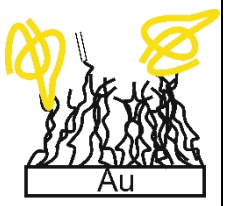 Surface 4
Roughness (grafted-area)	40 nm	100 nm	80 nm	170 nm
Roughness (non-grafted-area)	10 nm	5 nm	4 nm	35 nm
Center height	40 nm	80 nm	100 nm	120 nm
Width/ height	200nm / 7 nm	300nm / 13 nm	250nm / 12 nm	300 nm / 40 nm
Length	1 µm	2 µm	7 µm	1.5 µm
EFM -2V/+2V	$2.30^{\circ}/1.80^{\circ}$	$1.53^{\circ}/1.70^{\circ}$	3.81°/2.74°	3.28°/1.12°

To conclude, the AFM images show that the eight steps of SurfAst polymerization of 11-mercaptoundecanoic acid stamped on the gold surface yield a bundle-like polyurethane (PU) layer with a sharp border and an average height distribution of 130 nm. After the gold surface was incubated with 11-mercaptoundecanoic acid, the 2-isocyanatoethyl methacrylate-end SurfAst polymerization (surface 1) provided an interwoven thread-like PU structure with an average 40 nm height and fibers with ~200 nm width (7 nm height profile) and ~1μm length. The irradiation of surface 1 with the presence of 1.8% irgacure in ethylene glycol (EG) solution could be initiated with a reaction between methacrylate groups, which fabricated woven-like PU structures (surface 2) with an average 80 nm height, fibers ~300 nm width (13 nm height profile), and ~2μm length. In addition, the irradiation of surface 1 with the presence of 1.8% irgacure and cationic polythiophene in ethylene glycol (EG) solution could be initiated with a reaction between methacrylate groups and cationic polythiophene, which fabricated rod-like PU-PT structures (surface 3) with an average 100 nm height, fibers ~250 nm width (12 nm height profile), and ~7μm length.

CHAPTER 5

NANOGEL FORMATION BY REACTIVE LAYER-BY-LAYER ASSEMBLY

Reactive *layer-by-layer assembly* (rLBL) is a multilayered grafting technique that ensures a robust, post-functionalizable, erosion-resistant polymer coating on solid substrates.[21, 108] Unlike non-covalent LBL assembly, which utilizes electrostatic interactions, host-guest interactions and hydrogen bonding, rLBL is formed by the fast cross-linking reaction of functional groups between at least two different polymer layers at the interface. Previous studies have utilized condensation reactions between carbonyl groups and nucleophiles for the rLBL. Bergbreiter et al. performed the utilization of poly(maleic anhydride)-c- poly(methyl vinyl ether) copolymer as an electrophile to ensure the nucleophilic attack of amine- or hydroxyl-terminated generation five (G5) poly(amidoamine) or G5 poly(iminopropane-1,3-diyl) dendrimers.[109-111] Lynn et al. demonstrated the stepwise LBL nucleophilic addition of the amines of polyethyleneimine (PEI) to the carbonyl group of poly(2-vinyl-4,4- dimethlyazalactone).[112] Caruso group utilized Cu (I) catalyzed azide-alkyne [3 + 2] cyclo-additions to form 1,2,3-triazole for rLBL on quartz substrates.[113] Hawker et al. demonstrated that [3 + 2] cycloadditions could be used for LBL assembly on silicon wafers.[114]

Ultra-high stiff free-standing rLBL thin films with a tensile strength of 15.6 GPa approaching hard ceramics have been demonstrated by Kotov et al.[115] Decher et al proposed epoxy/PEI to improve the abrasion resistance of rLBL, and the rLBL covered films showed 2% loss after 25 abrasion cycles.[116] The rLBL methodology has also been used to increase the antifouling properties of the surface and free-standing films. Post-modification of polyacrylic acid (PAA) and PEI multilayers with polyethylene glycol (PEG) provided good protection against biofouling for five months with surface wettability.[117] In addition, rLBL methodologies have been used to increase the biocompatibility of substrates.[118-120]

Electrodes modified with rLBL provided a wide range of advantages like high anti-corrosive properties, stable detection performances after long device storage, and capacity loss after charge-discharge cycles.[121-128] Well-designed rLBL modified

electrodes ensure numerous benefits in biosensor technologies, like increasing the biocompatibility of the electrode, controlling electron transfer, creating protective layers to control diffusion, and increasing probe immobilization efficiency.[129-131] For instance, Qu, F. et al. showed that rLBL nanogel modified with ferrocene can be used for the electrochemical determination of glucose. The glucose biosensor with high sensitivity, wide linear range, short response time, and good stability has been achieved in favor of improved enzyme loading and efficient electron transfer; however, the nanogel does not covalently bond to the electrode surface (Figure 5.1).[132] Freeman, M. et al. carried out research on nanomaterial-supported electrochemical detection with an amperometric glucose biosensor having hexanediol-protected gold nanoparticles (NP) in a xerogel matrix.[133] Zhai, D. et al. Fabricated the glucose sensor with a Pt nanoparticle (NP)/polyaniline (PAni) heterostructured hydrogel that combined the advantages of both a nanoparticle catalyst and a conductive hydrogel with its three-dimensional porous structure.[134]

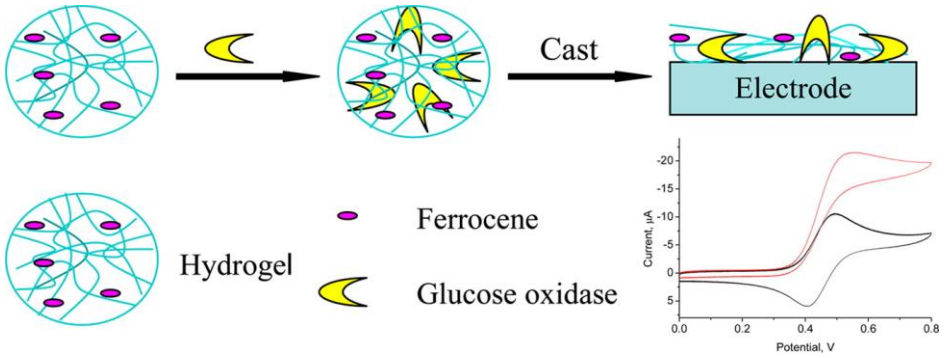

Figure 5.1 Illustration of hydrogel prepared from ferrocene modified amino acid as a highly efficient immobilization matrix.[132]

In the *Chapter 3*, it was shown that the nanometer-sensitive height control is achieved by a surface assisted (SurfAst) urethane polymerization methodology based on gold-isocyanate interaction. This chapter mainly involves forming nanometer-thick gels using an isocyanate-gold interaction for the rLBL methodology with the aza-Michael addition reaction of branched polyethyleneimine (BPEI) and polyester with triple bonds. A homogeneous nanogel coating produced by rLBL assembly via the rapid condensation reaction of the -NH2 groups of BPEI and the alkyne group of PE on a gold surface was obtained. This soft biointerface may be useful for bioamperometric type glucose sensors, as the nanogel property can maintain the distance between the layers and provide

openings that facilitate charge/substance transfer.[133, 134] Moreover, while the 3D network of rLbL can enhance enzyme loading ability, the NH_2 terminated structure could potentially be a scaffold for cell adhesion, DNA immobilization, and protein adsorption.[135-138]

5.1. Materials and Methods

Dibutyltin dilaurate, 11-mercapto-1-undecanol, branched polyethyleneimine, hexamethylene diisocyanate, and ferrocene carboxaldehyde were purchased from Sigma Aldrich. Polyester (PE) was synthesized as reported by a previous study.[139] PerkinElmer Spectrum 100 FTIR with VeeMAX III Accessory was utilized for infrared measurements. A topographical characterization of nanogel was performed by using Nanosurf AFM (Stat0.2LAuD: k = 0.2 N/m). An XPS analysis was done at a pass energy of 30 eV. Al Kα Monochromatic beam was used with a spot size of 50 μm. A 160 mM HDI solution was prepared with 90 x 10^{-3} mM DBTDL catalyst in acetone. In the first step, the gold surface was incubated in the HDI solution at 40°C for 30 minutes to functionalize with -NCO. After incubation, the gold surface was sonicated with chloroform, and the unbound HDI molecule was removed from the surface. In the second step of rLBL, the gold substrate was incubated in 1.2 mM BPEI of chloroform at 40°C for 30 minutes. The gold surface was sonicated with chloroform and the unbound BPEI polymer was removed from the surface. In the third step of rLBL, the gold substrate was incubated in chloroform 3.4 mM PE solution for 30 minutes at room temperature. The gold surface was rinsed by sonication with chloroform. The 6-multilayered rLBL assembly was obtained by repeating the PE and BPEI incubation steps for further layers. Branched polyethyleneimine modified with ferrocene carboxaldehyde (Fc-BPEI) to obtain a redox-active polymer was synthesized as described elsewhere.[140]

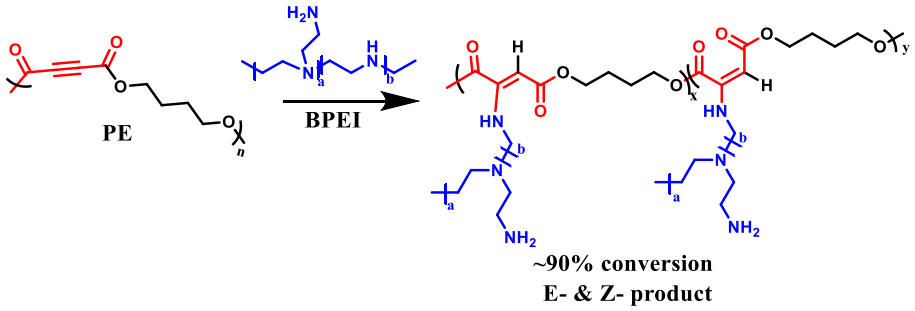

Figure 5.2 Reaction between PE and BPEI.

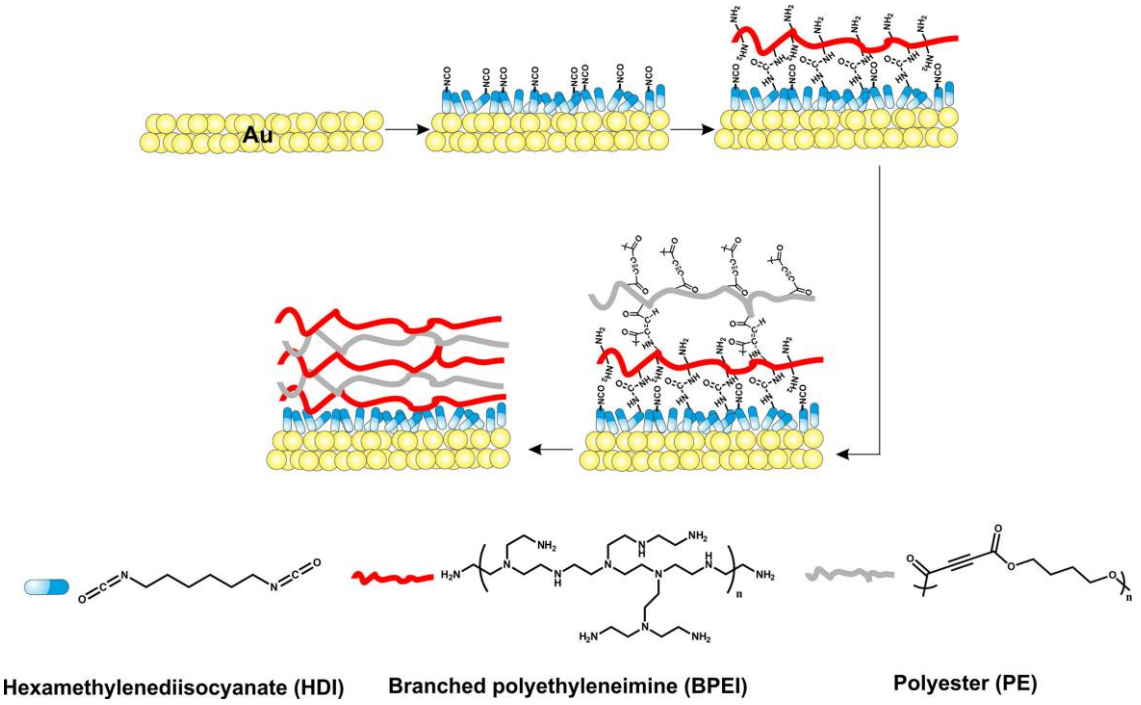

Figure 5.3 Illustration of multilayered rLBL assembly.[141]

Figure 5.3 illustrates that the nanogel structure was formed by rLBL assembly with the use of polyester (PE) with triple bonds and BPEI on an isocyanate-functionalized gold surface. In the previous chapter, it was shown that HDI interacts with the gold surface, and the gold surface is functionalized with isocyanate groups.[41] In order to obtain 6-multilayered rLBL assembly, isocyanate functionalized gold surface is incubated with BPEI. The BPEI has grafted onto the gold surface with the formation of urea groups between the amine groups and isocyanate groups. A polyester with an internal electron-deficient triple bond (PE) is incubated with the BPEI-grafted surface. The PE gives an aza-Michael addition reaction using primary amines of BPEI.[142] The reacting triple bonds form a double bond and the PE is grafted onto the gold surface within fast and high yield. The aza-Michael reaction is a nucleophilic addition reaction involving BPEI as Michael donors and electron-deficient polymer PE as Michael acceptors. E-isomers in the final structures are in the range of 89-94% in the reaction that takes place in a 90% yield (Figure 5.2).[141-143] The nanogel is formed with 6-multilayered rLBL assembly of BPEI and PE, respectively on the gold surface. After the sequential rLBL assembly, a nanogel form containing triple bonds, double bonds, and primary amine groups is obtained. Thus, a post-functionalizable nanogel form could be performed on the gold surface.

5.2. Results and Discussion

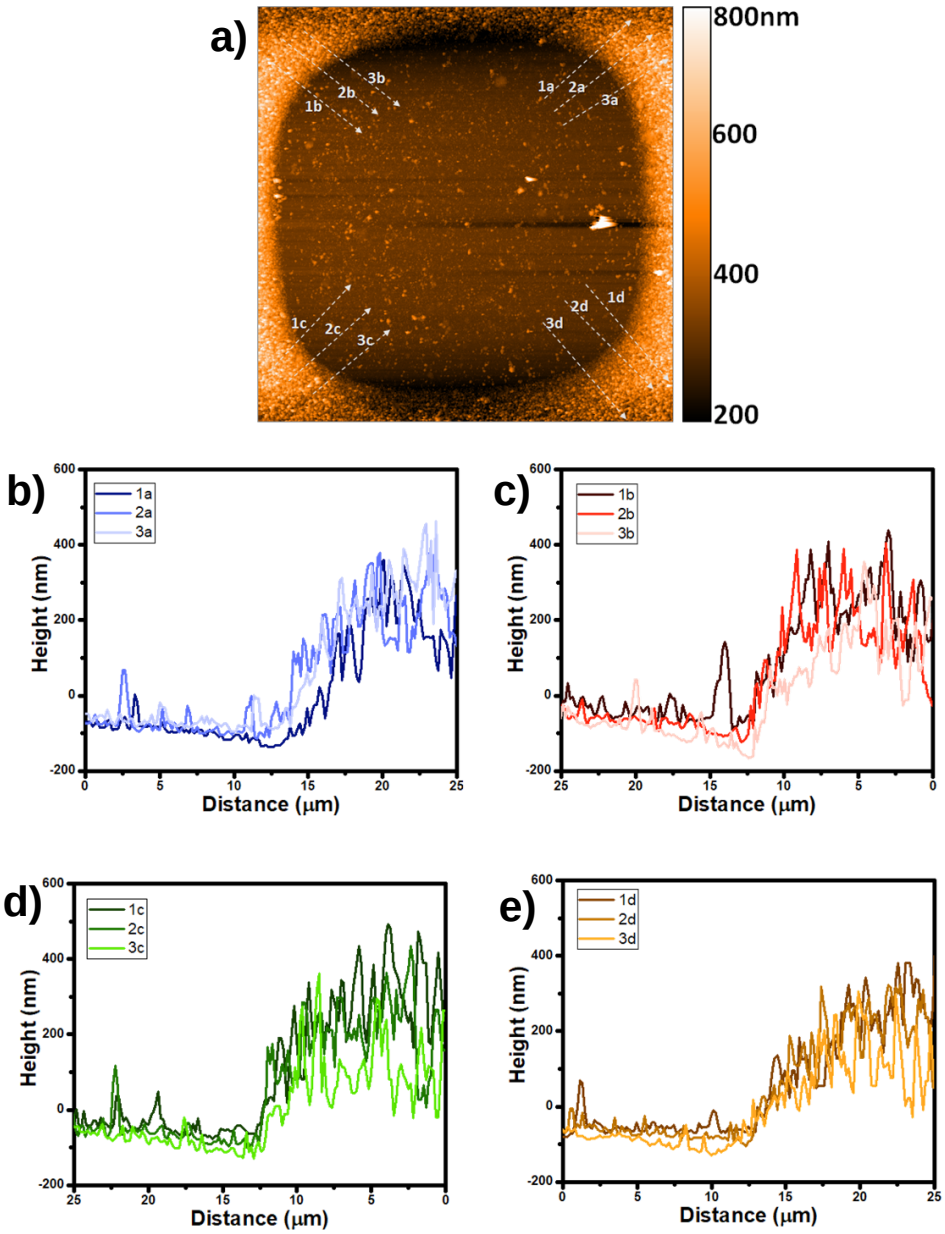

Figure 5.4 a) AFM image of the of 6-multilayered rLBL nanogel (the square region passivized). b, c, d, and e) Cross-section analysis of various region.

The gold surface is passivated with 11-mercapto-1-undecanol to discover the average height distribution of the nanogel. Figure 5.4a shows the AFM image of the nanogel formed after the rLBL assembly on the gold surface. Also, Figure 5.4a shows that the nanogel structure has a sharp square pattern after rLBL assembly. The average height is approximately 400 nm, indicating that the resulting high yield rLBL on the gold interface formed a sharp edge homogeneously. Figures 5.4b, c, and d show the cross-section of the PE-PEI of various regions of the rLBL assembly to understand deposition behavior. The average height of the formed nanogel is approximately 370 ± 60 nm. It shows that the nanogel has homogeneous height distribution; thus, PE and BPEI do not have random agglomeration behavior on the surface. This result may show that at each step of the rLBL assembly, the surface is saturated with the respective polymer and is equally functional for the next assembly.

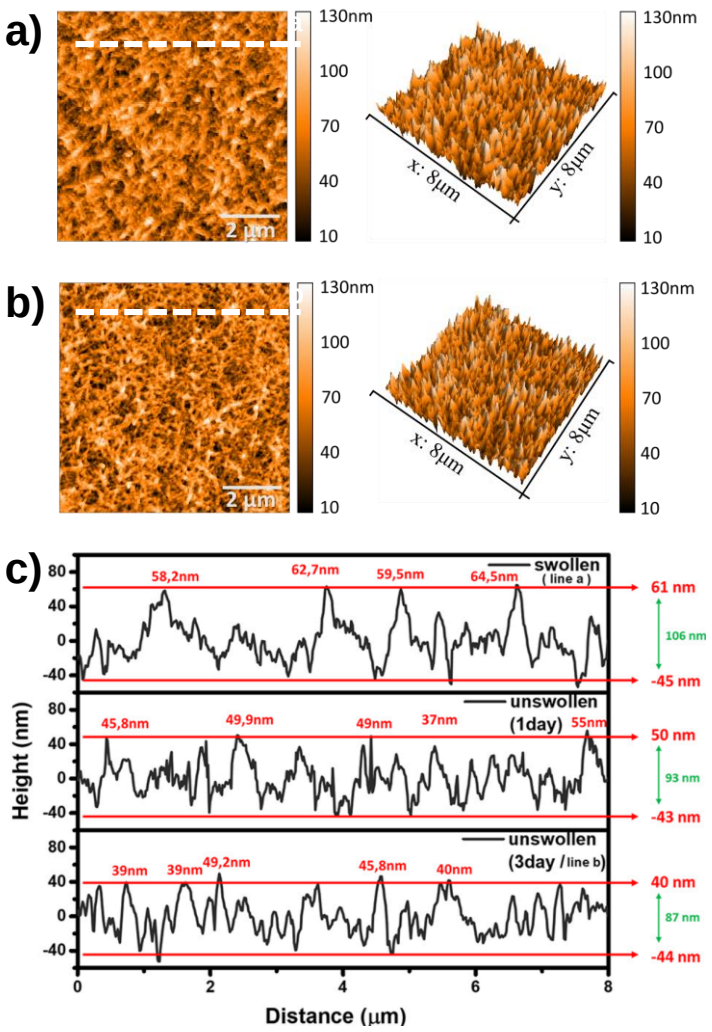

Figure 5.5 AFM height images a) shortly after rLBL (swollen) b) 3 days after rLBL (non-swollen). c) Cross-section of the swollen and unswollen surface.

The additional measurement of AFM shown in Figures 5.5a and b shows the chloroform-loaded rLBL nanogel and the chloroform-free form, respectively. The results revealed that the chloroform-loaded rLBL showed a less protruding and smoother topography than the chloroform-free form. In terms of surface area roughness of 9 μm^2, the chloroform-loaded rLBL had a roughness of 63 nm while the chloroform-free rLBL had a roughness of 74 nm. As a general view, it can be assumed that the pores that increase the roughness of the surface are formed by removing the solvent from the gel network. Therefore, the cross-section analysis shown in Figure 5.5c ensures that the number of protrusions per unit distance of rLBL films increased compared to the chloroform-loaded form between the first and third days of solvent evaporation. Also, as a result of solvent removal, the chloroform-free form of the nanogel exhibits significantly lower height profiles compared to its chloroform-loaded nanogel form. Once the solvent molecules are removed from the nanogel, the rLBL increases the roughness as a result of the collapse of the nanogel while the height decreases. These results could assume that the 6-multilayered rLBL has organogel characteristics due to the swelling behavior with chloroform. To obtain statistically reliable roughness, several cross-sectional analyses shown in Figure 5.6 demonstrate that the roughness is more distributed along the z-axis for unswollen nanogel compared to swollen. The 40x40 μm^2 area roughness of the swollen nanogel was 401.3 nm. After 3 days of solvent evaporation, the nanogel area roughness increased by around 19% of the swollen roughness and was found as a 477.2 nm. Since the area roughness was found to be 19% greater for the unswollen nanogel, it can be assumed that the area roughness increases significantly with solvent evaporation.

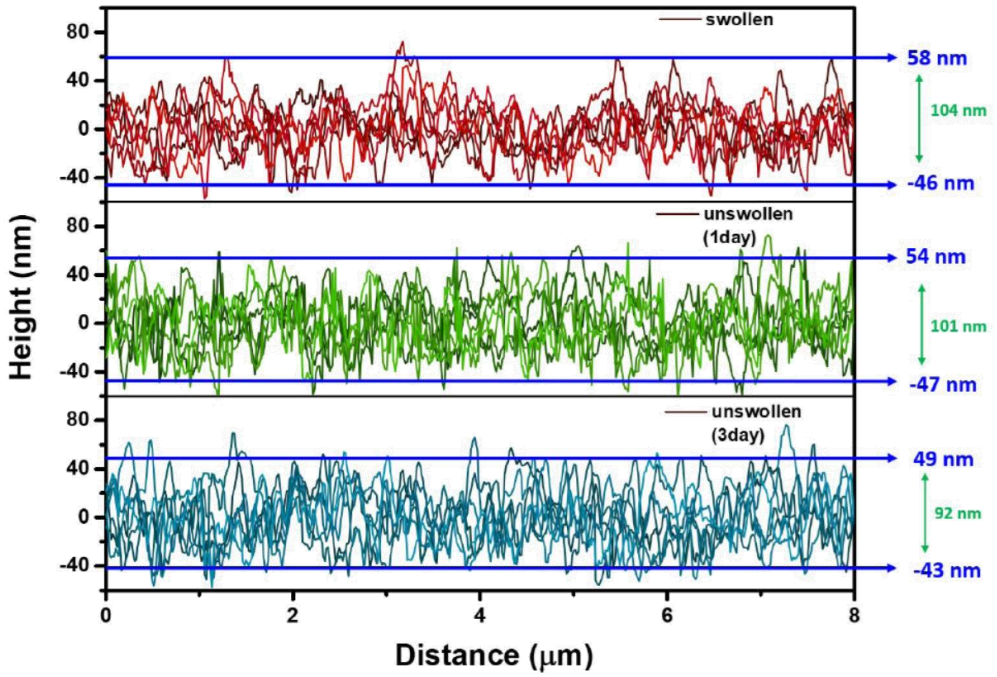

Figure 5.6 The cross-section of the swollen and unswollen sample held three days in the room conditions for air dry. After the first and third days, measurements were taken from the same regions of the sample, respectively. The rLbL nanogel surface points out the maximum and minimum point of the surface and thee average height difference.

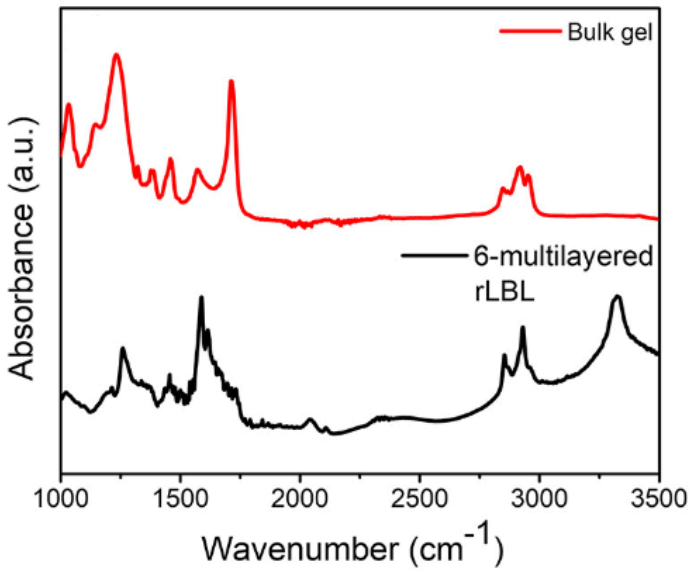

Figure 5.7 FTIR spectrum of bulk gel and the 6-multilayered rLBL coated gold surface.

Figure 5.7 shows the FTIR spectrum of bulk gel and the 6-multilayered rLBL coated gold surface. The alkyne chain triple bond (C≡C) stretching is observed at 2046 cm^{-1} and 2112 cm^{-1}; however, the (C≡C) stretching is absent in the bulk gel spectrum. This result indicates that the reaction takes place in high yield between polymer chains in the bulk gel synthesis. On the contrary, in the rLBL that occurs on the gold surface, the polymer is grafting to the surface, and it could be assumed that the polymer motion is restricted. Therefore, results indicate that the 6-multilayered rLBL has triple bonds that provide post-functionalization. Both the bulk gel and the 6-multilayered rLBL show C-O-C asymmetrical stretching, and symmetrical stretching occurs at 1261 cm^{-1} and 1023 cm^{-1}, respectively. Also, the absorption band at 1588 cm^{-1} assigned to the N-H bending of amines and N-H stretching appears at 3332 cm^{-1}.[76]

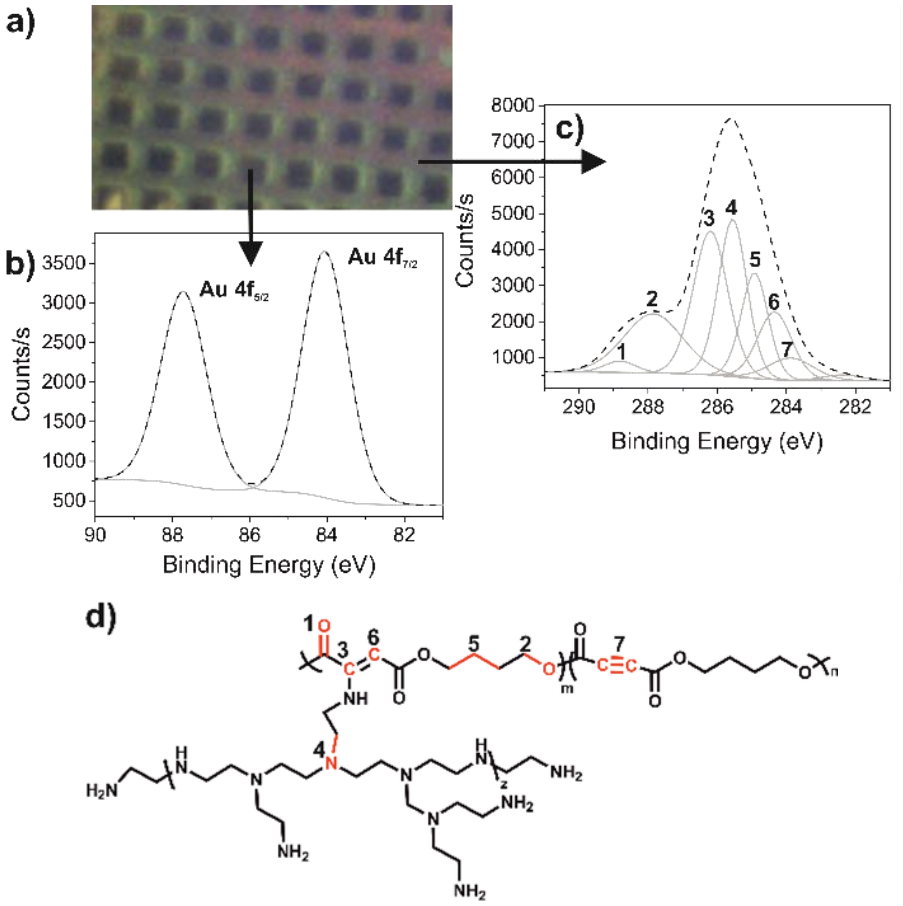

Figure 5.8 a) Light microscope image. b) XPS spectra of c) Au 4f and C 1s. d) Chemical group representation corresponding to the XPS spectra of Figure 5.8c.[141]

The microscope image of the patterned PE-PEI gel obtained with 6-multilayered rLBL is shown in Figure 5.8a. Black arrows indicate the polymer and gold regions where the XPS point analyses have been carried out. Figure 5.8b shows the XPS spectra of Au 4f corresponding to the Au 4f5/2 peak at 87.71 eV and the Au 4f7/2 peak at 84.08 eV.The C 1s spectrum of the 6-multilayered rLBL shown in Figure 5.8c is fitted into seven peaks. The binding peaks at 288.43 eV (FWHM: 1.57) and 287.61 eV (FWHM: 1.14) can be attributed to the C=O (1) PE and C-O (2). The binding energy of 286.26 eV is the major peak corresponding to the reaction between PE and BPEI on the gold surface. González-Torres et al. described the structure of a possible union of three pyrroles Py and ethylene glycol EG molecules at 286.39 eV that indicated a C=CN-C bond, which are the bonds of Py-Py.[144] The bond formed as a result of the reaction between PE and PEI could be assumed similar to the polypyrroles.[145, 146] Thus, the binding energy of C=C-N-C (3) can be defined as 286.26 eV (FWHM: 1.39). The peaks found at 284.08 eV (FWHM: 0.92) and 285.49 eV (FWHM: 1.18) can be attributed to the groups C = CH-C (6) and C-N (4).[47] Also, the binding energy peak of the C-N bond resulting solely from the presence of BPEI is remarkable. The binding energies at 284.77 eV (FWHM: 1.01) and 283.33 eV (FWHM: 0.79) correspond to C≡C (7) triple bonds and C-C (5) aliphatic carbons.[147] These XPS point analysis results demonstrate that rLBL assembly is formed by reacting BPEI and PE polymers on the gold surface. The binding energy area of the C=CN–C bond at 286.26 eV and the C≡C triple bond at 283.33 eV corresponds to reacted PE and free PE C≡C triple bond, respectively.

The ratio of the sum of the binding energy area values of 283.33 eV and 286.26 eV (from the top to 400 nm etch depth) reveals that 86% of the carbon triple bonds of PE reacted with BPEI while 14% unreacted. It can be assumed that the reaction, which takes place in the solution with a yield above 90%, is coated on the surface with high efficiency.[141, 142]

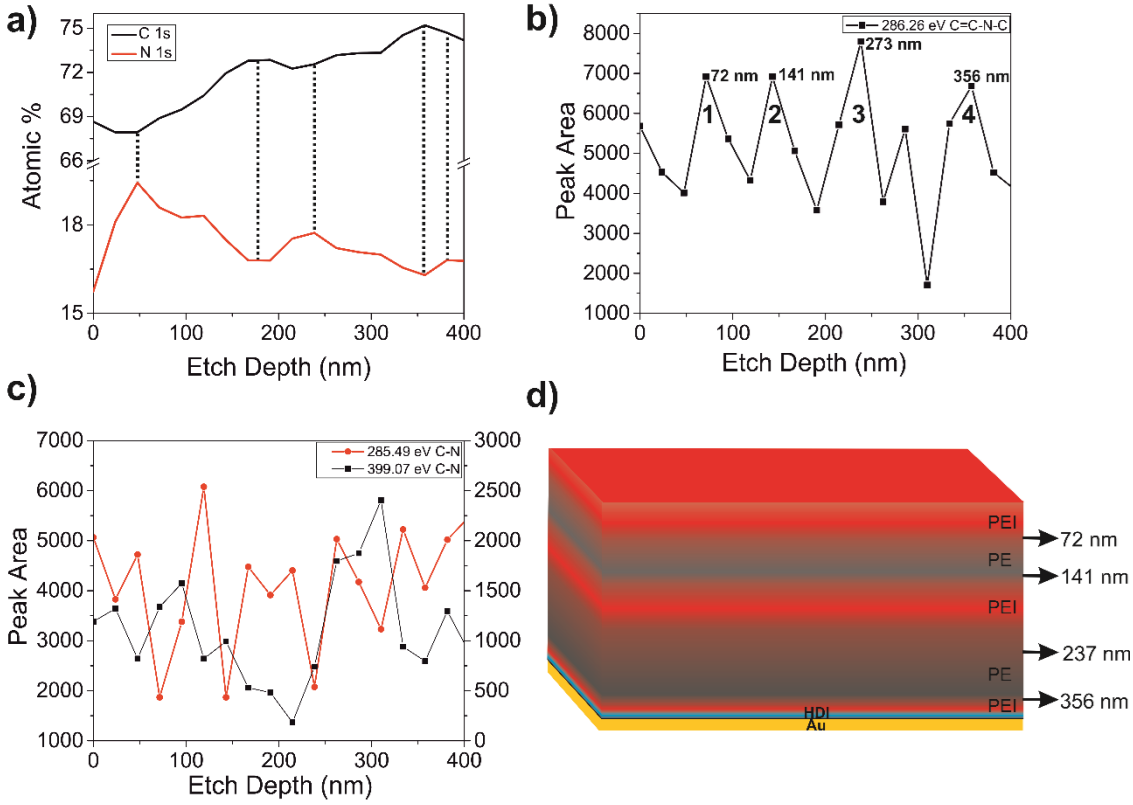

Figure 5.9 a) Atomic percentage of carbon and nitrogen on the gold surface and etching depth versus peak area of b) C=C-N-C and c) C-N and C-N. d) Illustration of XPS depth profiling results of rLBL assembly.

XPS depth profiling analysis is a significant method used to disclose the inner composition of layer-by-layer films.[148-150] Taketa et al. has revealed nano-structured coatings of PSS / CHI and CMC / CHI (sodium polystyrene sulfonate (PSS), chitosan (CHI), and carboxymethylcellulose (CMC)) electrostatic interactions as model systems on a silicon substrate with depth profile XPS analysis.[151] The study reported that the inner composition of LBL films is well-defined in terms of thickness/cycle (nm) for the ratio of polymer. Thus, XPS depth profiling analysis was carried out to reveal the average thickness of the 6-multilayered rLBL assembly. Figure 5.9a shows the change in atomic percentage of carbon and nitrogen values with increasing depth. There are two semicircle-like, slightly upward slopes in the carbon percentage and two semicircular-like slightly downward slopes in the nitrogen percentage change. With the change of nitrogen percentage, BPEI corresponding to the topmost layer can be related to the first peak at 48 nm. After the first peak, an increase in the carbon percentage is monitored while the nitrogen percentage decreases. The first peak of the percentage carbon, which can also be

assigned with the fifth layer, is 173 nm, and the corresponding percentage of nitrogen has a relatively low value. The peak of the percentage of nitrogen at 238 nm and the percentage of carbon at 350 nm can be related to the fourth and third layers. Also, the peak at 390 nm of the nitrogen percentage can be associated with the second layer. A binding energy corresponding to 286.36 eV belongs to the C = C-N-C bond formed by the reaction of PE and BPEI. Figure 5.9b demonstrates the etching depth corresponding to the peak area at 286.36 eV. In Figure 5.9b, the densest bond between PE and BPEI could point out peaks at 72 nm, 141 nm, 237 nm, and 356 nm, respectively, and can indicate the transition point between polymers. BPEI has a low thickness in the second layer, while PE has a relatively high thickness in the third layer. The reason for the thin layer in BPEI in the second layer may be attributed to the density of the NCO functional group formed in the first layer, which is less than the density of the NH_2 functional group ratio in BPEI. Thickness values of 237 nm, 141 nm, and 72 nm stand out as almost equal thickness values in the following layers, indicating that the polymers were uniformly grafted. Figure 5.9c demonstrates the peak areas with parallel increase and decrease correlations of the 285.49 eV (C-N) and 399.07 eV (C-N) binding energies related to the etching depth. Figure 5.9d illustrates the scheme of the XPS depth profile analysis depicted according to the C=C-N-C peak (thickness) values in Figure 5.9b. As a result, layers with densified regions in terms of PE and BPEI polymers are obtained, as well as a mixed inner composition of the 6-multilayered rLBL films containing more or less two polymers in each layer.

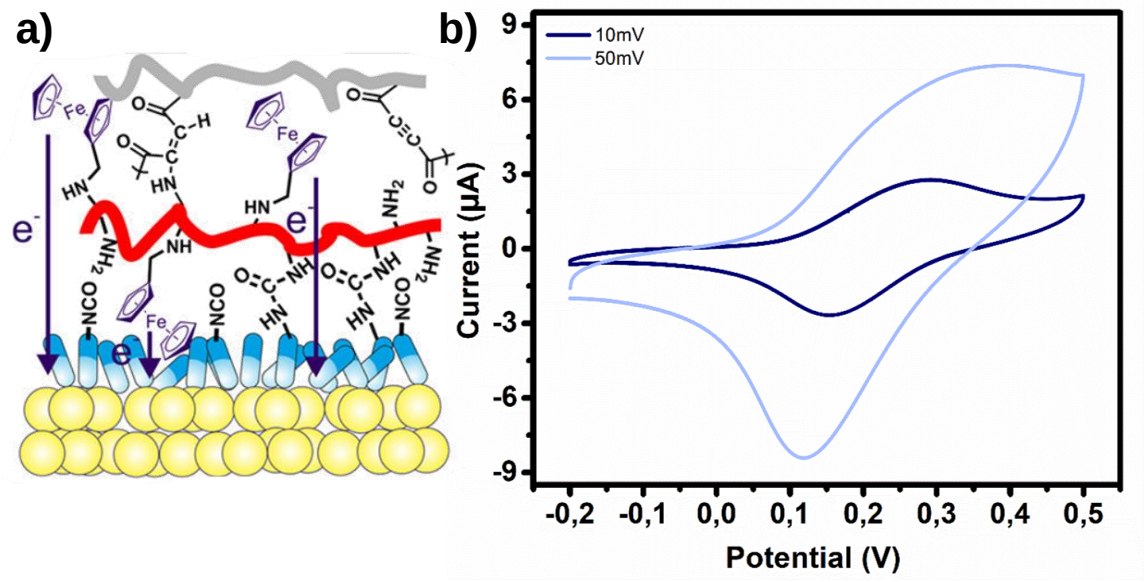

Figure 5.10 a) Scheme of Fc-BPEI rLBL. b) The cyclic voltammogram of six-multilayered rLBL gold electrode (with ferrocene carboxyaldehyde (Fc) modified BPEI), at 10 and 50 mV/s scan rate in 0.01M PBS buffer which did not include $Fe_4(CN)_6$ as a redox. Buffer solution pH is 7.

The BPEI backbones were modified with ferrocene carboxaldehyde to obtain a redox-active polymer. The high amine density of BPEI allows pre-functionalization with Fc and then could be utilized for rLBL assembly (Figure 5.10a). Figure 5.10b shows a cyclic voltammogram that the electroactivity of the ferrocene anchored rLBL without any free redox couple as a mediator in the electrolyte solution. The current density and the peak separation are decreased with the decrease of the scan rate. Also, the distinct anodic and cathodic currents observed at the low scan rate indicate a slow electron transfer. The anodic peak current is 2.6 μA and the cathodic peak current is 1.5 μA for scan rate 10mV/s.

5.3. Conclusion

In *Chapter 2*, a surface polymerization owing to the strong interaction (~ 900 meV) of the isocyanate functional group with the gold surface was described. This chapter presents the aza-Michael addition reaction of PE and BPEI to form rLBL film on an isocyanate functionalized gold surface. The soft nanogel fabricated with the rLBL methodology could potentially present three advantages over traditional methods:

(i) As mentioned in *Chapter 2*, the incubation of diisocyanate is a fast (less than 30 minutes for modification) and powerful modification methodology compare to gold-thiol chemistry.

(ii) Most LBL films are obtained on the surface by solvent exclusion, while the method defined presents a gel coat that promotes electron and mass transfer towards the electrode.

(iii) Presented rLBL method has the possibility of pre- or post-modification of the gel coat. It can be easily achieved to respond quickly to many analytes through rapid electron and ion movement.

A homogeneous and well-defined, patterned nanogel coat on the gold substrate is formed, and the 6-multilayered rLBL gel has a thickness profile of 400 nm that is characterized by utilizing AFM. rLBL films exhibit an organogel-like behavior with solvent-related swelling and shrinkage features on the gold substrate. This feature could ensure openings in the mesh structure that readily permit the transfer of matter and charge by maintaining the distance between the reacting multiple layers. The XPS point analysis of rLBL films confirms that the layers are composed of covalently reacting groups, and FTIR spectra confirm unreacted functional primary amine groups (NH_2) and carbon-carbon triple bonds. The XPS depth profiling analysis reveals the inner composition of layer-by-layer films that determine the average thickness of the 6-multilayered rLBL. These layers have dense regions in terms of PE and BPEI polymers, as well as a mixed composition of each individual layer containing both polymers. 6-multilayered rLBL contains the promising potential for nanogel soft biointerface applications with post-functionalizable groups.

CHAPTER 6

MICRO-PATTERNING OF HYDROGEL BY LASER ABLATION FOR CELL GUIDANCE

Surface modification is to bring physical, chemical, or biological properties that are different from the original properties of the interface properties. In this way, we can tailor the interface properties with improved biocompatibility, surface roughness, hydrophilicity, and surface charge. The surface modification with hydrogel-based soft materials like gelatine is proper for creating 3D biomaterials, which can be used in tissue engineering applications in terms of cell adhesion, low immunogenicity, biocompatibility, and low cost. The interaction of the cell with the surface is related to the boundaries of micro-scale structures of various domains that harmonize with the arrangement of the cells.[4, 152]

Lithographic technologies fabricate patterns on surfaces and create different chemical and physical domains that provide control of the interaction between the cell and the surface, thereby controlling the cell behavior for proliferation, differentiation, and adhesive ability. The laser ablation method, which is a fabricating pattern in terms of rapid, straightforward, and high reproducibility is the process of vaporization or sublimation of the material from a substrate by a laser beam.[153, 154] The effect of cell guidance was investigated on micro-patterned hydrogel regions with different chemical and physical domains on glass surfaces using the laser ablation method. In addition, use of bioactive glass coating is widely used for the improvement of biocompatibility of implants in bone tissue engineering applications.[155]

This chapter covers the utilization of a rapid and straightforward laser ablation method to form a micro-patterned hydrogel film on the glass surface for cell guidance. As a model hydrogel, the gelatin methacryloyl (GelMA) was cured on the glass surface, and optimum laser ablation parameters were determined. By using laser ablation, we removed the gel from the surface, and cell culture studies were performed by fabricating various micro-patterned GelMa on glass surfaces.

6.1 Materials and Methods

All chemicals were purchased from Sigma-Aldrich and used without further purification. The Gelatin methacryloyl hydrogel (GelMA) was synthesized as described elsewhere.[156] GelMa was characterized using PerkinElmer Spectrum 100 FTIR with an attenuated total reflection apparatus. The synthesized GelMa (36 mg) was dissolved in 800 µl water containing 1% Irgacure 2959. Glass surfaces were cleaned with standard cleaning (RCA cleaning) and removed from organic impurities. The solution was dropped onto the glass surface to form a meniscus (~125 µl) and photopolymerization was carried out in the UV cabinet (365 nm) for 7 minutes. GelMA was dried for one day at room temperature, and the laser ablation procedure was performed by using CO_2 laser ablation. In order to examine the power parameter effect of laser ablation on the gel, the power value was set from 3 to 5 while the speed was 60, and the power value was set to 4 while the speed value ranged from 45 to 75. SEM images were obtained on the edge of the glass by using a Quanta 250 FEG Scanning Electron Microscope.

Cell culture studies were performed with the NIH 3T3 mouse fibroblast cell line. This cell line was chosen due to how easily the cells grow in a culture medium and the immortalized cell line. The cells were pre-cultured in Dulbecco's Modified Eagle's Medium (DMEM), supplemented with 10% Fetal Bovine Serum (FBS), 1% penicillin-streptomycin in an incubator at 37°C, and 5% CO_2 humidified atmosphere for two to three days. Before cell-seeding, hydrogel patterned glass surfaces (n=3, size: 1x1 cm^2) were disinfected under UV exposure for 30 minutes. Then, glass surfaces were placed in the 12 well plate and conditioned with a culture medium for 3 hours. Following the trypsinization, cells were removed on the culture flask and counted, then seeded as $5x10^4$ cells/well on the hydrogel patterned glass surfaces and cultured in DMEM supplemented with 10% FBS, 1% penicillin-streptomycin in an incubator at 37°C, and 5% CO_2 humidified atmosphere for 24 hours. To assess the cell viability, Live/Dead (AAT Bioquest) assay was used. CytoCalcein™ Green and Propidium Iodide (PI) were added to the buffer solution in equal amounts, then transferred onto the samples. After 30 minutes of incubation at 37°C, the viability of the cells was observed by using a fluorescence microscope (Zeiss Axio Observer), visualizing live (green) and dead (red) cells on the glass surfaces.

6.2. Results and Discussion

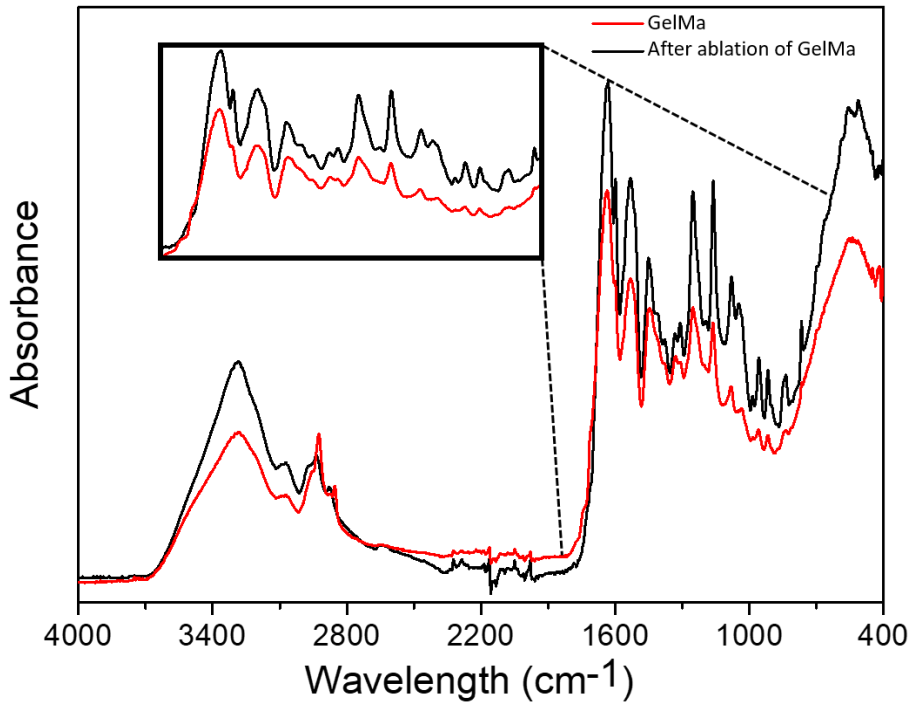

Figure 6.1. Comparison of FTIR spectra of GelMa and after laser ablation of GelMa on glass surface.

Figure 6.1 shows the FTIR spectra of GelMa and after laser ablation of GelMa on the glass surface. FTIR spectra of GelMa has broadband centered at 545 cm^{-1} could be attributed to the Si-O-Si bending vibration of the glass surface. Amide I, amide II, and amide III bands correspond at 1632, 1530, and 1250 cm^{-1} respectively. The signal at 3285 cm^{-1} is represented for O-H stretching of hydrogen-bonded hydroxyl groups and N-H stretching vibration coupled with hydrogen-bonding. Two peaks 2878 and 2934 cm^{-1} are attributed to the symmetric and asymmetric stretching modes of CH_2 groups, respectively. After laser ablation, the absorbance of all peaks was reduced due to the decrease in the amount of GelMa. Notably, the two peaks around 2878 cm^{-1} and 2934 cm^{-1} shifted to 2854 and 2925 cm^{-1} that could be assumed for well-ordered alkyl chains after ablation of GelMa.[30, 76]

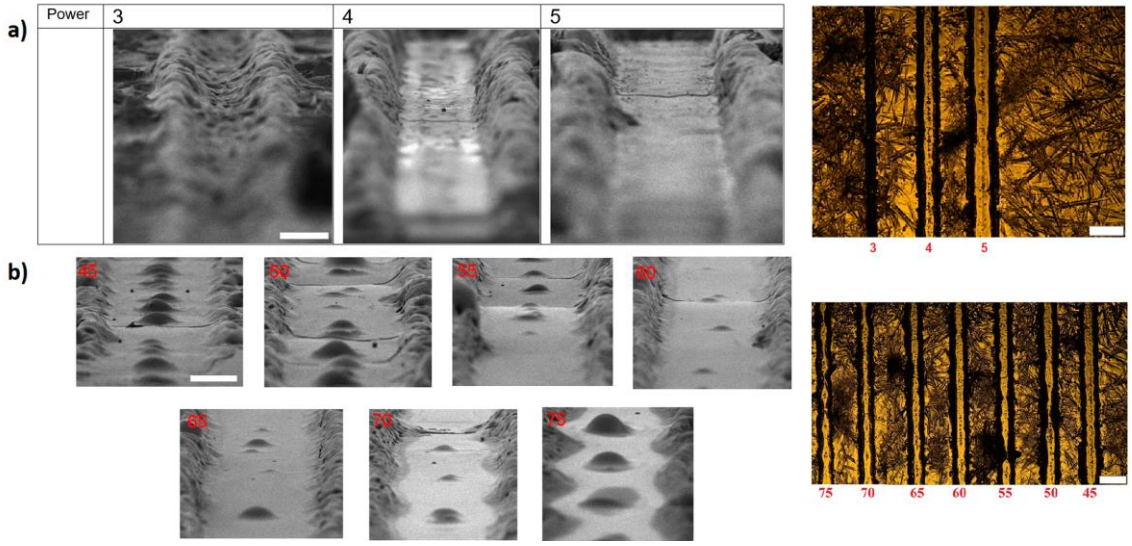

Figure 6.2. SEM image after laser ablation of the GelMa on the glass surface and light microscope images with (scale bar: 500 µm) a) speed: set 60, power values between 3 to 5 (scale bar: 50 µm) b) power: set 4, speed values between 45 to 75 (scale bar: 50 µm).

RCA cleaning forms hydroxyl and hydroxylate groups on the glass surface, which enhance the hydrophilic property.[157] Thus, a homogeneous hydrogel layer is obtained with secondary interactions like hydrogen bonds between the hydrophilic glass surface and GelMa, which has NH_2 and OH groups. Therefore, the GelMa retained form for a long time in the cell culture medium without chemically bonding on the glass surface. In addition, hydrogen bonding capable groups (NH_2 and OH) on the GelMa backbone interact with water and give a high yield swelling capacity.[156]

Figure 6.2 shows the SEM and microscope images of laser ablation after the drying of GelMa on the glass surface. The power value 3 formed a half-cylinder gel structure (diameter ~60 µm); therefore, gel residues have existed on the glass surface. The laser power values 4 and 5 swept up gel material and formed a straight line of 130 and 180 µm width, respectively (Figure 6.2a). In order to examine the effect of the speed parameter, the power value was set to 4, and the speed value was scanned between 45 and 75. The power values 45, 50, and 55 give a yield of a circular island-like structure in the middle of the wavy line. The power values 70 and 75 gave rise to a lower number of circular island-like structures in the middle of the wavy line compared to the power values 45 and 50. On the contrary, the homogeneous straight line with identical width was obtained with speed values 60 and 65 (Figure 6.2b). SEM and microscope image results

showed that by utilizing a rapid and straightforward laser ablation method, the gel material was removed from the glass surface with speed and power values of 60 and 4, respectively.

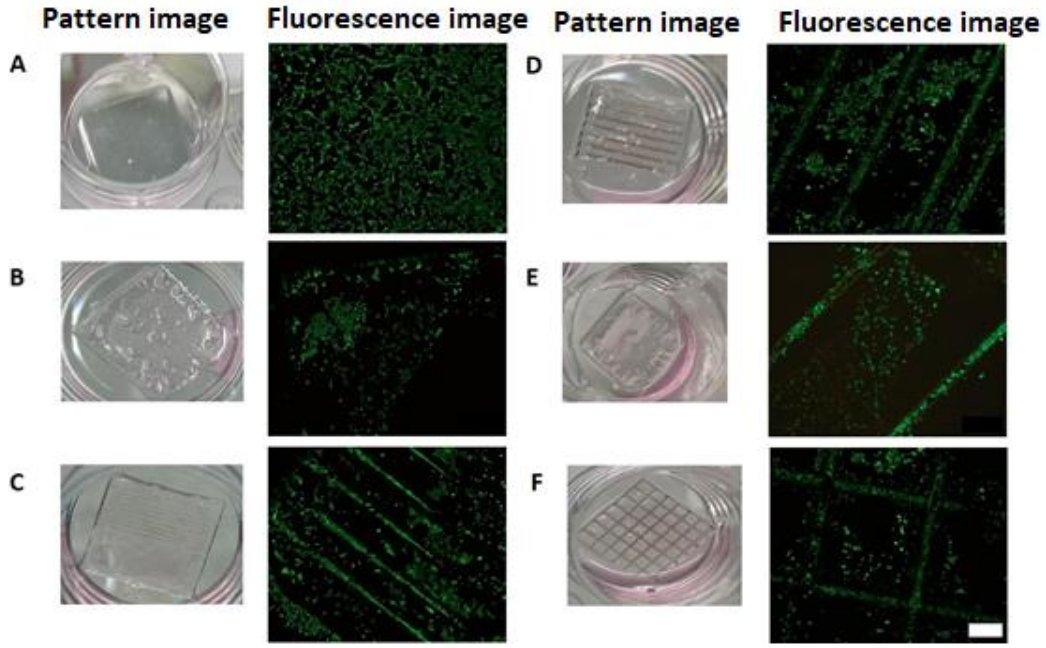

Figure 6.3. Investigation of the viability of NIH 3T3 cells seeded on hydrogel-patterned glass surfaces using the live-dead method, scale bar: 200µm. a) Control: Glass and cell. b) Glass, hydrogel, and cell. c) Glass, hydrogel pattern 1, and cell. d) Glass, hydrogel pattern 2, and cell. e) Glass, hydrogel pattern 3, and cell. f) Glass, hydrogel pattern 4, and cell.

Figure 6.3 depicts Live/Dead assay results. Fluorescence microscopy images display the live (green) and dead (red) cells on the hydrogel patterned glass surfaces. The cells were attached and covered on whole bare glass surfaces, and it was observed that cell viability was high (Figure 6.3a). Besides, cells were attached on the untreated hydrogel surface without any cavity; however, cell attachment and viability were lower than the glass surface (Figure 6.3b). To assess the cell adhesion and migration, various patterns were created on the hydrogel surface. In pattern 1, cells were attached both on the hydrogel area and hydrogel-free cavity obtained by laser ablation (Figure 6.3c). In pattern 2, which was composed of the double-sized hydrogel-free cavity, cells were attached mostly on the hydrogel-free cavity compared to pattern 1 (Figure 6.3d). In the higher size of the cavity, pattern 3, cells were attached and arranged more regularly in the

hydrogel-free cavity (Figure 6.3e). In pattern 4, the viable cells were seen in the hydrogel-free area, and viability was higher compared to the hydrogel surface (Figure 6.3f). Moreover, the cage-like surface provided an organization of the cells, which confirmed that various patterns were affected by the cell adhesion.

6.3. Conclusion

In this chapter, micro-patterned hydrogel film on the glass surface was evaluated for cell guidance by the laser ablation method. Gelma was removed from the surface and cell attachment and arrangement were observed on the various micro-patterned GelMa on glass surfaces. It was observed that cells were attached and proliferate on the hydrogel-free cavities produced by the laser ablation method.

Barbucci et al. obtained a micro-patterned glass surface based on a striped pattern of hyaluronic acid and its sulfated derivative using laser ablation technique. The micro-patterned surfaces were seeded with mouse fibroblasts (3T3) and bovine aortic endothelial cells (BAEC) and assessed in terms of cellular adhesion, proliferation, and orientation. They reported that cell behavior is related to the surface modification; both 3T3s and BAECs adhered and lined up on the sulfated derivative surface, which confirmed that hyaluronan is not a suitable substrate for cell adhesion. On the contrary, the cells spread and demonstrate good cell adhesion on the sulfated hyaluronic acid.[153]

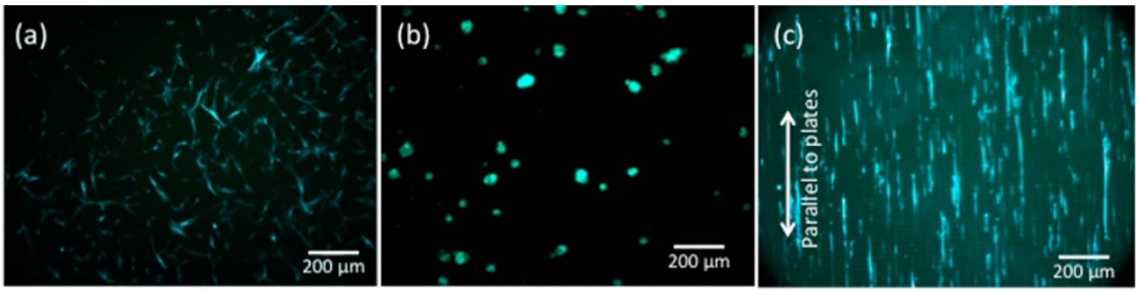

Figure 6.4. Adhere and spread of HMSCs a) on Petri-dish, b) on flat pHEMA hydrogel substrate, and c) elongate and align on patterned pHEMA hydrogel substrate.

Hu et al. evaluated the cell orientation on micro-patterned topography produced by poly(2-hydroxyethyl methacrylate) (pHEMA) hydrogel. It has been shown that the surface can effectively guide the orientation and morphology of human mesenchymal

stem cells (HMSCs) (Figure 6.4). In accordance with our study, the hydrogel patterned surfaces provide a tunable cellular arrangement.[158] In another study, with an alternative approach on ablasion, Janhavi et al. fabricated micro-channels on Polycaprolactone (PCL)-Chitosan (CH) nanofiber layered bovine pericardium scaffold by using nanosecond laser to enhanced cellular adhesion and migration. The decellularized pericardium was used as a biological layer and PCL, CH nanofibrous were electrospun on the decellularized layer, then laser ablation was applied on the surface to obtain microchannels. The cells seeded on the microchannels exhibited increased cellular adhesion comparison to non-ablated surfaces. This study suggested that the feasibility to selectively ablate the polymer layer in the scaffolds and also describes a new approach to enhance cellular infiltration.[159]

CHAPTER 7

OVERALL CONCLUSIONS

As an overall consideration, interface engineering is combined with metals or semiconductors, which are electronic components of bioelectronic systems, to create a soft and stimulus-sensitive interface that achieves the delicate balance between bio and electronic components. In this thesis, an isocyanate functionalized gold surface is probed with surface modification methodologies like *grafting to*, *grafting from*, and *reactive layer-by-layer assembly*, which do not require inert conditions, degassing, or high-cost catalysts.

XPS point analysis results and theoretical calculations of the adsorption of HDI molecules on the Au (111) show that one isocyanate of HDI molecule interacts with the gold surface. XPS C 1s point spectra demonstrate binding energy peaks of the main urethane bonds as C-O, C-N, NCOOM, and unreacted NCO. The theoretical calculation and favorable configuration are that an N atom of the NCO group is horizontally aligned to the gold surface while the aliphatic chain is perpendicular to the surface. The binding energy between the N atom and the top-site of the Au (990 meV) is much higher than the Van der Waals type interaction (35 meV) energy, while the binding energy is lower than the Au-S (1700 meV) bond. As a result of XPS point analysis results and theoretical calculations of the HDI-gold surface interaction, one isocyanate interacts with gold while the other isocyanate remains for further reaction. Thus, both surface modifications and unreacted isocyanate groups have been formed on the gold surface, which enabled the formation of polymeric structures with further reactions.

Unreacted isocyanate gives a yield 70 nm-thick nanoporous PU interface on a gold substrate by sequential incubation of 1,4-BDO and HDI via surface-assisted (SurfAst) urethane polymerization. On the other hand, PDI-1,4-BDO result in rod-like structures while IPDI-1,4-BDO couldn't form a PU interface on the gold surface. In addition, XPS chemical mapping results show that for a high yield PU interface a minimum of six steps should be applied. Furthermore, VeeMax III results show that a PU interface orientation of approximately 90° with respect to the surface and carbon chain packing as the self-assembled monolayers. This orientation may arise from the highly mixed hydrogen bonding between the nanoporous PU chains that increase secondary

interaction energy per unit length on the surface. A nanoporous PU structure could be performed with a post-functionalization of PEG to obtain antifouling properties and PEG post-functionalization reduced protein adhesion by approximately tenfold. Also, CV result shows PU interface with a peak current value of 11 μA.

For further investigation, SurfAst urethane polymerization is applied to 11-mercaptoundecanoic acid incubated to post-functionalize with poly(N-allyl-N-methyl-N-(3-((4-methylthiophen-3-yl)oxy)propyl)prop-2-en-1-aminium bromide (PT) nanowire on the gold surface. The nanowire PT structure has dense centers with an average height of 100 nm and fibers with ~250 nm width and ~7μm length. Since the phase shift values of surfaces containing cationic PT nanowires are similar and higher than 3.20°, the phase shift value could be considered as an alternative and complement characterization technique of *grafting to* PT nanowires on the gold surface by using EFM.

In the following study, the isocyanate functional gold surface is utilized to obtain a soft nanogel fabrication with the *reactive layer-by-layer* methodology and the Aza-Michael addition reaction of PE and BPEI. The nanogel coat on the gold substrate is formed with 6-multilayered rLBL that has a 400 nm thickness. In addition, the BPEI is pre-functionalized with ferrocene carboxaldehyde to obtain a redox-active polymer and the CV result shows the anodic peak current is 2.6 μA and the cathodic peak current is 1.5 μA for scan rate 10mV/s. In the last part of the thesis, the use of the laser ablation method to create a micro-patterned hydrogel film for cell guidance on a glass surface is presented as a brief study.

In summary, the stimulus-sensitive interface with well-defined alternative interface studies is a contemporary study area that needs to be more heavily researched because it is constantly growing. The production of soft materials on solid surfaces is presented with novel, simple, and straightforward methods. The production process, structures, and comprehensive characterization of the soft materials obtained on the surfaces are discussed. Consequently, our greatest ambition is for this thesis study to serve as a source and guide for alternative interface research.

REFERENCES

1. Asri, R. I. M.; Harun, W. S. W.; Samykano, M.; Lah, N. A. C.; Ghani, S. A. C.; Tarlochan, F.; Raza, M. R., Corrosion and surface modification on biocompatible metals: A review. *Materials Science and Engineering: C* **2017,** *77*, 1261-1274.

2. Mozetič, M., Surface Modification to Improve Properties of Materials. *Materials (Basel)* **2019,** *12* (3), 441.

3. Love, J. C.; Estroff, L. A.; Kriebel, J. K.; Nuzzo, R. G.; Whitesides, G. M., Self-assembled monolayers of thiolates on metals as a form of nanotechnology. *Chemical reviews* **2005,** *105* (4), 1103-1170.

4. Fabbri, P.; Messori, M., Surface modification of polymers: chemical, physical, and biological routes. In *Modification of Polymer Properties*, Elsevier: 2017; pp 109-130.

5. Chang, R.; Asatyas, S.; Lkhamsuren, G.; Hirohara, M.; Mondarte, E. A. Q.; Suthiwanich, K.; Sekine, T.; Hayashi, T., Water near bioinert self-assembled monolayers. *Polymer Journal* **2018,** *50* (8), 563-571.

6. Clifford, T. J., The Effect of Alkyl Chain Parity on the In Situ Covalent Modification of Carboxy Terminated Alkane Thiol SAMs. **2007**.

7. Colangelo, E.; Comenge, J.; Paramelle, D.; Volk, M.; Chen, Q.; Lévy, R., Characterizing Self-Assembled Monolayers on Gold Nanoparticles. *Bioconjugate Chemistry* **2017,** *28* (1), 11-22.

8. Porter, M. D.; Bright, T. B.; Allara, D. L.; Chidsey, C. E. D., Spontaneously organized molecular assemblies. 4. Structural characterization of n-alkyl thiol monolayers on gold by optical ellipsometry, infrared spectroscopy, and electrochemistry. *Journal of the American Chemical Society* **1987,** *109* (12), 3559-3568.

9. Hui, C. M.; Pietrasik, J.; Schmitt, M.; Mahoney, C.; Choi, J.; Bockstaller, M. R.; Matyjaszewski, K., Surface-Initiated Polymerization as an Enabling Tool for Multifunctional (Nano-)Engineered Hybrid Materials. *Chemistry of Materials* **2014,** *26* (1), 745-762.

10. Zhao, B.; Brittain, W. J., Polymer brushes: surface-immobilized macromolecules. *Progress in Polymer Science* **2000,** *25* (5), 677-710.

11. Zoppe, J. O.; Ataman, N. C.; Mocny, P.; Wang, J.; Moraes, J.; Klok, H.-A., Surface-Initiated Controlled Radical Polymerization: State-of-the-Art, Opportunities, and Challenges in Surface and Interface Engineering with Polymer Brushes. *Chemical Reviews* **2017,** *117* (3), 1105-1318.

12. Wang, S.; Wang, Z.; Li, J.; Li, L.; Hu, W., Surface-grafting polymers: from chemistry to organic electronics. *Materials Chemistry Frontiers* **2020,** *4* (3), 692-714.

13. Banerjee, S.; Paira, T. K.; Mandal, T. K., Surface confined atom transfer radical polymerization: access to custom library of polymer-based hybrid materials for speciality applications. *Polymer Chemistry* **2014,** *5* (14), 4153-4167.

14. Matyjaszewski, K., Atom Transfer Radical Polymerization (ATRP): Current Status and Future Perspectives. *Macromolecules* **2012,** *45* (10), 4015-4039.

15. Matyjaszewski, K.; Xia, J., Atom Transfer Radical Polymerization. *Chemical Reviews* **2001,** *101* (9), 2921-2990.

16. Jakubowski, W.; Min, K.; Matyjaszewski, K., Activators Regenerated by Electron Transfer for Atom Transfer Radical Polymerization of Styrene. *Macromolecules* **2006,** *39* (1), 39-45.

17. Kim, J. Y.; Lee, B. S.; Choi, J.; Kim, B. J.; Choi, J. Y.; Kang, S. M.; Yang, S. H.; Choi, I. S., Cytocompatible Polymer Grafting from Individual Living Cells by Atom-Transfer Radical Polymerization. *Angewandte Chemie (International ed. in English)* **2016,** *55* (49), 15306-15309.

18. Paterson, S. M.; Brown, D. H.; Chirila, T. V.; Keen, I.; Whittaker, A. K.; Baker, M. V., The synthesis of water-soluble PHEMA via ARGET ATRP in protic media. *Journal of Polymer Science Part A: Polymer Chemistry* **2010,** *48* (18), 4084-4092.

19. Tsarevsky, N. V.; Matyjaszewski, K., "Green" Atom Transfer Radical Polymerization: From Process Design to Preparation of Well-Defined Environmentally Friendly Polymeric Materials. *Chemical Reviews* **2007,** *107* (6), 2270-2299.

20. Wang, J.-S.; Matyjaszewski, K., Controlled/"living" radical polymerization. atom transfer radical polymerization in the presence of transition-metal complexes. *Journal of the American Chemical Society* **1995,** *117* (20), 5614-5615.

21. An, Q.; Huang, T.; Shi, F., Covalent layer-by-layer films: chemistry, design, and multidisciplinary applications. *Chemical Society Reviews* **2018,** *47* (13), 5061-5098.

22. Borges, J.; Mano, J. F., Molecular Interactions Driving the Layer-by-Layer Assembly of Multilayers. *Chemical Reviews* **2014,** *114* (18), 8883-8942.

23. Broderick, A. H.; Lynn, D. M., Covalent Layer-by-Layer Assembly Using Reactive Polymers. In *Functional Polymers by Post-Polymerization Modification*, pp 371-406.

24. Bergbreiter, D. E.; Liao, K.-S., Covalent layer-by-layer assembly—an effective, forgiving way to construct functional robust ultrathin films and nanocomposites. *Soft Matter* **2009,** *5* (1), 23-28.

25. Sezen, H. Photo-dynamic XPS for investigating photoinduced voltage changes in semiconducting materials. Bilkent University, 2011.

26. Habibullah, H., 30 Years of atomic force microscopy: Creep, hysteresis, cross-coupling, and vibration problems of piezoelectric tube scanners. *Measurement* **2020,** *159*, 107776.

27. El Khoury, D. Towards the use of Electrostatic Force Microscopy to study interphases in nanodielectric materials. 2017.

28. Elgrishi, N.; Rountree, K. J.; McCarthy, B. D.; Rountree, E. S.; Eisenhart, T. T.; Dempsey, J. L., A Practical Beginner's Guide to Cyclic Voltammetry. *Journal of Chemical Education* **2018,** *95* (2), 197-206.

29. Chen, J.; Yagi, H.; Furutani, Y.; Nakamura, T.; Inaguma, A.; Guo, H.; Kong, Y.; Goto, Y., Self-assembly of the chaperonin GroEL nanocage induced at submicellar detergent. *Sci Rep* **2014,** *4*, 5614.

30. Martins, M. C.; Ratner, B. D.; Barbosa, M. A., Protein adsorption on mixtures of hydroxyl- and methyl-terminated alkanethiols self-assembled monolayers. *J Biomed Mater Res A* **2003,** *67* (1), 158-71.

31. Pujari, S. P.; Scheres, L.; Marcelis, A. T.; Zuilhof, H., Covalent surface modification of oxide surfaces. *Angewandte Chemie International Edition* **2014,** *53* (25), 6322-6356.

32. Aslam, M.; Bandyopadhyay, K.; Vijayamohanan, K.; Lakshminarayanan, V., Comparative Behavior of Aromatic Disulfide and Diselenide Monolayers on Polycrystalline Gold Films Using Cyclic Voltammetry, STM, and Quartz Crystal Microbalance. *Journal of Colloid and Interface Science* **2001,** *234* (2), 410-417.

33. Schoenenberger, C.; Sondag-Huethorst, J. A. M.; Jorritsma, J.; Fokkink, L. G. J., What Are the "Holes" in Self-Assembled Monolayers of Alkanethiols on Gold? *Langmuir* **1994,** *10* (3), 611-614.

34. Zhao, X.-M.; Wilbur, J. L.; Whitesides, G. M., Using Two-Stage Chemical Amplification To Determine the Density of Defects in Self-Assembled Monolayers of Alkanethiolates on Gold. *Langmuir* **1996,** *12* (22), 5504-5504.

35. Jones, J. A.; Qin, L. A.; Meyerson, H.; Kwon, I. K.; Matsuda, T.; Anderson, J. M., Instability of self-assembled monolayers as a model material system for macrophage/FBGC cellular behavior. *J Biomed Mater Res A* **2008,** *86* (1), 261-268.

36. Chaki, N. K.; Vijayamohanan, K., Self-assembled monolayers as a tunable platform for biosensor applications. *Biosensors and Bioelectronics* **2002,** *17* (1-2), 1-12.

37. Ionescu, M., *Chemistry and technology of polyols for polyurethanes*. iSmithers Rapra Publishing: 2005.

38. Tardio, S.; Abel, M.-L.; Carr, R. H.; Watts, J. F., The interfacial interaction between isocyanate and stainless steel. *International Journal of Adhesion and Adhesives* **2019,** *88*, 1-10.

39. Shimizu, K.; Phanopoulos, C.; Loenders, R.; Abel, M. L.; Watts, J. F., The characterization of the interfacial interaction between polymeric methylene diphenyl diisocyanate and aluminum: a ToF-SIMS and XPS study. *Surface and interface analysis* **2010,** *42* (8), 1432-1444.

40. Nies, C.; Wehlack, C.; Ehbing, H.; Dijkstra, D. J.; Possart, W., Adhesive interactions of polyurethane monomers with native metal surfaces. *The Journal of Adhesion* **2012,** *88* (8), 665-683.

41. Ozenler, S.; Sozen, Y.; Sahin, H.; Yildiz, U. H., Fabrication of post-functionalizable, bio-repellent, electroactive polyurethane interface on gold surface by Surface-Assisted (SurfAst) polymerization. *Langmuir* **2020**.

42. Blöchl, P. E., Projector augmented-wave method. *Physical Review B* **1994,** *50* (24), 17953-17979.

43. Kresse, G.; Furthmüller, J., Efficient iterative schemes for ab initio total-energy calculations using a plane-wave basis set. *Physical Review B* **1996,** *54* (16), 11169-11186.

44. Kresse, G.; Hafner, J., Ab initio molecular dynamics for liquid metals. *Physical Review B* **1993,** *47* (1), 558-561.

45. Perdew, J. P.; Burke, K.; Ernzerhof, M., Generalized Gradient Approximation Made Simple. *Physical Review Letters* **1996,** *77* (18), 3865-3868.

46. Grimme, S., Semiempirical GGA-type density functional constructed with a long-range dispersion correction. *Journal of Computational Chemistry* **2006,** *27* (15), 1787-1799.

47. Beamson, G., High Resolution XPS of Organic Polymers. *The Scienta ESCA 300 Database* **1992**.

48. Bürgi, T., Properties of the gold–sulphur interface: from self-assembled monolayers to clusters. *Nanoscale* **2015,** *7* (38), 15553-15567.

49. Roy, K.; Kar, S.; Das, R. N., Chapter 1 - Background of QSAR and Historical Developments. In *Understanding the Basics of QSAR for Applications in Pharmaceutical Sciences and Risk Assessment*, Roy, K.; Kar, S.; Das, R. N., Eds. Academic Press: Boston, 2015; pp 1-46.

50. Fug, F.; Nies, C.; Possart, W., in situ FTIR study of adhesive interactions of 4, 4′-methylene diphenyl diisocyanate and native metals. *International Journal of Adhesion and Adhesives* **2014,** *52*, 66-76.

51. Gong, S.; Lai, D. T. H.; Su, B.; Si, K. J.; Ma, Z.; Yap, L. W.; Guo, P.; Cheng, W., Highly Stretchy Black Gold E-Skin Nanopatches as Highly Sensitive Wearable Biomedical Sensors. *Advanced Electronic Materials* **2015,** *1* (4).

52. Lee, H.; Hong, Y. J.; Baik, S.; Hyeon, T.; Kim, D.-H., Enzyme-Based Glucose Sensor: From Invasive to Wearable Device. *Advanced Healthcare Materials* **2018,** *7* (8).

53. Choi, S.; Han, S. I.; Jung, D.; Hwang, H. J.; Lim, C.; Bae, S.; Park, O. K.; Tschabrunn, C. M.; Lee, M.; Bae, S. Y.; Yu, J. W.; Ryu, J. H.; Lee, S.-W.; Park, K.; Kang, P. M.; Lee, W. B.; Nezafat, R.; Hyeon, T.; Kim, D.-H., Highly conductive, stretchable and biocompatible Ag–Au core–sheath nanowire composite for wearable and implantable bioelectronics. *Nature Nanotechnology* **2018,** *13* (11), 1048-1056.

54. Lee, S.; Inoue, Y.; Kim, D.; Reuveny, A.; Kuribara, K.; Yokota, T.; Reeder, J.; Sekino, M.; Sekitani, T.; Abe, Y.; Someya, T., A strain-absorbing design for tissue–machine interfaces using a tunable adhesive gel. *Nature Communications* **2014,** *5* (1).

55. Xu, L.; Gutbrod, S. R.; Bonifas, A. P.; Su, Y.; Sulkin, M. S.; Lu, N.; Chung, H.-J.; Jang, K.-I.; Liu, Z.; Ying, M.; Lu, C.; Webb, R. C.; Kim, J.-S.; Laughner, J. I.; Cheng, H.; Liu, Y.; Ameen, A.; Jeong, J.-W.; Kim, G.-T.; Huang, Y.; Efimov, I. R.; Rogers, J. A., 3D multifunctional integumentary membranes for spatiotemporal cardiac measurements and stimulation across the entire epicardium. *Nature Communications* **2014,** *5* (1).

56. Lim, S.; Son, D.; Kim, J.; Lee, Y. B.; Song, J.-K.; Choi, S.; Lee, D. J.; Kim, J. H.; Lee, M.; Hyeon, T.; Kim, D.-H., Transparent and Stretchable Interactive Human Machine Interface Based on Patterned Graphene Heterostructures. *Advanced Functional Materials* **2015,** *25* (3), 375-383.

57. Miyamoto, A.; Lee, S.; Cooray, N. F.; Lee, S.; Mori, M.; Matsuhisa, N.; Jin, H.; Yoda, L.; Yokota, T.; Itoh, A.; Sekino, M.; Kawasaki, H.; Ebihara, T.; Amagai, M.; Someya, T., Inflammation-free, gas-permeable, lightweight, stretchable on-skin electronics with nanomeshes. *Nature Nanotechnology* **2017,** *12* (9), 907-913.

58. Gong, S.; Schwalb, W.; Wang, Y.; Chen, Y.; Tang, Y.; Si, J.; Shirinzadeh, B.; Cheng, W., A wearable and highly sensitive pressure sensor with ultrathin gold nanowires. *Nature Communications* **2014,** *5* (1).

59. Lipomi, D. J.; Vosgueritchian, M.; Tee, B. C. K.; Hellstrom, S. L.; Lee, J. A.; Fox, C. H.; Bao, Z., Skin-like pressure and strain sensors based on transparent elastic films of carbon nanotubes. *Nature Nanotechnology* **2011,** *6* (12), 788-792.

60. Park, J.; Choi, S.; Janardhan, A. H.; Lee, S.-Y.; Raut, S.; Soares, J.; Shin, K.; Yang, S.; Lee, C.; Kang, K.-W.; Cho, H. R.; Kim, S. J.; Seo, P.; Hyun, W.; Jung, S.; Lee, H.-J.; Lee, N.; Choi, S. H.; Sacks, M.; Lu, N.; Josephson, M. E.; Hyeon, T.; Kim, D.-H.; Hwang, H. J., Electromechanical cardioplasty using a wrapped elasto-conductive epicardial mesh. *Science Translational Medicine* **2016,** *8* (344), 344ra86-344ra86.

61. Son, D.; Lee, J.; Qiao, S.; Ghaffari, R.; Kim, J.; Lee, J. E.; Song, C.; Kim, S. J.; Lee, D. J.; Jun, S. W.; Yang, S.; Park, M.; Shin, J.; Do, K.; Lee, M.; Kang, K.; Hwang, C. S.; Lu, N.; Hyeon, T.; Kim, D.-H., Multifunctional wearable devices for diagnosis and therapy of movement disorders. *Nature Nanotechnology* **2014,** *9* (5), 397-404.

62. Wang, J.; Zhao, X.; Li, J.; Kuang, X.; Fan, Y.; Wei, G.; Su, Z., Electrostatic Assembly of Peptide Nanofiber–Biomimetic Silver Nanowires onto Graphene for Electrochemical Sensors. *ACS Macro Letters* **2014,** *3* (6), 529-533.

63. Weng, Y.-H.; Xu, L.-T.; Chen, M.; Zhai, Y.-Y.; Zhao, Y.; Ghorai, S. K.; Pan, X.-H.; Cao, S.-H.; Li, Y.-Q., In Situ Monitoring of Fluorescent Polymer Brushes by Angle-Scanning Based Surface Plasmon Coupled Emission. *ACS Macro Letters* **2019,** *8* (2), 223-227.

64. Ma, H.; Hyun, J.; Stiller, P.; Chilkoti, A., "Non-Fouling" Oligo(ethylene glycol)- Functionalized Polymer Brushes Synthesized by Surface-Initiated Atom Transfer Radical Polymerization. *Advanced Materials* **2004,** *16* (4), 338-341.

65. Conzatti, G.; Cavalie, S.; Combes, C.; Torrisani, J.; Carrere, N.; Tourrette, A., PNIPAM grafted surfaces through ATRP and RAFT polymerization: Chemistry and bioadhesion. *Colloids and Surfaces B: Biointerfaces* **2017,** *151*, 143-155.

66. Murugan, P.; Krishnamurthy, M.; Jaisankar, S. N.; Samanta, D.; Mandal, A. B., Controlled decoration of the surface with macromolecules: polymerization on a self-assembled monolayer (SAM). *Chemical Society Reviews* **2015,** *44* (10), 3212-3243.

67. Ngo, B. K. D.; Grunlan, M. A., Protein Resistant Polymeric Biomaterials. *ACS Macro Letters* **2017,** *6* (9), 992-1000.

68. Rodriguez, K. J.; Gajewska, B.; Pollard, J.; Pellizzoni, M. M.; Fodor, C.; Bruns, N., Repurposing Biocatalysts to Control Radical Polymerizations. *ACS Macro Letters* **2018,** *7* (9), 1111-1119.

69. Jeong, W.; Kang, H.; Kim, E.; Jeong, J.; Hong, D., Surface-Initiated ARGET ATRP of Antifouling Zwitterionic Brushes Using Versatile and Uniform Initiator Film. *Langmuir* **2019,** *35* (41), 13268-13274.

70. Pinto, J. C.; Whiting, G. L.; Khodabakhsh, S.; Torre, L.; Rodríguez, A.; Dalgliesh, R. M.; Higgins, A. M.; Andreasen, J. W.; Nielsen, M. M.; Geoghegan, M.; Huck, W. T. S.; Sirringhaus, H., Organic Thin Film Transistors with Polymer Brush Gate Dielectrics Synthesized by Atom Transfer Radical Polymerization. *Advanced Functional Materials* **2008,** *18* (1), 36-43.

71. Ge, F.; Wang, X.; Zhang, Y.; Song, E.; Zhang, G.; Lu, H.; Cho, K.; Qiu, L., Modulating the Surface via Polymer Brush for High-Performance Inkjet-Printed Organic Thin-Film Transistors. *Advanced Electronic Materials* **2017,** *3* (1).

72. Joh, D. Y.; McGuire, F.; Abedini-Nassab, R.; Andrews, J. B.; Achar, R. K.; Zimmers, Z.; Mozhdehi, D.; Blair, R.; Albarghouthi, F.; Oles, W.; Richter, J.; Fontes, C. M.; Hucknall, A. M.; Yellen, B. B.; Franklin, A. D.; Chilkoti, A., Poly(oligo(ethylene glycol) methyl ether methacrylate) Brushes on High-κ Metal Oxide Dielectric Surfaces for Bioelectrical Environments. *ACS Applied Materials & Interfaces* **2017,** *9* (6), 5522-5529.

73. Tang, P.; di Cio, S.; Wang, W.; E. Gautrot, J., Surface-Initiated Poly(oligo(2-alkyl-2-oxazoline)methacrylate) Brushes. *Langmuir* **2018,** *34* (34), 10019-10027.

74. Yeow, J.; Chapman, R.; Gormley, A. J.; Boyer, C., Up in the air: oxygen tolerance in controlled/living radical polymerisation. *Chemical Society Reviews* **2018,** *47* (12), 4357-4387.

75. Hong, D.; Hung, H.-C.; Wu, K.; Lin, X.; Sun, F.; Zhang, P.; Liu, S.; Cook, K. E.; Jiang, S., Achieving Ultralow Fouling under Ambient Conditions via Surface-Initiated ARGET ATRP of Carboxybetaine. *ACS Applied Materials & Interfaces* **2017,** *9* (11), 9255-9259.

76. Socrates, G., *Infrared and Raman Characteristic Group Frequencies: Tables and Charts, 3rd Edition*. Wiley: 2004; p 366.

77. Sardon, H.; Irusta, L.; Fernández-Berridi, M. J., Synthesis of isophorone diisocyanate (IPDI) based waterborne polyurethanes: Comparison between zirconium and tin catalysts in the polymerization process. *Progress in Organic Coatings* **2009,** *66* (3), 291-295.

78. Grasselli, D. L.-V. N. C. W. F. J., *The Handbook of Infrared and Raman Characteristic Frequencies of Organic Molecules*. Academic Press: 1991.

79. Kojio, K.; Uchiba, Y.; Mitsui, Y.; Furukawa, M.; Sasaki, S.; Matsunaga, H.; Okuda, H., Depression of microphase-separated domain size of polyurethanes in confined geometry. *Macromolecules* **2007,** *40* (8), 2625-2628.

80. Zharkov, V. V.; Strikovsky, A. G.; Verteletskaya, T. E., Amide I absorption band: description of the urethane group association scheme in polyether urethane elastomers. *Polymer* **1993,** *34* (5), 938-941.

81. Strikovsky, A. G.; Zharkov, V. V.; Letunovsky, M. P., Ir- spectroscopy of hydrogen bond as a method of analytical determination of physical network in poly(ether urethane)s. *Macromolecular Symposia* **1995,** *94* (1), 181-188.

82. Check, C.; Imre, B.; Gojzewski, H.; Chartoff, R.; Vancso, G. J., Kinetic aspects of formation and processing of polycaprolactone polyurethanes in situ from a blocked isocyanate. *Polymer Chemistry* **2018,** *9* (15), 1983-1995.

83. Mishra, A.; Aswal, V. K.; Maiti, P., Nanostructure to Microstructure Self-Assembly of Aliphatic Polyurethanes: The Effect on Mechanical Properties. *The Journal of Physical Chemistry B* **2010,** *114* (16), 5292-5300.

84. Klinedinst, D. B.; Yilgör, E.; Yilgör, I.; Beyer, F. L.; Wilkes, G. L., Structure–property behavior of segmented polyurethaneurea copolymers based on an ethylene–butylene soft segment. *Polymer* **2005,** *46* (23), 10191-10201.

85. Yilgör, I.; Yilgör, E.; Wilkes, G. L., Critical parameters in designing segmented polyurethanes and their effect on morphology and properties: A comprehensive review. *Polymer* **2015,** *58*, A1-A36.

86. Queiroz, D.; Botelhodorego, A.; Depinho, M., Bi-soft segment polyurethane membranes: Surface studies by X-ray photoelectron spectroscopy. *Journal of Membrane Science* **2006,** *281* (1-2), 239-244.

87. Shimizu, K.; Phanopoulos, C.; Loenders, R.; Abel, M.-L.; Watts, J. F., The characterization of the interfacial interaction between polymeric methylene diphenyl diisocyanate and aluminum: a ToF-SIMS and XPS study. *Surface and Interface Analysis* **2010,** *42* (8), 1432-1444.

88. Vargo, T. G.; Hook, D. J.; Gardella, J. A.; Eberhardt, M. A.; Meyer, A. E.; Baier, R. E., A Surface Spectroscopic and Wettability Study of a Segmented Block Copolymer Poly(etherurethane). *Appl. Spectrosc.* **1991,** *45* (3), 448-456.

89. Higaki, Y.; Kobayashi, M.; Murakami, D.; Takahara, A., Anti-fouling behavior of polymer brush immobilized surfaces. *Polymer Journal* **2016,** *48* (4), 325-331.

90. Krishnan, S.; Weinman, C. J.; Ober, C. K., Advances in polymers for anti-biofouling surfaces. *Journal of Materials Chemistry* **2008,** *18* (29), 3405-3413.

91. Heuberger, M.; Drobek, T.; Vörös, J., About the Role of Water in Surface-Grafted Poly(ethylene glycol) Layers. *Langmuir* **2004,** *20* (22), 9445-9448.

92. Wang, F.; Zhang, H.; Yu, B.; Wang, S.; Shen, Y.; Cong, H., Review of the research on anti-protein fouling coatings materials. *Progress in Organic Coatings* **2020,** *147*, 105860.

93. Benhabbour, S. R.; Liu, L.; Sheardown, H.; Adronov, A., Protein Resistance of Surfaces Prepared by Chemisorption of Monothiolated Poly(ethylene glycol) to Gold and Dendronization with Aliphatic Polyester Dendrons: Effect of Hydrophilic Dendrons. *Macromolecules* **2008,** *41* (7), 2567-2576.

94. Sharma, S.; Johnson, R. W.; Desai, T. A., Evaluation of the Stability of Nonfouling Ultrathin Poly(ethylene glycol) Films for Silicon-Based Microdevices. *Langmuir* **2004,** *20* (2), 348-356.

95. Danielsen, S. P. O.; Davidson, E. C.; Fredrickson, G. H.; Segalman, R. A., Absence of Electrostatic Rigidity in Conjugated Polyelectrolytes with Pendant Charges. *ACS Macro Letters* **2019,** *8* (9), 1147-1152.

96. Holliday, S.; Donaghey, J. E.; McCulloch, I., Advances in Charge Carrier Mobilities of Semiconducting Polymers Used in Organic Transistors. *Chemistry of Materials* **2014,** *26* (1), 647-663.

97. Baycan Koyuncu, F.; Davis, A. R.; Carter, K. R., Emissive Conjugated Polymer Networks with Tunable Band-Gaps via Thiol–Ene Click Chemistry. *Chemistry of Materials* **2012,** *24* (22), 4410-4416.

98. Davis, A. R.; Carter, K. R., Surface Grafting of Vinyl-Functionalized Poly(fluorene)s via Thiol–Ene Click Chemistry. *Langmuir* **2014,** *30* (15), 4427-4433.

99. Martin, K. L.; Nyquist, Y.; Burnett, E. K.; Briseno, A. L.; Carter, K. R., Surface Grafting of Functionalized Poly(thiophene)s Using Thiol–Ene Click Chemistry for Thin Film Stabilization. *ACS Applied Materials & Interfaces* **2016,** *8* (44), 30543-30551.

100. Yong, Q.; Liang, C., Synthesis of an Aqueous Self-Matting Acrylic Resin with Low Gloss and High Transparency via Controlling Surface Morphology. *Polymers* **2019,** *11* (2).

101. Yucel, M.; Koc, A.; Ulgenalp, A.; Akkoc, G. D.; Ceyhan, M.; Yildiz, U. H., PCR-Free Methodology for Detection of Single-Nucleotide Polymorphism with a Cationic Polythiophene Reporter. *ACS Sensors* **2021,** *6* (3), 950-957.

102. Blagbrough, I. S.; Mackenzie, N. E.; Ortiz, C.; Scott, A. I., The condensation reaction between isocyanates and carboxylic acids. A practical synthesis of substituted amides and anilides. *Tetrahedron Letters* **1986,** *27* (11), 1251-1254.

103. Diao, P.; Jiang, D.; Cui, X.; Gu, D.; Tong, R.; Zhong, B., Studies of structural disorder of self-assembled thiol monolayers on gold by cyclic voltammetry and ac impedance. *Journal of Electroanalytical Chemistry* **1999,** *464* (1), 61-67.

104. Sabatani, E.; Rubinstein, I., Organized self-assembling monolayers on electrodes. 2. Monolayer-based ultramicroelectrodes for the study of very rapid electrode kinetics. *The Journal of Physical Chemistry* **1987,** *91* (27), 6663-6669.

105. Zhou, X.; Dai, J.; Wu, K., Steering on-surface reactions with self-assembly strategy. *Physical Chemistry Chemical Physics* **2017,** *19* (47), 31531-31539.

106. Özenler, S.; Yucel, M.; Tüncel, Ö.; Kaya, H.; Özçelik, S.; Yildiz, U. H., Single Chain Cationic Polymer Dot as a Fluorescent Probe for Cell Imaging and Selective Determination of Hepatocellular Carcinoma Cells. *Analytical Chemistry* **2019,** *91* (16), 10357-10360.

107. Chen, Y.; Cui, H.; Li, L.; Tian, Z.; Tang, Z., Controlling micro-phase separation in semi-crystalline/amorphous conjugated block copolymers. *Polymer Chemistry* **2014,** *5* (15), 4441-4445.

108. Richardson, J. J.; Cui, J.; Björnmalm, M.; Braunger, J. A.; Ejima, H.; Caruso, F., Innovation in Layer-by-Layer Assembly. *Chemical Reviews* **2016,** *116* (23), 14828-14867.

109. Liu, Y.; Bruening, M. L.; Bergbreiter, D. E.; Crooks, R. M., Multilayer Dendrimer–Polyanhydride Composite Films on Glass, Silicon, and Gold Wafers. *Angewandte Chemie International Edition in English* **1997,** *36* (19), 2114-2116.

110. Liu, Y.; Zhao, M.; Bergbreiter, D. E.; Crooks, R. M., pH-Switchable, Ultrathin Permselective Membranes Prepared from Multilayer Polymer Composites. *Journal of the American Chemical Society* **1997,** *119* (37), 8720-8721.

111. Zhao, M.; Liu, Y.; Crooks, R. M.; Bergbreiter, D. E., Preparation of Highly Impermeable Hyperbranched Polymer Thin-Film Coatings Using Dendrimers First as Building Blocks and Then as in Situ Thermosetting Agents. *Journal of the American Chemical Society* **1999,** *121* (5), 923-930.

112. Buck, M. E.; Zhang, J.; Lynn, D. M., Layer-by-Layer Assembly of Reactive Ultrathin Films Mediated by Click-Type Reactions of Poly(2-Alkenyl Azlactone)s. *Advanced Materials* **2007,** *19* (22), 3951-3955.

113. Such, G. K.; Quinn, J. F.; Quinn, A.; Tjipto, E.; Caruso, F., Assembly of Ultrathin Polymer Multilayer Films by Click Chemistry. *Journal of the American Chemical Society* **2006,** *128* (29), 9318-9319.

114. Vestberg, R.; Malkoch, M.; Kade, M.; Wu, P.; Fokin, V. V.; Barry Sharpless, K.; Drockenmuller, E.; Hawker, C. J., Role of architecture and molecular weight in the formation of tailor-made ultrathin multilayers using dendritic macromolecules and click chemistry. *Journal of Polymer Science Part A: Polymer Chemistry* **2007,** *45* (14), 2835-2846.

115. Mamedov, A. A.; Kotov, N. A.; Prato, M.; Guldi, D. M.; Wicksted, J. P.; Hirsch, A., Molecular design of strong single-wall carbon nanotube/polyelectrolyte multilayer composites. *Nature Materials* **2002,** *1* (3), 190-194.

116. Qureshi, S. S.; Zheng, Z.; Sarwar, M. I.; Félix, O.; Decher, G., Nanoprotective Layer-by-Layer Coatings with Epoxy Components for Enhancing Abrasion Resistance: Toward Robust Multimaterial Nanoscale Films. *ACS Nano* **2013,** *7* (10), 9336-9344.

117. Makamba, H.; Hsieh, Y.-Y.; Sung, W.-C.; Chen, S.-H., Stable Permanently Hydrophilic Protein-Resistant Thin-Film Coatings on Poly(dimethylsiloxane) Substrates by Electrostatic Self-Assembly and Chemical Cross-Linking. *Analytical Chemistry* **2005,** *77* (13), 3971-3978.

118. Aumsuwan, N.; Ye, S.-H.; Wagner, W. R.; Urban, M. W., Covalent Attachment of Multilayers on Poly(tetrafluoroethylene) Surfaces. *Langmuir* **2011,** *27* (17), 11106-11110.

119. Hu, X.; Gong, X., A new route to fabricate biocompatible hydrogels with controlled drug delivery behavior. *Journal of Colloid and Interface Science* **2016,** *470*, 62-70.

120. Ma, L.; Cheng, C.; He, C.; Nie, C.; Deng, J.; Sun, S.; Zhao, C., Substrate-Independent Robust and Heparin-Mimetic Hydrogel Thin Film Coating via Combined LbL Self-Assembly and Mussel-Inspired Post-Cross-linking. *ACS Applied Materials & Interfaces* **2015,** *7* (47), 26050-26062.

121. Guin, T.; Stevens, B.; Krecker, M.; D'Angelo, J.; Humood, M.; Song, Y.; Smith, R.; Polycarpou, A.; Grunlan, J. C., Ultrastrong, Chemically Resistant Reduced Graphene Oxide-based Multilayer Thin Films with Damage Detection Capability. *ACS Applied Materials & Interfaces* **2016,** *8* (9), 6229-6235.

122. Liu, X.; Wen, N.; Wang, X.; Zheng, Y., Layer-by-Layer Self-Assembled Graphene Multilayer Films via Covalent Bonds for Supercapacitor Electrodes. *Nanomaterials and Nanotechnology* **2015,** *5*, 14.

123. Olichwer, N.; Leib, E. W.; Halfar, A. H.; Petrov, A.; Vossmeyer, T., Cross-Linked Gold Nanoparticles on Polyethylene: Resistive Responses to Tensile Strain and Vapors. *ACS Applied Materials & Interfaces* **2012,** *4* (11), 6151-6161.

124. Ou, X.; Jiang, L.; Chen, P.; Zhu, M.; Hu, W.; Liu, M.; Zhu, J.; Ju, H., Highly Stable Graphene-Based Multilayer Films Immobilized via Covalent Bonds and Their Applications in Organic Field-Effect Transistors. *Advanced Functional Materials* **2013,** *23* (19), 2422-2435.

125. Sun, Y.; Yan, F.; Yang, W.; Sun, C., Multilayered construction of glucose oxidase and silica nanoparticles on Au electrodes based on layer-by-layer covalent attachment. *Biomaterials* **2006,** *27* (21), 4042-4049.

126. Xiong, Z.; Gu, T.; Wang, X., Self-Assembled Multilayer Films of Sulfonated Graphene and Polystyrene-Based Diazonium Salt as Photo-Cross-Linkable Supercapacitor Electrodes. *Langmuir* **2014,** *30* (2), 522-532.

127. Zhang, S.; Yang, W.; Niu, Y.; Sun, C., Multilayered construction of glucose oxidase and poly(allylamine)ferrocene on gold electrodes by means of layer-by-layer covalent attachment. *Sensors and Actuators B: Chemical* **2004,** *101* (3), 387-393.

128. Zhang, S.; Yang, W.; Niu, Y.; Sun, C., Multilayered construction of glucose oxidase on gold electrodes based on layer-by-layer covalent attachment. *Analytica Chimica Acta* **2004,** *523* (2), 209-217.

129. Jung, I. Y.; Kim, J. S.; Choi, B. R.; Lee, K.; Lee, H., Hydrogel based biosensors for in vitro diagnostics of biochemicals, proteins, and genes. *Advanced healthcare materials* **2017,** *6* (12), 1601475.

130. Karbarz, M.; Mackiewicz, M.; Kaniewska, K.; Marcisz, K.; Stojek, Z., Recent developments in design and functionalization of micro-and nanostructural environmentally-sensitive hydrogels based on N-isopropylacrylamide. *Applied Materials Today* **2017,** *9*, 516-532.

131. Li, L.; Shi, Y.; Pan, L.; Shi, Y.; Yu, G., Rational design and applications of conducting polymer hydrogels as electrochemical biosensors. *Journal of Materials Chemistry B* **2015,** *3* (15), 2920-2930.

132. Qu, F.; Zhang, Y.; Rasooly, A.; Yang, M., Electrochemical biosensing platform using hydrogel prepared from ferrocene modified amino acid as highly efficient immobilization matrix. *Analytical chemistry* **2014,** *86* (2), 973-976.

133. Freeman, M. H.; Hall, J. R.; Leopold, M. C., Monolayer-protected nanoparticle doped xerogels as functional components of amperometric glucose biosensors. *Analytical chemistry* **2013,** *85* (8), 4057-4065.

134. Zhai, D.; Liu, B.; Shi, Y.; Pan, L.; Wang, Y.; Li, W.; Zhang, R.; Yu, G., Highly sensitive glucose sensor based on Pt nanoparticle/polyaniline hydrogel heterostructures. *ACS nano* **2013,** *7* (4), 3540-3546.

135. Gnanasampanthan, T.; Beyer, C. D.; Yu, W.; Karthäuser, J. F.; Wanka, R.; Spöllmann, S.; Becker, H.-W.; Aldred, N.; Clare, A. S.; Rosenhahn, A., Effect of Multilayer Termination on Nonspecific Protein Adsorption and Antifouling Activity of Alginate-Based Layer-by-Layer Coatings. *Langmuir* **2021,** *37* (19), 5950-5963.

136. Kuo, C.-W.; Lai, J.-J.; Wei, K. H.; Chen, P., Surface modified gold nanowires for mammalian cell transfection. *Nanotechnology* **2007,** *19* (2), 025103.

137. Milton, R. D.; Wang, T.; Knoche, K. L.; Minteer, S. D., Tailoring Biointerfaces for Electrocatalysis. *Langmuir* **2016,** *32* (10), 2291-2301.

138. Oh, S. J.; Cho, S. J.; Kim, C. O.; Park, J. W., Characteristics of DNA Microarrays Fabricated on Various Aminosilane Layers. *Langmuir* **2002,** *18* (5), 1764-1769.

139. Cetin, M.; Esen, C.; Daglar, O.; Luleburgaz, S.; Hizal, G.; Durmaz, H.; Tunca, U., 1, 3-Dipolar and Diels–Alder cycloaddition reactions on polyester backbones possessing internal electron-deficient alkyne moieties. *Polymer Chemistry* **2016,** *7* (46), 7094-7100.

140. Merchant, S. A.; Glatzhofer, D. T.; Schmidtke, D. W., Effects of Electrolyte and pH on the Behavior of Cross-Linked Films of Ferrocene-Modified Poly(ethylenimine). *Langmuir* **2007,** *23* (22), 11295-11302.

141. Yildirimkaraman, O.; Özenler, S.; Gunay, U. S.; Durmaz, H.; Yıldız, Ü. H., Electroactive Nanogel Formation by Reactive Layer-by-Layer Assembly of Polyester and Branched Polyethylenimine via Aza-Michael Addition. *Langmuir* **2021,** *37* (37), 10902-10913.

142. Gunay, U. S.; Cetin, M.; Daglar, O.; Hizal, G.; Tunca, U.; Durmaz, H., Ultrafast and efficient aza-and thiol-Michael reactions on a polyester scaffold with internal electron deficient triple bonds. *Polymer Chemistry* **2018,** *9* (22), 3037-3054.

143. Genest, A.; Portinha, D.; Fleury, E.; Ganachaud, F., The aza-Michael reaction as an alternative strategy to generate advanced silicon-based (macro)molecules and materials. *Progress in Polymer Science* **2017,** *72*, 61-110.

144. González-Torres, M.; Olayo, M. G.; Cruz, G. J.; Gómez, L. M.; Sánchez-Mendieta, V.; González-Salgado, F., XPS Study of the Chemical Structure of Plasma Biocopolymers of Pyrrole and Ethylene Glycol. *Advances in Chemistry* **2014,** *2014*, 965920.

145. Gomez, L. M.; Cruz, G. J.; Olayo, M. G.; Gonzalez-Torres, M.; Gonzalez-Salgado, F.; Lopez-Gracia, O. G., Analysis of crosslinking in polypyrrole particles synthesized by plasma. *Polymer Bulletin* **2014,** *71* (12), 3275-3287.

146. González-Torres, M.; Olayo, M. G.; Gómez, L. M.; Morales, J.; Olayo, R.; Ramírez, R.; Flores, F. G.; Mejía-Cuero, M. R.; Cruz, G. J., Chemical interactions of heparin in porous polypyrrole, an example of drug–carrier destructive interaction. *Polymer Bulletin* **2020,** *77* (1), 375-385.

147. Rybachuk, M.; Bell, J., Electronic states of trans-polyacetylene, poly(p-phenylene vinylene) and sp-hybridised carbon species in amorphous hydrogenated carbon probed by resonant Raman scattering. *Carbon* **2009,** *47*, 2481-2490.

148. Gilbert, J. B.; Rubner, M. F.; Cohen, R. E., Depth-profiling X-ray photoelectron spectroscopy (XPS) analysis of interlayer diffusion in polyelectrolyte multilayers. *Proceedings of the National Academy of Sciences* **2013,** *110* (17), 6651-6656.

149. Lee, H.; Gilbert, J. B.; Angilè, F. E.; Yang, R.; Lee, D.; Rubner, M. F.; Cohen, R. E., Design and Fabrication of Zwitter-Wettable Nanostructured Films. *ACS Applied Materials & Interfaces* **2015,** *7* (1), 1004-1011.

150. Sydow, S.; de Cassan, D.; Hänsch, R.; Gengenbach, T. R.; Easton, C. D.; Thissen, H.; Menzel, H., Layer-by-layer deposition of chitosan nanoparticles as drug-release coatings for PCL nanofibers. *Biomaterials Science* **2019,** *7* (1), 233-246.

151. Taketa, T. B.; dos Santos, D. M.; Fiamingo, A.; Vaz, J. M.; Beppu, M. M.; Campana-Filho, S. P.; Cohen, R. E.; Rubner, M. F., Investigation of the Internal Chemical Composition of Chitosan-Based LbL Films by Depth-Profiling X-ray Photoelectron Spectroscopy (XPS) Analysis. *Langmuir* **2018,** *34* (4), 1429-1440.

152. Guan, X.; Avci-Adali, M.; Alarçin, E.; Cheng, H.; Kashaf, S. S.; Li, Y.; Chawla, A.; Jang, H. L.; Khademhosseini, A., Development of hydrogels for regenerative engineering. *Biotechnology journal* **2017,** *12* (5).

153. Barbucci, R.; Lamponi, S.; Pasqui, D.; Rossi, A.; Weber, E., Micropatterned polysaccharide surfaces via laser ablation for cell guidance. *Materials Science and Engineering: C* **2003,** *23* (3), 329-335.

154. Fink, J.; Théry, M.; Azioune, A.; Dupont, R.; Chatelain, F.; Bornens, M.; Piel, M., Comparative study and improvement of current cell micro-patterning techniques. *Lab on a chip* **2007,** *7* (6), 672-80.

155. Oliver, J.-a. N.; Su, Y.; Lu, X.; Kuo, P.-H.; Du, J.; Zhu, D., Bioactive glass coatings on metallic implants for biomedical applications. *Bioactive Materials* **2019,** *4*, 261-270.

156. Koksal, B.; Onbas, R.; Baskurt, M.; Sahın, H.; Arslan Yildiz, A.; Yildiz, U. H., Boosting up printability of biomacromolecule based bio-ink by modulation of hydrogen bonding pairs. *European Polymer Journal* **2020,** *141*, 110070.

157. Neupane, G. P.; Dhakal, K. P.; Kim, M. S.; Lee, H.; Guthold, M.; Joseph, V. S.; Hong, J. D.; Kim, J., Simple method of DNA stretching on glass substrate for fluorescence imaging and spectroscopy. *J Biomed Opt* **2014,** *19* (5), 051210.

158. Hu, Y.; You, J.-O.; Aizenberg, J., Micropatterned Hydrogel Surface with High-Aspect-Ratio Features for Cell Guidance and Tissue Growth. *ACS Applied Materials & Interfaces* **2016,** *8* (34), 21939-21945.

159. Jahnavi, S.; Arthi, N.; Pallavi, S.; Selvaraju, C.; Bhuvaneshwar, G. S.; Kumary, T. V.; Verma, R. S., Nanosecond laser ablation enhances cellular infiltration in a hybrid tissue scaffold. *Materials science & engineering. C, Materials for biological applications* **2017,** *77*, 190-201.

VITA

PERSONAL INFORMATION

Surname, Name: Özenler, Sezer

EDUCATION

Degree, Institution, Year of Graduation

MSc, Anadolu University – Analytical Chemistry, 2015

BSc, Muğla Sıtkı Koçman University - Chemistry, 2010

WORK EXPERIENCE

Year, Place, Enrollment

1. 2018-2019, Izmir Institute of Technology, Research Scholar in TUBITAK 1001 Project encoded 116Z547

2. 2019-2020, Izmir Institute of Technology, Scientific Research Projects, 2019-IYTE-291

3. 2020-2021 Friedrich-Alexander-Universität Erlangen-Nürnberg, 2214-A - International Research Fellowship Programme for PhD Students Research Project supported by TUBITAK, Visiting Researcher

PUBLICATIONS

1. Yildirimkaraman, O.; Özenler, S.; Gunay, U. S.; Durmaz, H.; Yıldız, Ü. H., Electroactive Nanogel Formation by Reactive Layer-by-Layer Assembly of Polyester and Branched Polyethylenimine via Aza-Michael Addition. Langmuir 2021.

2. Özenler, S., Sozen, Y., Sahin, H., & Yildiz, U. H. (2020). Fabrication of a Postfunctionalizable, Biorepellent, Electroactive Polyurethane Interface on a Gold Surface by Surface-Assisted Polymerization. Langmuir, 36(24), 6828-6836.

3. Aydın, H. B., Cheema, J. A., Ammanath, G., Toklucu, C., Yucel, M., Özenler, S., . . . Yildiz, U. H. (2020). Pixelated colorimetric nucleic acid assay. Talanta, 209, 120581.

4. Özenler, S., Yucel, M., Tüncel, O., Kaya, H., Özçelik, S., & Yildiz, U. H. (2019). Single Chain Cationic Polymer Dot as a Fluorescent Probe for Cell Imaging and Selective Determination of Hepatocellular Carcinoma Cells. Analytical chemistry, 91(16), 10357-10360.

5. Özenler, S., Kaya, H., Elmaci, N., & Yildiz, U. H. (2019). Transition-Metal-Free Direct C-H Arylation of Thiophene in Aqueous Media via Potassium Peroxymonosulfate. ChemistrySelect, 4(29), 8516-8521.

6. B. Yildiz, S. Ozenler, M. Yucel, U.H. Yildiz, A. Arslan Yildiz Nanopharmaceuticals: Principles and Applications Vol. 1. Environmental Chemistry for a Sustainable World, Yata V., Ranjan S., Dasgupta N., Biomimetic and Synthetic Gels for Nanopharmaceutical Applications, ISBN: 978-3-030-44924-7 Springer, Cham, 2021.

7. S. Özenler, M. Yücel & Ü. H. Yıldız, Conformational Switching in Nanofibers: A New Bioelectronic Interface for Gas Sensors, Parlak O., Switchable Bioelectronics, ISBN: 978-1-003-05600-3: Jenny Stanford Publishing, 2020.

READY TO BE SUBMITTED MANUSCRİPTS

1. Fabrication of Cationic Polythiophene Nanowires on a Gold Surface by Surface-Assisted Polymerization.

2. Nanogel Formation by Nanogradient Reactive Layer-by-Layer Assembly via Aza-Michael Addition on Gold Surface.

3. Micro-Patterning of Hydrogel by Laser Ablation on Glass Surface for Cell Guidance.

PROOFREADINGSERVICES.COM

October 13, 2021

ProofreadingServices.com, a professional proofreading and editing service, certifies that we reviewed "Preparation of Nanostructured Interface by Polymer Grafting on Various Solid Substrates for Biosensor Application" for Sezer ÖZENLER on October 8, 2021.

Thank you.

Luke Palder
CEO | ProofreadingServices.com
1-800-49-CORRECT (1-800-492-6773) | http://www.ProofreadingServices.com